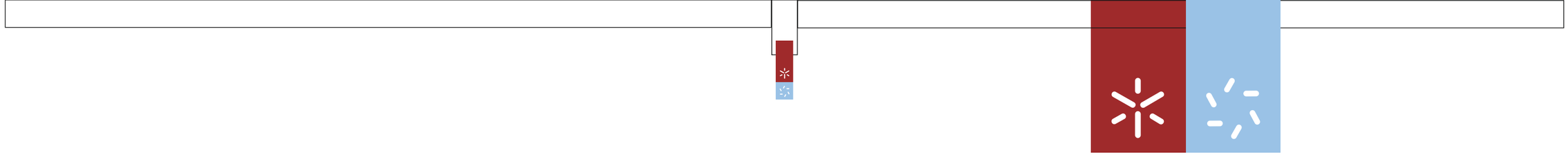

Universidade do Minho
Escola de Ciências

Fábio André Rodrigues Ferreira

Study of the electronic structure of bidimensional materials with the *GW* approximation and Bethe-Salpeter equation

outubro de 2016

Fábio André Rodrigues Ferreira **Study of the electronic structure of bidimensional materials with the *GW* approximation and Bethe-Salpeter equation**

UMinho | 2016

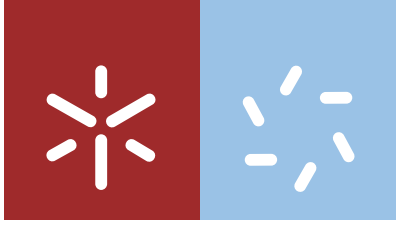

Universidade do Minho
Escola de Ciências

Fábio André Rodrigues Ferreira

Study of the electronic structure of bidimensional materials with the *GW* approximation and Bethe-Salpeter equation

Dissertação de Mestrado
Mestrado em Fsica
Ramo de Física Aplicada

Trabalho realizado sob orientação do
Professor Doutor Ricardo Mendes Ribeiro

outubro de 2016

Acknowledgments

First I want to thank my advisor, Professor Ricardo Ribeiro, for helping me in every step of this work. Without his patience and willingness, this thesis would not have the same quality.

I also want to thank "Search-ON2: Revitalization of HPC infrastructure of UMinho" (NORTE-07-0162-FEDER-000086), co-funded by the North Portugal Regional Operational Programme (ON.2 – O Novo Norte), under the National Strategic Reference Framework (NSRF), through the European Regional Development Fund (ERDF).

This work was supported by National Funds through the Portuguese Foundation for Science and Technology (FCT) in the framework of the Strategic Funding UID/FIS/04650/2013" and through project PTDC/FIS-NAN/3668/2014.

Finally I would like to thank my family and my close friends for keeping me motivated for the realization of this thesis.

Abstract

Study of the electronic structure of bidimensional materials with the GW approximation and Bethe-Salpeter equation

In this work the electronic and optical properties of bidimensional materials h-BN and phosphoerene have been studied. It is well known that DFT often fails to predict properties like electronic band-structures and absorption spectra. To correct those predictions, theories that use electron-electron and electron-hole interactions are needed. The GW approximation formalism, which includes electron-electron interactions, is used to compute the electronic band-structures of the h-BN and phosphorene. With the electronic band-structures computed we can measure quantities like the band gap value. The BSE formalism, which includes electron-hole interactions, is used to compute the absorption spectra. This allows us to measure the optical gap and the excitonic binding energy. Only a few theoretical works that use many-body theories like GW approximation and BSE have been done in these materials. Their results are not consistent enough to give a clear understanding of the electronic and optical properties of these two materials. This work aims at clarifying the issue.

Resumo

Estudo de estrutura electrónica de materias bidimensionais na aproximação GW e pela equação Bethe-Salpeter

Neste trabalho as propriedades electrónicas e ópticas dos materiais bidimensionais h-BN e fosforeno foram estudadas. É sabido que a DFT falha na maior parte das vezes a previsão de propriedades como a estrutura de bandas electrónicas e o espectro de absorção. Para corrigir tais previsões, teorias que incluem interacções electrão-electrão e electrão-lacuna são necessárias. O formalismo da aproximação GW, que inclui interacções electrão-electrão, é usado para calcular as estruturas de bandas electrónicas. Desta forma podemos medir o hiato de banda destes materiais. O formalismo BSE, que inclui interacções electrão-lacuna, é usado para calcular o espectro de absorção. Com este espectro podemos medir o valor do hiato óptico e também a energia de ligação do excitão. Poucos trabalhos que utilizam teorias com efeitos de muitos corpos como a aproximação GW e a BSE foram feitos para estes dois materiais. Dessa forma há uma falta de dados para termos um conhecimento claro das suas propriedades electrónicas e ópticas. Este trabalho tem como objectivo fornecer tal conhecimneto.

Contents

List of Figures

List of Tables

Chapter 1

Introduction

Density functional theory (DFT) is a very successful computational method to determine ground state properties of many-electron systems. One of its most important applications is to predict the electronic band-structure of solids, which allows us to study the electronic and optical properties of a particular material. DFT is very precise when predicting ground state properties like lattice parameters, bulk modulus and cohesive energies, However, it does not predict correctly the electronic and optical properties of semiconductors and insulators in most cases. Electronic bands-structures computed by DFT give band gaps often underestimated, predicting metal materials that are semiconductors or insulators [1–3]. Other electronic properties like ionization energies and magnetic moments are also in disagreement with experimental results [4, 5]. And because optical properties are very related to electronic properties, DFT also gives wrong predictions in quantities like the dielectric functions and absorption spectra [6]. The reason for these discrepancies is that many of the properties are related to excited states, which are outside the DFT domain.

The basic idea of DFT is that the ground state energy can be represented as a functional of the ground state electronic density n_0 which is a quantity that is more easy to work than the many-body wave function. Besides, the ground state energy can be obtained by a variational principle of the ground state electronic density. Khon and Sham [7] used these ideas to formulate a system of N non-interacting fictitious particles that obeys the equations 1.1 (in atomic units)

$$\left[\frac{1}{2}\nabla^2 + V_H + V_{ext} + V_{xc}\right]\Phi_i = \epsilon_i \Phi_i, \qquad n_0 = \sum_{i=1}^{N} |\Phi_i|^2, \tag{1.1}$$

where Φ_i are the Khon-Sham orbitals, ϵ_i the Khon-Sham eigenvalues, V_{ext}

is the external potential, V_H and V_{xc} is the Hartree potential and exchange-correlation potential respectively, that are given by equations 1.2

$$V_H(\mathbf{r}) = \int \frac{n(\mathbf{r}')}{|\mathbf{r} - \mathbf{r}'|} d\mathbf{r}', \qquad V_{xc}(\mathbf{r}) = \frac{\delta E_{xc}[n]}{\delta n(\mathbf{r})}, \tag{1.2}$$

where E_{xc} is the exchange-correlation energy that contains correlation and kinetic effects that are not included in the Hartree potential. The exact form for the E_{xc} is not known, so in order to solve the Khon-Sham equations we have to use approximations for the exchange-correlation potential. One of the most used approximations is the Local-Density-Approximation [7] (LDA), where the exchange-correlation potential is replaced by a homogeneous electron gas that is evaluated locally. With this approximation we have an exchange-correlation potential that is local, where it depends only on the local density in each point of space and is energy independent. We can give more information to this potential if we include the gradient corrections to the local density. This second approximation is called Generalised-Gradient-Approximation [8] (GGA) and despite its corrections to LDA it is still local (or semi-local) and energy independent.

These two approximations, LDA and GGA, are very simple and very successful when describing the ground state properties of many-electron systems. If the exact form of the exchange-correlation potential were known, we would obtain the exact ground state electronic density of the system and have exact ground state results. The discrepancies mentioned above about the electronic and optical properties come from DFT being a ground state theory. The Khon-Sham eigenvalues and orbitals are just mathematical tools without any clear physical meaning with the exception that the square of the Khon-Sham orbitals sums up to the ground state density and the highest occupied Khon-Sham eigenvalue corresponds to the chemical potential for metals [9] or the negative ionization energy for semiconductors and insulators [10]. Nevertheless, we are tempted to identify or interpret the corresponding Khon-Sham eigenvalues spectrum to the excited energies. There is not a justification for this interpretation and that is the reason why DFT shows discrepancies when predicting electronic properties like electronic band-structures. Even with the exact form of the exchange-correlation potential, there is still no reason to use DFT to describe properties related to excited energies. Nevertheless, there are many cases where DFT energy dispersions are in good agreement with experimental data and even if they are not a real description of the system the results can be often interpreted qualitatively.

One of the experimental techniques for measuring the excitation energies which allows us to measure the band gap energies is photo-emission spec-

troscopy or photo-electron spectroscopy. This technique can be performed in two ways: direct photo-emission or inverse photo-emission. The basic idea of the direct photo-emission is to impinge a photon on the sample with energy $\hbar\omega$ which will cause an electron to be ejected with kinetic energy E_{kin}. What happens in this process is that the electron in an occupied band absorbs the photon and then it is removed from the sample with a kinetic energy E_{kin}. During this process the absorbed energy by the electron has to be greater than the work function ϕ which is the energy necessary to remove an electron from the sample to the vacuum. Considering that the initial state with N electrons has energy E_0^N and the final excited state with $N-1$ electrons has energy E_n^{N-1}, then by conservation of energy we get

$$\hbar\omega + E_0^N = E_n^{N-1} + E_{kin} + \phi, \tag{1.3}$$

and knowing that the binding energy of an electron can be considered as $\epsilon_n = E_0^N - E_n^{N-1}$, we can reach the following expression

$$\epsilon_n = E_{kin} + \phi - \hbar\omega, \tag{1.4}$$

allowing us to measure the excitation energy. This process is represented in figure 1.1.

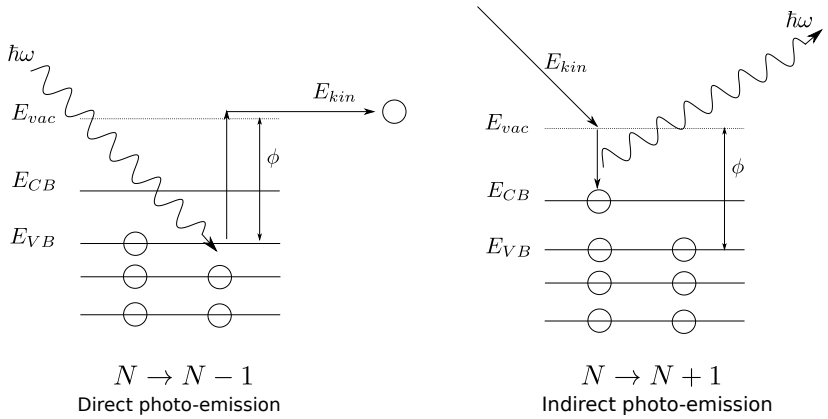

Figure 1.1: Direct photo-emission on the left and inverse photo-emission on the right. E_{kin} is the kinetic energy of the electron, $\hbar\omega$ the photon energy, E_{VB} and E_{CB} is the energy of the last valence band and first conduction band respectively, ϕ is the work function which is the energy necessary to remove the electron from the sample to the vacuum with E_{vac} being the vacuum energy.

In the inverse photo-emission, also represented in figure 1.1, an electron is injected to the sample with a kinetic energy E_{kin}. After that the electron

will go to a lower energy in the conduction band emitting a photon with energy $\hbar\omega$. In this case the binding energy is defined as $\epsilon_n = E_n^{N+1} - E_0^N$. These two processes fail to be a reliable description of the reality because the ejection and injection of electrons in the sample is a many-body problem where the electrons are correlated with each other by Coulomb interactions. The electrons are not independent particles, and there are many complex interactions as phonon and defect scattering that are not considered in these photo-emission process. Still, we can give more reliability to this process when considering the screening effect, which is a very important effect that should be considered in electron interactions. If we consider the screening process, where the electron repulses the other electrons creating a positive cloud charge that "screens" the electron, we can still describe the photo-emission process with the quasi-independent picture. But this time we are considering not the bare electron, but the electron surrounded by the cloud of positive charge that we call a quasi-particle as we can see in figure 1.2 for the electron addition case.

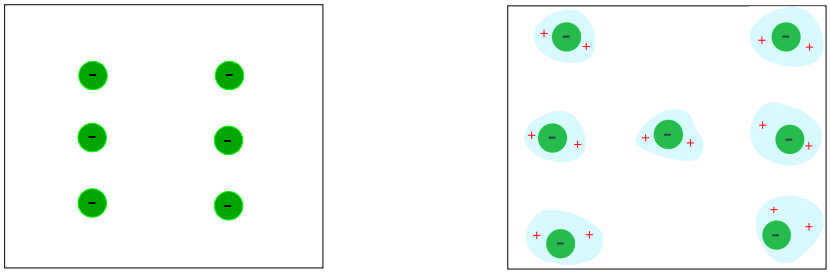

N $\qquad\qquad$ $N \to N+1$

Figure 1.2: In the left picture we have a system of N electrons interacting via Coulomb potential. In the second picture, an electron is added to the system. The new electron will repulse the other electrons, polarizing the system. This polarization creates a positive cloud charge that surrounds the electrons. The electrons are not bare electrons anymore because the positive cloud charge and the electron behave as one which we call quasi-particle. The interactions between the quasi-particles are not Coulomb interactions but interactions by a weaker potential called the screened Coulomb potential.

A many-body theoretical formulation that is related to adding or removing quasi-particles of a system where the initial state has energy E_0^N and the final excited state have energies $E_i^{N\pm1}$ is the Green's function formalism. With this formalism we can find the mathematical description of the quasi-particles which allows us to determine the excitation energies and many other important properties like quasi-particles life times. Such mathematical

description requires the knowledge of the quasi-particle self-energy operator Σ that provides all information about exchange and correlation effects. The problem now is to calculate this quantity, which is far more complex than any quantity in DFT. We will see that with Hedin's equations [11, 12] it is possible to reach a very useful approximation for calculating Σ and determine the excited properties of any material. That approximation is called the GW approximation [11, 12] where the Σ is approximated in the following way

$$\Sigma \approx GW, \tag{1.5}$$

where G is the Green's function and W is the screened Coulomb interaction. In the figure 1.3 we can understand the motivation of the GW approximation:

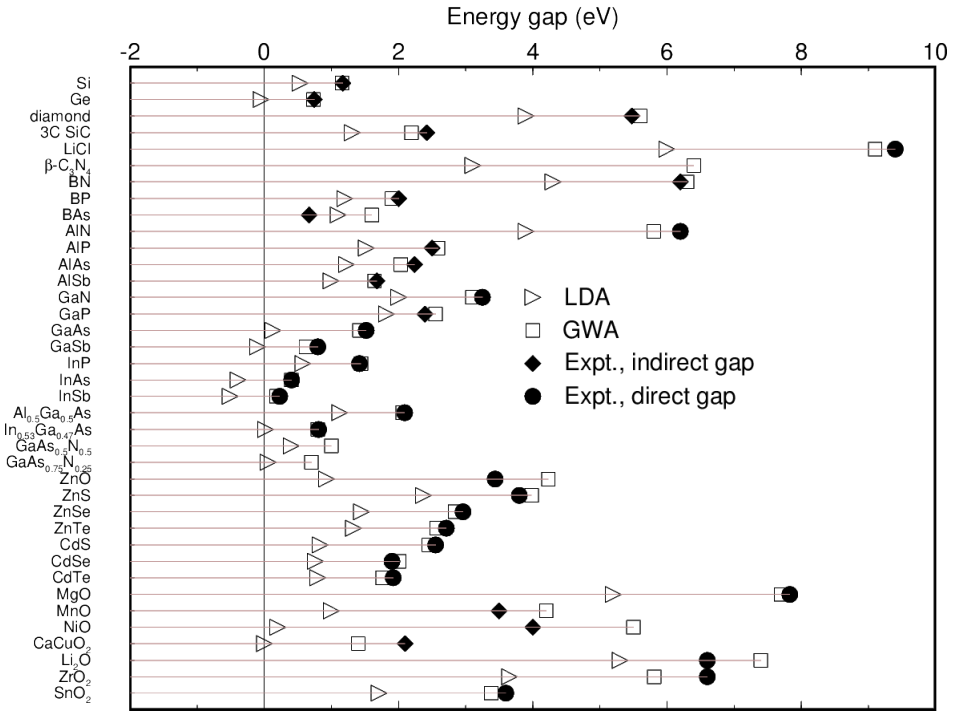

Figure 1.3: Comparison of the band gap values obtained by LDA and by the GW approximation (GWA) with experimental data. Taken from reference [13].

There is still something very important that is missing in this approximation. If we use it to calculate optical properties we still have some bad descriptions when compared to experiments. The reason is the excitonic effects that are being ignored. The electron-hole interactions are very important to describe the optical properties of materials like semiconductors and

insulators which have considerable gaps. The solution is to do calculations with the Bethe-Salpeter equation [14,15] (BSE) which takes into account the electron-hole interactions like screening and exchange. In figure 1.4 we can see the motivation for using the BSE equation to describe the absorption spectrum.

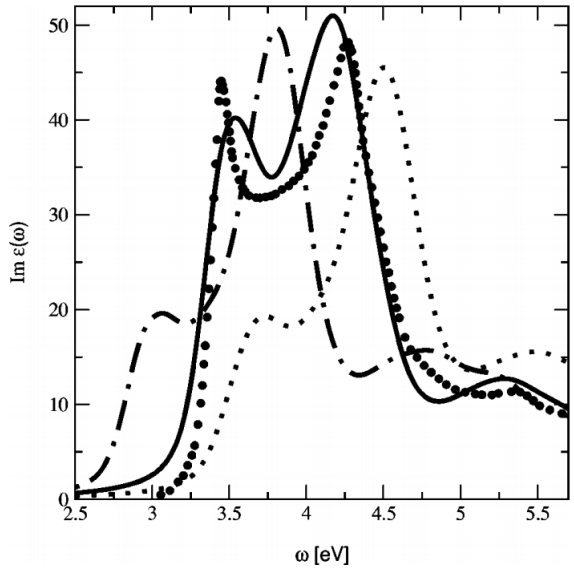

Figure 1.4: Absorption spectrum of silicon. The black dots are the experimental data, the dashed-dot curve is the Random-Phase-Approximation (RPA) which can be obtained by DFT, the dotted curve is obtained by *GW*-RPA which includes the quasi-particle corrections but does not include the excitonic interactions, the solid curve is obtained by the BSE which include the quasi-particle corrections and excitonic effects. This graphic is taken from [16].

An introduction to Green's function, *GW* approximation and BSE formalism is presented in the chapter 2. In the chapter 3 an explanation of how these methods can be implemented numerically in order to perform computational calculations is given. Then we have two chapters for two different bidimensional materials: Bidimensional hexagonal-boron nitride (h-BN) and phosphorene. We will apply the DFT, *GW* approximation and BSE computational techniques to these materials in order to study their electronic an optical properties. First we give a brief introduction to every material. Then we perform DFT and *GW* calculations and discuss the results. Finally we perform BSE equations to calculate optical properties. In the chapter Conclusions and outlook we give a summarized discussion of all the results obtained for the different materials.

Chapter 2

Theoretical Background

We saw in the Introduction chapter that it is not reliable to describe photo-emission spectroscopy by considering that the electrons are independent particles. The reason for this is that photo-emission is a many-body problem and electrons are correlated with each other by Coulomb forces. It is very difficult to solve a many-body problem with real strong interacting particles but, fortunately for us, we can solve it by considering fictitious weakly interacting particles. We call this particles "quasi-particles". One of the best techniques to solve the many-body problem is using the Green's function formalism. In this chapter we give an introduction to Green's function where we show it's properties and usefulness. Then we show that with the Green's function formalism we can construct an approximation, the GW approximation [11, 12], that takes into account the dynamical potential with screening of the quasi-particles and determines the self-energy operator, which is the operator that contains the exchange-correlations effects of these particles. With the knowledge of the self-energy operator we can determine the quasi-particles energy spectrum, which are the excitation energies that give us the electronic band-structures. Finally we talk about the Bethe-Salpeter equation [14, 15] (BSE) which takes into account the excitonic effects that are very important to describe the optical properties.

2.1 Introduction to Green's function

Here we give a brief introduction to the main properties of Green's function. Most of the theory that is written in this section is based on the literature in references [17–19], so it is recommended to consult those references if the reader wants to understand the concepts with more detail.

2.1.1 One particle Green's function as a propagator

The Green's function for one particle is defined by the following equation

$$iG_{\alpha\beta}(\mathbf{r},t;\mathbf{r}',t') = \frac{\langle\Psi_0^N|\, T\left[\hat{\psi}_\alpha(\mathbf{r},t)\hat{\psi}_\beta^\dagger(\mathbf{r}',t')\right]|\Psi_0^N\rangle}{\langle\Psi_0^N|\Psi_0^N\rangle}, \tag{2.1}$$

where $|\Psi_0^N\rangle$ is the many-body Heisenberg ground state of the interacting system with N particles that satisfies equation $\hat{H}\Psi_0^N = E\Psi_0^N$ with $\hat{H}$ being the many-body Hamiltonian, and $\hat{\psi}_\alpha$ and $\hat{\psi}_\beta^\dagger$ are the Heisenberg destruction and creation operators respectively. The spin indices, α and β, are written explicitly and can take two values, up or down for fermions. Everything that is presented in this chapter is about fermions and not bosons. The T that appears in equation 2.1 is called the time-ordering operator and in this particular case it operates in the following way

$$T\left[\hat{\psi}_\alpha(\mathbf{r},t)\hat{\psi}_\beta^\dagger(\mathbf{r}',t')\right] = \hat{\psi}_\alpha(\mathbf{r},t)\hat{\psi}_\beta^\dagger(\mathbf{r}',t')\theta(t-t') \; -\hat{\psi}_\beta^\dagger(\mathbf{r}',t')\hat{\psi}_\alpha(\mathbf{r},t)\theta(t'-t), \tag{2.2}$$

where θ is the Heaviside function. The time-ordering operator in general orders the operators with the highest value in time to the left, until the ascending order is achieved. It adds a factor of $(-1)^P$ for P interchanges of the fermion operators. In the above case where we have $t' > t$, we have to do one interchange between the two operators, so we have to add the $(-1)^1 = -1$ factor. With this definition we can rewrite equation 2.1 in the following way:

$$iG_{\alpha\beta}(\mathbf{r}t;\mathbf{r}'t') = \begin{cases} \dfrac{\langle\Psi_0^N|\,\hat{\psi}_\alpha(\mathbf{r}t)\hat{\psi}_\beta^\dagger(\mathbf{r}'t')\,|\Psi_0^N\rangle}{\langle\Psi_0^N|\Psi_0^N\rangle} & t > t' \\ -\dfrac{\langle\Psi_0^N|\,\hat{\psi}_\beta^\dagger(\mathbf{r}'t')\hat{\psi}_\alpha(\mathbf{r}t)\,|\Psi_0^N\rangle}{\langle\Psi_0^N|\Psi_0^N\rangle} & t' > t \end{cases}. \tag{2.3}$$

We can see that Green's function is complex, because it is nothing more than a matrix element of the Heisenberg ground state. These elements are expectation values of the field operators that depends on the coordinates. So Green's function is simply an ordinary function that depends on the coordinates $(\mathbf{r},t)$ and $(\mathbf{r}',t')$. It is possible to show that if the Hamiltonian is time independent then Green's function is translation invariant in time. That can be easily shown knowing that the Heisenberg operator can be written in the following way

$$\hat{\psi}_\alpha(\mathbf{r},t) = e^{i\hat{H}t/\hbar}\hat{\psi}_\alpha(\mathbf{r})e^{-i\hat{H}t/\hbar}, \tag{2.4}$$

and by using $e^{i\hat{H}t/\hbar}\left|\Psi_0^N\right\rangle = e^{iEt/\hbar}\left|\Psi_0^N\right\rangle$ we will obtain a Green's function that depends on the coordinates $(\mathbf{r}, \mathbf{r}', \tau)$, where $\tau = t - t'$. The equation 2.3 will be expressed as

$$iG_{\alpha\beta}(\mathbf{r}, \mathbf{r}', \tau) = \begin{cases} e^{iE\tau/\hbar}\dfrac{\left\langle\Psi_0^N\right|\hat{\psi}_\alpha(\mathbf{r})e^{i\hat{H}\tau/\hbar}\hat{\psi}_\beta^\dagger(\mathbf{r}')\left|\Psi_0^N\right\rangle}{\left\langle\Psi_0^N|\Psi_0^N\right\rangle} & t > t' \\ -e^{-iE\tau/\hbar}\dfrac{\left\langle\Psi_0^N\right|\hat{\psi}_\beta^\dagger(\mathbf{r}')e^{i\hat{H}\tau/\hbar}\hat{\psi}_\alpha(\mathbf{r})\left|\Psi_0^N\right\rangle}{\left\langle\Psi_0^N|\Psi_0^N\right\rangle} & t' > t \end{cases}. \tag{2.5}$$

where $e^{iE\tau/\hbar}$ is just a complex number. Looking to the expression of equation 2.3, we can observe that Green's function is identical to a propagator. For $t > t'$, Green's function give us the probability amplitude for the propagation of an additional electron from the coordinates $(\mathbf{r}', t')$ to $(\mathbf{r}, t)$. For the case $t' > t$, we have the propagation of an additional hole from the position $(\mathbf{r}', t')$ to $(\mathbf{r}, t)$. This process can be more easily understood if we work in the Schrödinger picture, with the Heisenberg and Schrödinger states being related by the following expression

$$\left|\Psi_H\right\rangle = \hat{U}(t, t')\left|\Psi_S(t)\right\rangle, \tag{2.6}$$

where the time-evolution operator is given by $\hat{U}(t, t') = e^{-i\hat{H}(t-t')/\hbar}$. A particle can be created in the point $(\mathbf{r}', t')$ by applying the creation operator $\hat{\psi}_\beta^\dagger(\mathbf{r}')$ on the Schrödinger state $|\Psi_S(t')\rangle$. Then it will propagate in time according to $\hat{U}(t, t')$. For $t > t'$, the overlap of this state with $\hat{\psi}_\alpha^\dagger(\mathbf{r})\left|\Psi_S(t)\right\rangle$ has the following expression

$$\left\langle\Psi_S(t)\right|\hat{\psi}_\alpha(\mathbf{r})U(t, t')\hat{\psi}_\beta^\dagger(\mathbf{r}')\left|\Psi_S(t')\right\rangle, \tag{2.7}$$

and it is the probability amplitude at a later time t for finding an additional electron at the sate $\Psi_S(t)$. The reverse, $t' > t$ is the probability amplitude to find an additional hole at later time t' in the ground state $\Psi_S(t')$. The holes can be considered as electrons going backwards in time. So we understand now the physical meaning of the one particle Green's function as a propagator.

2.1.2 One particle Green's function and observables

It is possible to calculate very interesting properties with the one particle Green's function of equation 2.1. We are talking for example about the expectation value of any single particle operator of a ground state system. Using the following definition for the single particle operator,

$$\hat{O} = \int d^3\mathbf{r} \sum_{\alpha\beta} \psi_\beta^\dagger(\mathbf{r})O(\mathbf{r})_{\alpha\beta}\psi_\alpha(\mathbf{r}) \tag{2.8}$$

and knowing that the expectation value of the operator is given by $\langle \Psi_0^N | \hat{O} | \Psi_0^N \rangle$ it is possible to get the following expression:

$$\langle \hat{O} \rangle = \pm i \int d^3\mathbf{r} \lim_{t' \to t^+} \lim_{\mathbf{r}' \to \mathbf{r}} \sum_{\alpha\beta} O(\mathbf{r})_{\alpha\beta} G_{\alpha\beta}(\mathbf{r}, t; \mathbf{r}' t') \tag{2.9}$$

where t^+ is an infinitesimal greater than t to ensure that the operators are in the correct order (seeing the derivation on the literature, it is easy to see that the case considered is $t' > t$, so the positive infinitesimal assures that). With the expression 2.9 we can express single-particle operators depending on the one particle Green's function. For example the total kinetic energy can be expressed as:

$$\langle \hat{T} \rangle = \pm i \int d^3\mathbf{r} \lim_{\mathbf{r}' \to \mathbf{r}} \left[-\frac{\hbar^2 \nabla^2}{2m} \operatorname{tr} G(\mathbf{r}, t; \mathbf{r}' t^+) \right] \tag{2.10}$$

where tr is the trace. It is also possible to show that the ground state energy depends on the one particle Green's function, where the expression is given by (see literature in reference [17] for full derivation):

$$E = \langle \hat{T} + \hat{V} \rangle = \langle \hat{H} \rangle = \pm \frac{1}{2} i \int d^3\mathbf{r} \lim_{t' \to t^+} \lim_{\mathbf{r}' \to \mathbf{r}} \left[i\hbar \frac{\partial}{\partial t} - \frac{\hbar^2 \nabla^2}{2m} \right] \operatorname{tr} G(\mathbf{r}, t; \mathbf{r}' t'). \tag{2.11}$$

It is clear that one particle Green's function can give us access to really interesting observable properties, like the ground state energy. Unlike DFT, we can obtain the exact ground sate energy as a functional of the Green's function, but it is much more complex to calculate as we will see in the next sections.

There is one very important property that one particle Green's function can give us. The excitation spectrum of the system, that is going to be introduced in the next section.

2.1.3 Excitation spectrum

To simplify our calculations, let us consider that the Heisenberg ground state in equation 2.1 is normalized, that is, $\langle \Psi_0^N | \Psi_0^N \rangle = 1$, and the spins are implicit from now on. If we insert the completeness relation $\sum_n |\Psi_n\rangle \langle \Psi_n| = 1$ between the two operators in equation 2.5 we end up with the following equation

$$\begin{aligned} iG(\mathbf{r}, \mathbf{r}', \tau) = &\sum_n \left[e^{-i(E_n - E)t/h} \theta(\tau) \langle \Psi_0^N | \hat{\psi}(\mathbf{r}) | \Psi_n \rangle \langle \Psi_n | \hat{\psi}^\dagger(\mathbf{r}') | \Psi_0^N \rangle \right] \\ &- \sum_n \left[-e^{i(E_n - E)t/h} \theta(\tau) \langle \Psi_0^N | \hat{\psi}^\dagger(\mathbf{r}') | \Psi_n \rangle \langle \Psi_n | \hat{\psi}(\mathbf{r}) | \Psi_0^N \rangle \right], \end{aligned} \tag{2.12}$$

where equation $H|\Psi_n\rangle = E_n|\Psi_n\rangle$ was used. We can see in the first term the state $|\Psi_n\rangle$ corresponds to a state with $N+1$ particles, considering that the ground state has N particles. That is because $\langle\Psi_0^N|\hat{\psi}(r)|\Psi_n\rangle\langle\Psi_n|\hat{\psi}^\dagger(r)|\Psi_0^N\rangle = \left|\langle\Psi_0^N|\hat{\psi}(r)|\Psi_n\rangle\right|^2$, which means that the state $|\Psi_n\rangle$ must contain one more particle than state $|\Psi_0^N\rangle$. So we can define the state $|\Psi_n\rangle$ in the first term as $|\Psi_n^{N+1}\rangle$. In the second term we have the opposite, so we define the state $|\Psi_n\rangle$ as $|\Psi_n^{N-1}\rangle$. Using equations $H|\Psi_n^{N\pm1}\rangle = E_n^{N\pm1}|\Psi_n^{N\pm1}\rangle$ and $H|\Psi_0^N\rangle = E|\Psi_0^N\rangle$, we can rewrite equation 2.12 in following way:

$$iG(\mathbf{r},\mathbf{r}',\tau) = \sum_n \theta(\tau)\Psi_n^{N+1}(\mathbf{r})\Psi_n^{*N+1}(\mathbf{r}')e^{-i\epsilon_n^{N+1}\tau/\hbar} - \sum_n \theta(-\tau)\Psi_n^{N-1}(\mathbf{r})\Psi_n^{*N-1}(\mathbf{r}')e^{-i\epsilon_n^{N-1}\tau/\hbar}, \quad (2.13)$$

where

$$\Psi_n^{N+1}(r) = \langle\Psi_0^N|\hat{\psi}(r)|\Psi_n^{N+1}\rangle \qquad \Psi_n^{N-1}(r) = \langle\Psi_n^{N-1}|\hat{\psi}(r)|\Psi_0^N\rangle\,, \quad (2.14)$$

and

$$\epsilon_n^{N+1} = E_n^{N+1} - E \qquad \epsilon_n^{N-1} = E - E_n^{N-1}. \quad (2.15)$$

If we perform a Fourier transform in frequency space of equation 2.13, we obtain the following equation

$$G(\mathbf{r},\mathbf{r}',\omega) = \sum_n \frac{\Psi_n^{N+1}(\mathbf{r})\Psi_n^{*N+1}(\mathbf{r}')}{\hbar\omega - \epsilon_n^{N+1} + i\eta} + \sum_n \frac{\Psi_n^{N-1}(\mathbf{r})\Psi_n^{*N-1}(\mathbf{r}')}{\hbar\omega - \epsilon_n^{N+1} - i\eta} \quad (2.16)$$

where η is a positive infinitesimal. The denominator in the first term of equation 2.16 can be expressed in the following way

$$\hbar\omega - \epsilon_n^{N+1} = \hbar\omega - (E_n^{N+1} - E^{N+1}) - (E^{N+1} - E). \quad (2.17)$$

The quantity $E^{N+1} - E$ represents the change of energy on ground state when a extra particle is added to the system with N particles. If the volume is kept constant, this change of energy is just the chemical potential μ. The quantity $E_n^{N+1} - E^{N+1} = \epsilon_{n_{ex}}^{N+1}$ is the excitation energy of the $N+1$ system. We can do the same analogy for the second denominator and finally rewrite equation 2.16 in the following way:

$$G(\mathbf{r},\mathbf{r}',\omega) = \sum_n \frac{\Psi_n^{N+1}(\mathbf{r})\Psi_n^{*N+1}(\mathbf{r}')}{\hbar\omega - \mu - \epsilon_{n_{ex}}^{N+1} + i\eta} + \sum_n \frac{\Psi_n^{N-1}(\mathbf{r})\Psi_n^{*N-1}(\mathbf{r}')}{\hbar\omega - \mu - \epsilon_{n_{ex}}^{N-1} - i\eta} \quad (2.18)$$

This equation shows that the one particle Green's function has poles at the exact excitation energies of the interacting system. For energies above the

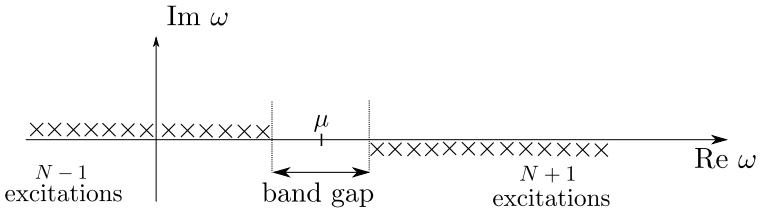

Figure 2.1: Singularities of equation 2.18 in the complex plane. For $N+1$ excitations we have energies above the chemical potential and the poles (crosses) are below the real axis. For $N-1$ excitations we have energies below the chemical potential and the poles (crosses) are above the real axis.

chemical potential we have poles that are slightly below the real axis. For energies below the chemical potential we have poles that are slightly above the real axis. These singularities are shown in figure 2.1. With the excitation energies one can obtain the energy spectrum of the material.

2.1.4 Dyson's equation and quasi-particle equation

Is is clear that Green's function gives us very useful properties that are observable. Still we have to solve the Green's function for a many-body interacting system where the Hamiltonian in the second quantization has the following expression (spins are implicit from now on):

$$\hat{H} = \int \hat{\psi}^\dagger(\mathbf{r})\hat{h}_0(\mathbf{r})\hat{\psi}(\mathbf{r})d^3r + \frac{1}{2}\int \hat{\psi}^\dagger(\mathbf{r})\hat{\psi}^\dagger(\mathbf{r}')v(\mathbf{r},\mathbf{r}')\hat{\psi}(\mathbf{r}')\hat{\psi}(\mathbf{r})d^3rd^3r', \quad (2.19)$$

where $v(\mathbf{r},\mathbf{r}')$ is the Coulomb interaction. The quantity $\hat{h}_0$ is the one-particle operator defined as

$$\hat{h}_0(\mathbf{r}) = -\frac{\nabla^2}{2} + V_{ext}(\mathbf{r}), \quad (2.20)$$

with V_{ext} being the potential created by the ions. From the Heisenberg equation of motion

$$i\frac{\partial\hat{\psi}(\mathbf{r},t)}{\partial t} = \left[\hat{\psi}(\mathbf{r},t),\hat{H}\right], \quad (2.21)$$

and using equation 2.1 with the ground state normalized, we can obtain the following equation,

$$\left[i\frac{\partial}{\partial t} - \hat{h}_0(\mathbf{r})\right]G(\mathbf{r},t,\mathbf{r}',t') = \delta(\mathbf{r}-\mathbf{r}')\delta(t-t') - i\int v(\mathbf{r},\mathbf{r}'')\left\langle\Psi_0^N\right|\hat{T}\left[\hat{\psi}^\dagger(\mathbf{r}'',t)\hat{\psi}(\mathbf{r}'',t)\psi(\mathbf{r},t)\psi^\dagger(\mathbf{r}',t')\right]\left|\Psi_0^N\right\rangle d^3r'', \quad (2.22)$$

which is equation of motion for the Green's function. As we can observe in the second term of the right hand side of equation 2.22, there is a quantity that involves the interaction between two particles. That quantity is the two-particle Green's function and it is defined as

$$G(,r_1t_1,\mathbf{r_2},t_2;\mathbf{r'_1},t'_1,\mathbf{r'_2},t'_2) = \\ (-i)^2\frac{\langle\Psi_0^N|\,\hat{T}\left[\hat{\psi}(\mathbf{r_1},t_1)\hat{\psi}(\mathbf{r_2},t_2)\hat{\psi}^\dagger(\mathbf{r'_2},t'_2)\hat{\psi}^\dagger(\mathbf{r'_1},t'_1)\right]|\Psi_0^N\rangle}{\langle\Psi_0^N|\Psi_0^N\rangle}. \quad (2.23)$$

We can see that equation 2.22 depends on the Green's function for two-particles which means that equation of motion of Green's function for two-particles depends on the Green's function for three-particles and so on. So we have an hierarchy of equations which are very complicated to solve. There is a very special and useful identity that allows us to get rid of the two-particle Green's function. This is what we want because we are interested only on the one-particle Green's function properties. That identity comes from the Schwinger's functional derivative method [20, 21] and it is defines as

$$\int\Sigma(\mathbf{r}t;\mathbf{r}'',t'')G(\mathbf{r}'',t'',\mathbf{r}',t')dr''dt'' + V_H(\mathbf{r},t)G(\mathbf{r},t;\mathbf{r}',t') \\ = i\int v(\mathbf{r},\mathbf{r}'')\,\langle\Psi_0^N|\,\hat{T}\left[\hat{\psi}^\dagger(\mathbf{r}'',t)\hat{\psi}(\mathbf{r}'',t)\psi(\mathbf{r},t)\psi^\dagger(\mathbf{r}',t')\right]|\Psi_0^N\rangle\,d^3r'', \quad (2.24)$$

where the Hartree Potential is defined as

$$V_H(\mathbf{r},t) = \int v(\mathbf{r},t;\mathbf{r}'',t'')n(\mathbf{r}'',t'';\mathbf{r}'',t''+\eta),dr'' \quad (2.25)$$

with η being an infinitesimal positive of time and the density is defined as $n(\mathbf{r}''t'';\mathbf{r}''t''+\eta) = iG(\mathbf{r}''t'';\mathbf{r}''t''+\eta)$. This allows us to rewrite 2.22 as

$$\left[i\frac{\partial}{\partial t} - \hat{h}(\mathbf{r})\right]G(\mathbf{r},t,\mathbf{r}',t') \\ = \delta(\mathbf{r}-\mathbf{r}')\delta(t-t') + \int\Sigma(\mathbf{r},t;\mathbf{r}'',t'')G(\mathbf{r}'',t'',\mathbf{r}',t')dr''dt'', \quad (2.26)$$

which is Dyson's equation and the $\hat{h}$ is the sum of the $\hat{h}_0$ and the Hartree potential. The Σ is the self-energy operator and we can solve the Green's function exactly if we know the exact form of self-energy operator. In order to understand the physical meaning of self-energy operator one can do a Fourier transformation of equation 2.26 in the frequency domain and then use equation 2.16 to obtain

$$\hat{h}\,(\mathbf{r})\,\Psi_n(\mathbf{r}) + \int\Sigma(\mathbf{r},\mathbf{r}';\epsilon_n)\Psi_n(\mathbf{r}')d^3\mathbf{r}' = \epsilon_n\Psi_n(\mathbf{r}), \quad (2.27)$$

which is often called the quasi-particle equation. We can see that Σ acts as a non-local frequency dependent potential on a Schrödinger like equation. This equation is not a mean-field formalism because Σ is a dynamical operator and takes into account all many-body exchange and correlations effects beyond Hartree potential. This means that Ψ_n and ϵ_n are not single-particle quantities. They are actually properties of the many-body problem as defined in equation 2.14 and 2.15.

If we consider a non-interacting system, the self-energy vanishes, that is, $\Sigma = 0$. This allows us to obtain 2.26

$$\left[i\frac{\partial}{\partial t} - \hat{h}(\mathbf{r})\right] G_0(\mathbf{r}, t; \mathbf{r}', t') = \delta(\mathbf{r} - \mathbf{r}')\delta(t - t'), \tag{2.28}$$

where G_0 is the Green's function for a non-interacting system. If we multiply 2.26 for G_0 and 2.28 by G one can rewrite the Dyson's equation as

$$\begin{aligned} G(\mathbf{r}, t; \mathbf{r}', t') &= G_0(\mathbf{r}, t; \mathbf{r}', t') \\ &+ \int G_0(\mathbf{r}, t; \mathbf{r}'', t'')\Sigma(\mathbf{r}'', t''; \mathbf{r}''', t''')G(\mathbf{r}''', t'''; \mathbf{r}', t')dr''dr''', \end{aligned} \tag{2.29}$$

which can be represented diagrammatically by Feynman's diagrams in figure 2.2.

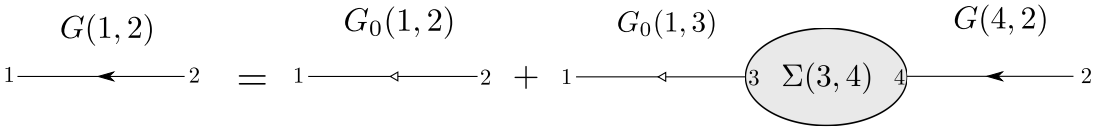

Figure 2.2: Feynman's diagram representation to the Dyson's equation. The notation used is represented in equation 2.34.

If our system is homogeneous stationary and non-magnetic (which means that G and Σ are diagonal in respect to spin indices) it is possible to make a Fourier transformation of 2.29 to get an algebraic equation

$$G(\mathbf{k}, \omega) = G_0(\mathbf{k}, \omega) + G_0(\mathbf{k}, \omega)\Sigma(\mathbf{k}, \omega)G(\mathbf{k}, \omega), \tag{2.30}$$

allowing us to obtain

$$G(\mathbf{k}, \omega) = \left[G_0(\mathbf{k}, \omega)^{-1} - \Sigma(\mathbf{k}, \omega)\right]^{-1}. \tag{2.31}$$

The beauty of equation above is that when we do an approximation for the self-energy we are actually calculating an infinite subseries of the perturbation series. This happens because those series are all contained in the self-energy

operator. The self-energy can be considered as everything that is beyond the non-interacting Green's function. The equation 2.31 can be written symbolic as

$$G^{-1} = i\frac{\partial}{\partial t} - \hat{h} - \Sigma, \tag{2.32}$$

which holds even if G and Σ are non-diagonal [18].

It is important to note that the non-interacting Green's function G_0 is in principle known because it is the Green's function for the non-interacting Hamiltonian. Then we can calculate self-consistently the G by using equation 2.31. For that is necessary to know how to calculate or approximate the self-energy operator.

2.2 Hedin's Equations: GW Approximation

In this section the Hedin's equations [11, 12] are presented, which is where the GW approximation takes place. Hedin's equations provides a set of integral-differential equations that gives the explicit form for the self-energy operator. The essential idea is that the self-energy can be expressed in terms of the screened Coulomb potential W instead of the bare Coulomb potential v. When expanding the self-energy in terms of v, it is known that the series will be divergent for metals and even if it converges, the convergence ratio becomes poor with the increase of the system polarizability [11, 12]. On the contrary, when expanding in terms of the screened potential W, the first order gives good results for system with large polarizability. The reason for this is the fact that W is weaker than v because of the dielectric medium which is polarized. This happens because of the screening effect. We will see that despite of the Hedin's equations looking like a self-consistent procedure, we have to iterate them analytically. This is where the GW approximation emerges.

2.2.1 Hedin's equations

We saw that equation 2.22 can be solved by using an identity that comes from using the Schwinger's functional derivative method which can be done by introducing an external potential $U(\mathbf{r}, t)$ that will be set to zero at the end. The first term of equation of motion 2.26 is now

$$\left[i\frac{\partial}{\partial t} - \hat{h}(\mathbf{r}) - U(\mathbf{r}, t)\right] G(\mathbf{r}, t; \mathbf{r}', t'). \tag{2.33}$$

In order to reduce the number of primes on equations that will be written later, one can use the following notation:

$$1 = (\mathbf{r}, t)\,, \quad 2 = (\mathbf{r}', t')\,, \quad 3 = (\mathbf{r}'', t'')\,, \tag{2.34}$$

$$\delta(1,2) = \delta\left(\mathbf{r} - \mathbf{r}'\right)\delta\left(t - t'\right), \tag{2.35}$$

$$v(1,2) = v\left(\mathbf{r} - \mathbf{r}'\right)\delta\left(t - t'\right), \tag{2.36}$$

$$\int d1 = \int d^3\mathbf{r} \int_{-\infty}^{+\infty} dt, \tag{2.37}$$

$$1^+ = (\mathbf{r}, t + \eta)\,, \tag{2.38}$$

where η is a positive infinitesimal. The equation of motion of the Green's function can be rewritten in the new notation as

$$\left[i\frac{\partial}{\partial t_1} - \hat{H}_0(1)\right] G(1,2) - \int \Sigma(1,3)G(3,2)d3 = \delta(1,2), \tag{2.39}$$

where $\hat{H}_0 = \hat{h} + U$. This is nothing more than the Dyson's equation of 2.26 but with the external potential included. The question now is how can one evaluate Σ. This is where the Schwinger's functional derivative method takes place. It is possible to show that [22]

$$\frac{\delta G(1,2)}{\delta U(3)}\Big|_{U=0} = G(1,2)G(3,3^+) - G(1,3,2,3^+) \tag{2.40}$$

and now we understand how we got rid of the two-particle Green's function in the previous section. We can see that if we look again to equation 2.22 with the two-particle Green's function and use identity 2.40, one can obtain the following equality

$$\begin{aligned} -i\int v(1^+,3)G(1,3,2,3^+)d3 \\ = -i\int v(1,3)G(3,3^+)G(1,2)d3 \;\; + i\int v(1^+,3)\frac{\delta G(1,2)}{\delta U(3)}\; d3 \end{aligned} \tag{2.41}$$

where $n(3,3^+) = iG(3,3^+)$ is the density. From equation 2.41 and 2.39 we arrive at:

$$\int \Sigma(1,3)G(3,2)d3 = i\int v(1^+,3)\frac{\delta G(1,2)}{\delta U(3)}\; d3 \tag{2.42}$$

Now using identity [22]

$$\int d3G(1,3)G^{-1}(3,2) = \int d3G^{-1}(1,3)G(3,2) = \delta(1,2), \tag{2.43}$$

we can reach the following expression

$$\Sigma(1,2) = i \int v(1^+,3) \frac{\delta G(1,4)}{\delta U(3)} G^{-1}(4,2)\ d3\ d4 \tag{2.44}$$

Finally, using this identity [22]

$$\int \frac{\delta \left(G(1,4)G^{-1}(4,2)\right)}{\delta U(3)} d4 = \int \frac{\delta G(1,4)}{\delta U(3)} G^{-1}(4,2) d4 + \int \frac{\delta G^{-1}(4,2)}{\delta U(3)} G(1,4) d4 = 0 \tag{2.45}$$

it is possible to reach the following expression

$$\begin{aligned} \Sigma(1,2) &= -i \int v(1,3^+) G(1,4) \frac{\delta G^{-1}(4,2)}{\delta U(3)} d3\ d4 \\ &= -i \int\ v(1,3^+) G(1,4) \frac{\delta G^{-1}(4,2)}{\delta V(5)} \frac{\delta V(5)}{\delta U(3)} d3\ d4\ d5 \end{aligned} \tag{2.46}$$

This allows us to reach the final expression for Σ which is given by

$$\Sigma(1,2) = i \int W(1^+,3) G(1,4) \Gamma(4,2,3) d3\ d4, \tag{2.47}$$

where the self-energy is expressed in terms of W, the screened Coulomb potential and the Γ vertex function. Before talking about the explicit expressions for the W and Γ let us define some important quantities that can be obtained using the functional differentiation. The response function is defined as

$$R(1,2) = \frac{\delta n(1)}{\delta U(2)}\Big|_{U=0}. \tag{2.48}$$

which is how the density changes due to the external field. The following quantity

$$V(1) = U(1) + \int v(1,3) R(3,2) U(2)\ d2\ d3, \tag{2.49}$$

is the effective or average potential and it is the sum of the Hartree potential and the external potential.

The inverse dielectric function is a very important quantity because it measures the screening in the system. It can be obtained classically by

differentiating the average potential due to a small variation in the external potential,

$$\epsilon^{-1}(1,2) = \frac{\delta V(1)}{\delta U(2)}\Big|_{U=0} = \delta(1,2) + \int v(1,3)R(3,2)d3. \tag{2.50}$$

The other quantity is the polarization function or polarizability which is the change of density upon the average potential, and it is given by

$$P(1,2) = \frac{\delta n(1)}{\delta V(2)}\Big|_{U=0}. \tag{2.51}$$

Using the following identity

$$\epsilon^{-1} = \frac{\delta V}{\delta U} = 1 + v\frac{\delta n}{\delta V}\frac{\delta V}{\delta U}, \tag{2.52}$$

we can invert the epsilon function in equation 2.50 and obtain

$$\epsilon(1,2) = \delta(1,2) - \int v(1,3)P(3,2)d3. \tag{2.53}$$

Now we know that the potential that an electron at position 1 feels due to the presence of a test charge at position 2 including the effects of the polarization of the electrons is the screened potential given by

$$W(1,2) = \int \epsilon^{-1}(1,3)v(3,2)d3 \tag{2.54}$$

Using equation identity 2.52, we can rewrite the inverse epsilon function as

$$\begin{aligned}\epsilon^{-1}(1,3) = \delta(1,3) + v(1,4)\frac{\delta n(3)}{\delta V(4)}\frac{\delta V(4)}{\delta U(3)} \\ = \delta(1,3) + v(1,4)P(3,4)\epsilon^{-1}(4,3).\end{aligned} \tag{2.55}$$

The screened potential can now be rewritten as

$$W(1,2) = \int \epsilon^{-1}(1,3)v(3,2)d3 = v(1,2) + \int v(1,3)P(3,4)W(4,2)d3d4. \tag{2.56}$$

The vertex function Γ in the expression 2.47, is defined as

$$\Gamma(1,2,3) = -\frac{\delta G^{-1}(1,2)}{\delta V(3)}\Big|_{U=0}, \tag{2.57}$$

If we use the identity 2.31 taking into account the inclusion of the external potential, we can obtain the following expression

$$G^{-1}(1,2) = i\frac{\partial}{\partial t_1} - H_0(1) - \Sigma(1,2) = G_0^{-1}(1,2) - U(1)\delta(1,2) - \Sigma(1,2). \quad (2.58)$$

With the expressions of 2.57 and 2.58 we get

$$\begin{aligned}\Gamma(1,2,3) = -\frac{\delta}{\delta V(3)}\left[G_0^{-1}(1,2) - U(1)\delta(1,2) - \Sigma(1,2)\right] \\ = \delta(1,2)\delta(1,3) + \frac{\delta\Sigma(1,2)}{\delta V(3)}, \quad (2.59)\end{aligned}$$

noting that the $V(3)$ is the sum of the external potential and the Hartree potential that is included in the $G_0^{-1}(1,2)$. We can rewrite equation 2.59 in the following way

$$\begin{aligned}\Gamma(1,2,3) &= \delta(1,2)\delta(1,3) + \int \frac{\delta\Sigma(1,2)}{\delta G(4,5)}\frac{\delta G(4,5)}{\delta V(3)} d4\ d5 \\ &= \delta(1,2)\delta(1,3) + \int \frac{\delta\Sigma(1,2)}{\delta G(4,5)} G(4,6)\Gamma(6,7,3)G(7,6) d4\ d5\ d6\ d7 \quad (2.60)\end{aligned}$$

where the identity 2.45 was used. The same can be done to the polarization function. Considering $n(1) = -i\hbar G(1,1^+)$, we can obtain:

$$\begin{aligned}P(1,2) = -i\frac{\partial G(1,1^+)}{\partial V(2)} = -i\int G(1,3)\frac{\partial G^{-1}(3,4)}{\partial V(2)} G(4,2) d3\ d4 \\ = -i\int G(1,3)\Gamma(3,4,2)G(4,1) d3\ d4. \quad (2.61)\end{aligned}$$

So in summary we get the following set of integral-differential equations:

$$G(1,2) = G_0(1,2) + \int G_0(1,3)\Sigma(3,4)G(4,2)d3\ d4, \tag{2.62}$$

$$\Sigma(1,2) = i\int W(1,3^+)G(1,4)\Gamma(4,2,3)d3\ d4, \tag{2.63}$$

$$\Gamma(1,2,3) = \delta(1,2)\delta(1,3) + \int \frac{\delta\Sigma(1,2)}{\delta G(4,5)}G(5,6)G(7,4)\Gamma(6,7,3)d4\ d5\ d6\ d7, \tag{2.64}$$

$$P(1,2) = -i\int G(1,3)G(4,1)\Gamma(3,4,2)d3\ d4, \tag{2.65}$$

$$\epsilon(1,2) = \delta(1,2) - \int v(1,3)P(3,2)d3, \tag{2.66}$$

$$W(1,2) = \int \epsilon^{-1}(1,3)v(3,2)d3, \tag{2.67}$$

which are called the Hedin's equations. These equations can be solved self-consistently in order to solve the many-body problem. The idea is to start with some value for Σ and then evaluate G and Γ which allows us to evaluate P. With P we can calculate the W and finally the new Σ. We can do this procedure over and over again until self-consistency is achieved. Figure 2.3 represents the cylce procedure of the self-consistent loop of Hedin's equations.

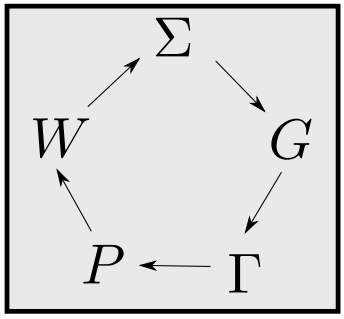

Figure 2.3: Cycle procedure of the self-consistent loop of Hedin's equations. First we start with an approximation for Σ and then we cam calculate the other quantities until the new Σ is calculated. The cycle can be repeated over and over again until self-consistency is achieved.

2.2.2 GW approximation

Hedin proposed in the first iteration to consider the $\Sigma = 0$ which means that $G = G_0$. With this consideration the vertex function is simply

$$\Gamma(1,2,3) = \delta(1,2)\delta(1,3). \tag{2.68}$$

Then we can calculate the polarization function that is given by

$$P(1,2) = -iG(1,2)G(2,1), \tag{2.69}$$

which allows us to determine the epsilon function and W. Finally we can calculate the Σ which is given by

$$\Sigma(1,2) = iG(1,2)W(1^+,2). \tag{2.70}$$

The equation 2.70 is the GW approximation. This is nothing more than the contribution of order one of the Σ that comes from the zero order contribution of the other terms. Then we can get the first order contribution for G and for the vertex function Γ. The later is done by doing the functional derivative and obtain $\Gamma(1,2,3) = iG(1,3)G(3,2)W(1^+2)$ which allow us then to obtain the second order contribution of Σ, which is given by

$$i^2 \int W(1^+,3)G(1,4)G(4,3)W(4^+,2)d3d4. \tag{2.71}$$

We can see that this gets very complicated because the second contribution from Γ now arises from the first and second contribution of Σ.

2.2.3 G_0W_0

One of the complexity of the GW approximation is to stop in the first order contribution

$$\Sigma(1,2) = iG(1,2)W(1^+,2). \tag{2.72}$$

and neglect the contribution from the other orders. Of course this is of very practical interest for computational calculations because we are not treating the GW approximation as a self-consistent procedure. Now the problem is how to calculate the G_0 of the first iteration. We can take advantage of DFT calculations and calculate the Green's function G_0 using singe-particle quantities as we will see in the next chapter. This allows us to determine the polarizability which is given by $P_0 = -iG_0(1,2)G_0(2,1)$. This is called the Random-Phase-Approximation (RPA). Finally we obtain the W_0 which

$$\Sigma = 0$$
$$\downarrow$$
$$G(1,2) = G_0(1,2)$$
$$\downarrow$$
$$P_0(1,2) = -iG_0(1,2)G_0(2,1)$$
$$\downarrow$$
$$\epsilon_0(1,2) = \delta(1,2) - \int v(1,3)P_0(3,2)$$
$$\downarrow$$
$$W_0(1,2) = \int \epsilon_0^{-1}(1,3)v(3,2)$$
$$\downarrow$$
$$\Sigma(1,2) = iG_0(1,2)W_0(1^+,2)$$

Figure 2.4: G_0W_0 scheme. We start by considering that $\Sigma = 0$ which allows us to calculate the other quantities till the new Σ is calculated. This new Σ is given by $iG_0(1,2)W_0(1^+,2)$.

is the screened potential calculated from the RPA. Then we calculate Σ and this procedure is called single-shot or one-shot GW (G_0W_0):

$$\Sigma(1,2) = iG_0(1,2)W_0(1^+,2). \tag{2.73}$$

Figure 2.4 represents the G_0W_0 scheme.

In the next chapter we will talk about the numerical implementation where one can understand how to relate the quasi-particles energies and the Khon-Sham energies.

Despite it's simplicity, G_0W_0 approximation is very successful when describing the electronic excitations in solids and molecules [23, 24]. More insight about this approximation will be given in the chapter Implementation of GW approximation and BSE, where we can understand better what is the significance of the quantities that are involved in this approximation.

2.3 Bethe-Salpeter Equation (BSE)

To describe the absorption spectrum of the materials one has to take into account the excitonic interactions, that is, electron-hole interactions. These interactions are not included in the GW approximation, which is why we

don't have reliable descriptions of optical properties with the RPA [6]. It is important then to consider the two-particle Green's function instead of one-particle. The two-particle Green's function has the following expression

$$G(1,2,3,4) = (-i)^2 \langle \Psi_0^N | \hat{T} \left[\hat{\psi}(1)\hat{\psi}(2)\hat{\psi}^\dagger(4)\hat{\psi}^\dagger(3) \right] | \Psi_0^N \rangle , \tag{2.74}$$

considering that ground state is normalized.

2.3.1 Four-point reducible polarizability

Let's introduce the quantity L which is called the four-point reducible polarizability and has the following expression

$$L(1,2,3,4) = L_0(1,2,3,4) - G(1,2,3,4), \tag{2.75}$$

where L_0 is the non-interacting four-point reducible polarizability and it is defined as $L_0(1,2,3,4) = iG(1,3)G(4,2)$. We can see that L describes the the propagation of electron and hole separately which is the L_0 quantity, minus the coupled propagation of electron and hole which is the two-particle G. Using the equation 2.40, we can rewrite the L function as

$$L(1,2,3,4) = -i\frac{\delta G(1,2)}{\delta U(3,4)}. \tag{2.76}$$

Using the identity 2.45, we can rewrite 2.76 as

$$\begin{aligned} L(1,2,3,4) &= -i\frac{\delta G(1,2)}{\delta U(3,4)} = +i \int G(1,5)\frac{\delta G^{-1}(5,6)}{\delta U(3,4)} G(6,2) d5d6 \\ &= +i \int G(1,5)\frac{\delta \left[G_0^{-1}(5,6) - U(5)\delta(5,6) - \Sigma(5,6) \right]}{\delta U(3,4)} G(6,3) d5d6, \end{aligned} \tag{2.77}$$

and because the only term in G_0^{-1} that depends on the external potential is the Hartree potential, we have

$$\begin{aligned} L(1,2,3,4) &= +i \int G(1,5)\frac{\delta \left[V_H(5)\delta(5,6) - U(5)\delta(5,6) - \Sigma(5,6) \right]}{\delta U(3,4)} G(6,2) d5d6, \\ &= -iG(1,3)G(4,2) + i \int G(1,5)G(6,2)\frac{\delta \left[V_H(5)\delta(5,6) - \Sigma(5,6) \right]}{\delta U(3,4)} d5d6 \\ &= L_0(1,2,3,4) + i \int G(1,5)G(6,2) \left[\frac{\delta V_H(5)\delta(5,6)}{\delta G(7,8)} - \frac{\delta \Sigma(5,6)}{\delta G(7,8)} \right] \frac{G(7,8)}{\delta U(3,4)} d5d6d7d8. \end{aligned} \tag{2.78}$$

Using the definition of the Hartee potential in equation 2.25, we can obtain the following expression

$$L(1,2,3,4) = L_0(1,2,3,4) + \int L_0(1,2,5,6)\left[v(5,7)\delta(5,6)\delta(7,8) - i\frac{\delta\Sigma(5,6)}{\delta G(7,8)}\right] L(7,8,3,4)d5d6d7d8, \tag{2.79}$$

which is called the Bethe-Salpeter equation (BSE) [14, 15]. This equation is very similar to the Dyson equation. If one consider the following quantity

$$\Xi(5,6,7,8) = \left[v(5,7)\delta(5,6)\delta(7,8) - i\frac{\delta\Sigma(5,6)}{\delta G(7,8)}\right], \tag{2.80}$$

which is called the kernel of the BSE, we can rewrite the BSE in the following way

$$L(1,2,3,4) = L_0(1,2,3,4) + \int L_0(1,2,5,6)\Xi(5,6,7,8)L(7,8,3,4)d5d6d7d8. \tag{2.81}$$

It's diagrammatic representation can be seen in figure 2.5.

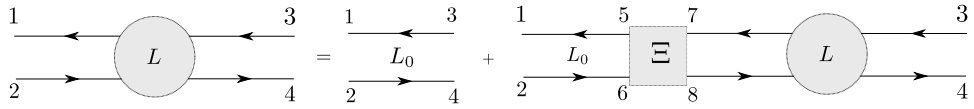

Figure 2.5: Feynman diagram of the Bethe-Salpeter equation. Sometimes it is called Dyson's equation, see similarity with figure 2.2.

One fact that should be noted is that we just need the two-point reducible polarizabilty that is given by

$$\chi(1,2) = -i\frac{\delta G(1,1^+)}{\delta U(2,2)} \tag{2.82}$$

to describe the optical properties. The problem is that there is not a closed equation to this quantity in the Green's function formalism, which means we need to evaluate the four-point reducible polarizability. We have to calculate the L function which depends on Σ. Let's recall the GW approximation where

$$\Sigma(1,2) = iG(1,2)W(1^+,2). \tag{2.83}$$

Using the identity

$$\frac{\delta(GW)}{\delta G} = W + G\frac{\delta W}{\delta G}. \tag{2.84}$$

and noting that $\frac{\delta W}{\delta G} \approx 0$ because the variation of screening with the excitation can be neglected [25–27], one can rewrite the kernel of BSE as

$$\Xi(1,2,3,4) = v(1,3)\delta(1,2)\delta(3,4) - \delta(1,3)\delta(2,4)W(1,2). \tag{2.85}$$

We can now rewrite the BSE equation as

$$L = L_0 + L_0(v - W)L. \tag{2.86}$$

Looking at the above equation, we can see that it represents the sum of the electron-hole exchange energy without screening, which is the term with the four-point extension of the Coulomb interaction v, plus the electron-hole attractive four-point extended screened Coulomb interaction. The diagrammatic representation of the kernel is shown in figure 2.6

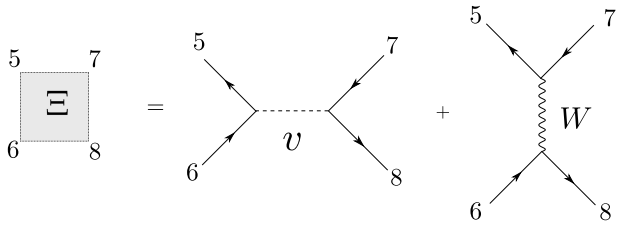

Figure 2.6: Feynman diagram of the kernel of the BSE. See figure 2.5 for BSE. The quantity v is the repulsion part and represents the Coulomb interaction. The quantity W is the electron-hole attractive screened Coulomb interaction.

2.3.2 Connection to absorption spectrum

So far we know how to calculate the BSE, but we did not explicit it's connection with absorption spectrum. That can be seen in the macroscopic dielectric function which is given in the plane-wave basis by equation

$$\epsilon_M(\mathbf{q},\omega) = 1 - \lim_{\mathbf{q}\to 0}\left[v_{\mathbf{G}=0}(\mathbf{q})\int d\mathbf{r}d\mathbf{r}' e^{-i\mathbf{q}(\mathbf{r}-\mathbf{r}')}\chi(\mathbf{r},\mathbf{r}';\omega)\right], \tag{2.87}$$

where $\mathbf{q}$ is a vector of the first Brillouin zone and $\mathbf{G}$ is a reciprocal vector. The absorption spectrum is simply the imaginary part of the macroscopic dielectric function. To calculate this function we have to perform a contraction on the four-point L to obtain the two-point χ, which is defined as

$$\chi(1,2) = L(1,2,1,2), \tag{2.88}$$

allowing us to calculate the absorption spectrum.

Chapter 3

Implementation of GW approximation and BSE

In this chapter we present how the GW [11, 12] approximation and BSE [14,15] is implemented numerically in order to do computational calculations. Most of the content that is written here was taken from [16, 19].

3.1 Numerical implementation GW approximation

As refereed in the previous chapter, in the first iteration of GW approximation we have to know how to determine G_0. Normally we use the single-particle quantities from DFT calculations to calculate G_0 which is the non-interacting Green's function. After that we can calculate the screened potential by using the RPA which allows us to obtain the self-energy operator. We can stop here and use the results for the quasi-particle calculations. This is called the single-shot or one-shot GW and its numerical implementation will be explained below.

3.1.1 Single-shot GW or G_0W_0

If one Fourier transforms equation 2.72, which in real space has the expression

$$\Sigma(\mathbf{r}, \mathbf{r}', \tau) = iG_0(\mathbf{r}, \mathbf{r}', \tau + \omega')W(\mathbf{r}, \mathbf{r}', \tau + t), \tag{3.1}$$

we obtain

$$\Sigma(\mathbf{r}, \mathbf{r}', \omega) = \frac{i}{2\pi} \int d\omega' G_0(\mathbf{r}, \mathbf{r}', \omega + \omega')W(\mathbf{r}, \mathbf{r}', \omega')e^{i\omega'\eta}. \tag{3.2}$$

where η is an infinitesimal positive to ensure the correct order. We saw that Green's function can be defined as

$$G(\mathbf{r}', \mathbf{r}', \omega) = \sum_n \frac{\Psi_n(\mathbf{r})\Psi_n^*(\mathbf{r}')}{\omega - \epsilon_n - i\eta \ \mathrm{sgn}(\epsilon_n - \mu)}, \tag{3.3}$$

where Ψ_n are the quasi-particle wave-functions, ϵ_n are the eigenvalues, μ chemical potential and $\eta \to 0^+$ an infinitesimal positive. We are not writing the quasi-particle functions and wave-functions with the superscripts $N \pm 1$ to simplify the next equations. It is important to remember that when $\epsilon_n > \mu$ we are dealing with a system of $N-1$ particles and for $\epsilon_n < \mu$ we are dealing with a system of $N+1$ particles.

As a starting point, we can use the solutions and energies obtained by the Khon-Sham equations which we define as ϕ_n^{KS} and ϵ_n^{KS} respectively. Doing the following approximations in equation 3.3,

$$\Psi_n \approx \phi_n^{KS} \quad \epsilon_n \approx \epsilon_n^{KS},$$

we can now calculate $G = G_0$ which is given by,

$$G_0(\mathbf{r}, \mathbf{r}', \omega) = \sum_n \frac{\phi_n^{KS}(\mathbf{r})\phi_n^{*KS}(\mathbf{r}')}{\omega - \epsilon_n^{KS} - i\eta \mathrm{sgn}(\epsilon_n^{KS} - \mu)}. \tag{3.4}$$

This is one of the best guesses that can be made for the initial G_0 function. The function W is given by equation 2.67, where the dielectric function is given by equation 2.66. Thus, it is necessary to calculate the polarizability function P. This function is given by

$$P = P_0 = -iG_0(1,2)G_0(2,1),$$

and it has the physical meaning that electrons respond to the total field (external plus induced) as non-interacting particles. This is called the RPA as referred in the previous chapter. If we perform a Fourier transformation and use equation 3.4, we obtain

$$P_0(\mathbf{r}, \mathbf{r}', \omega) = \sum_{spin} \sum_{n}^{occupied} \sum_{m}^{unoccupied} \phi_n^{KS}(\mathbf{r})\phi_m^{*KS}(\mathbf{r})\phi_n^{*KS}(\mathbf{r}')\phi_m^{KS}(\mathbf{r}') \times \left(\frac{1}{\omega + \epsilon_n^{KS} - \epsilon_m^{KS} + i\eta} - \frac{1}{\omega - \epsilon_n^{KS} + \epsilon_m^{KS} - i\eta} \right). \tag{3.5}$$

With the function P_0 calculated, we can calculate the dielectric function and consequently the potential W. We call it W_0 because it was calculated with the RPA. Finally we have the approximation

$$\Sigma(1,2) = iG(1,2)W(1,2) = iG_0(1,2)W_0(1,2).$$

With the self-energy operator Σ calculated, we can return to the quasi-particle equation 2.27 to calculate the quasi-particle energies. This equation can be rewritten in the following notation,

$$\left[h + \Sigma(\epsilon_n^{GW})\right] |\Psi_n^{GW}\rangle = \epsilon_n^{GW} |\Psi_n^{GW}\rangle \,. \tag{3.6}$$

Of course we have a problem that is the Σ depends on the quasi-particle energies, which are the energies that we want to calculate. To solve this problem, we use the first order perturbation, where the perturbation is the difference between the Σ of the G_0W_0 and the exchange-correlation potential used in the Khon-Sham calculation (V_{xc}^{KS}). First we approximate $\Psi_n^{GW} \approx \phi_n^{KS}$ to treat the G_0W_0 as perturbation to the Khon-Sham solutions. It is reported that this approximation is harmless [28]. Then we do the difference between the quasi-particle equation

$$\langle\phi_n^{KS}| \left[h_0 + \Sigma(\epsilon_n^{GW})\right] |\phi_n^{KS}\rangle = \epsilon_n^{GW}, \tag{3.7}$$

with the Khon-Sham equation

$$\langle\phi_n^{KS}| \left[h_0 + V_{xc}^{DFT}\right] |\phi_n^{KS}\rangle = \epsilon_n^{KS}, \tag{3.8}$$

where we can obtain,

$$\epsilon_n^{GW} - \epsilon_n^{KS} = \langle\phi_n^{KS}| \left[\Sigma(\epsilon_n^{GW}) - V_{xc}^{DFT}\right] |\phi_n^{KS}\rangle \,. \tag{3.9}$$

There is still a term that depends on the quasi-particle eigenvalues, $\Sigma(\epsilon_n^{GW})$. What we can do is to consider initially $\epsilon_n^{GW} = \epsilon_n^{KS}$ to compute the quasi-particle energy $\epsilon_n^{GW(0)}$. Then we consider $\epsilon_n^{GW} = \epsilon_n^{GW(0)}$ to compute the new quasi-particle energy $\epsilon_n^{GW(1)}$. The process has to be repeated until self-consistency is achieved. There are many cases where the self-energy is a nearly linear function of ϵ_n^{GW} and we can compute $\Sigma(\epsilon_n^{GW})$ for two grid points and evaluate self-consistent ϵ_n^{GW} by using the Newton's method [28]

$$\epsilon_n^{GW} = \epsilon_n^{GW(0)} + \frac{d\Sigma(\epsilon_n^{GW(0)})}{d\omega} Z_n(\epsilon_n^{GW(0)} - \epsilon_n^{KS}). \tag{3.10}$$

where Z_n is the renormalization factor given by

$$Z_n = \left(1 - \frac{d\Sigma(\epsilon_n^{GW(0)})}{d\omega}\right)^{-1}. \tag{3.11}$$

We can easily see that the most difficult step in this G_0W_0 method is to calculate the self-energy operator, because the other terms can be easily extracted from the DFT calculations. The approximation G_0W_0 can be divided in two parts,

$$\Sigma^{GW} = iG_0W_0 = i\left[G_0v + G_0(W_0 - v)\right] = \Sigma_x^{GW} + \Sigma_c^{GW}, \tag{3.12}$$

where the first term corresponds to the exchange part and it is given by

$$\Sigma_x^{GW}(\mathbf{r},\mathbf{r}',\omega) = \frac{i}{2\pi}\int G_0(\mathbf{r},\mathbf{r}',\omega+\omega')v(\mathbf{r},\mathbf{r}')e^{i\omega'\eta}d\omega', \tag{3.13}$$

the second term corresponds to the correlation part and it is given by

$$\Sigma_c^{GW}(\mathbf{r},\mathbf{r}',\omega) = \frac{i}{2\pi}\int G_0(\mathbf{r},\mathbf{r}',\omega+\omega')\left[W(\mathbf{r},\mathbf{r}',\omega') - v(\mathbf{r},\mathbf{r}')\right]d\omega'. \tag{3.14}$$

The first term can be calculated analytically and it is nothing more than the Hartree-Fock exchange,

$$\langle\phi_n^{KS}|\,\Sigma_x^{GW}\,|\phi_n^{KS}\rangle = -\frac{e^2}{4\pi\epsilon_0}\sum_m^{occupied}\int\frac{\phi_n^{*KS}(\mathbf{r})\phi_m^{KS}(\mathbf{r})\phi_m^{*KS}(\mathbf{r}')\phi_n^{KS}(\mathbf{r}')}{|\mathbf{r}-\mathbf{r}'|}d^3r_1d^3r_2. \tag{3.15}$$

In the other hand, the second term has to be calculated numerically and it is the responsible for the computational expensiveness. In the following list the steps to calculate the quasi-particle energies are shown:

1. Self-consistent calculation using DFT to obtain the Khon-Sham functions ϕ_n^{KS} and the corresponding energies ϵ_n^{KS}. In this point it is possible to determine G_0 and calculate the term of equation 3.15.

2. Calculate the polarizability functions P with the RPA. Then the dielectric functions is calculated by equation 2.66.

3. With dielectric function calculated it is possible to calculate W by equation 2.67.

4. Calculate the correlation term of equation 3.14 by a numerical contour integration on the complex frequency plane.

5. With the self-energy operator calculated, we can calculate the quasi-particle energies according equation 3.10.

3.1.2 Plasmon Pole Approximation

One of the steps that is very computational expensive is the determination of W of equation 3.14. It is easy to see that to evaluate $\Sigma_c^{GW}(\omega)$ one has to know $W(\omega')$ for each frequency point, which means that we have to evaluate the dielectric function for all frequencies. There is an approximation, Plasmon Pole Approximation (PPA), where we can obtain a model for the dielectric

function with the frequency dependence using few parameters. The idea is to calculate the static dielectric function and then extend it to finite frequencies. There are many proposed models for PPA. The model used in this work is the model proposed by Hybertson e Louie [28]. It is explained with more detail in the next chapter. It is important to note that PPA has to be used carefully and we have to check its validity. This can be done by comparing it with a calculation evaluated in a frequency grid. Nevertheless, in materials like semiconductors or insulators PPA often gives good results [28].

3.2 Numerical implementation of BSE

In this section we will introduce briefly how the BSE is implemented numerically with the help of a GW calculation. For more detail one can consult references [15, 16, 29].

3.2.1 How to calculate BSE with GW

We saw in the previous chapter that the BSE is given by:

$$L = L_0 + L_0(V - W)L, \tag{3.16}$$

where L is the four-point reducible polarizability and L_0 the non-interacting four-point reducible polarizability. The first consideration that is made before calculating the BSE is to assume that W is static. This approximation is harmless because dynamical effects in the electron-hole W and G tend to cancel each other and we can ignore them [15, 29]. This allows us to do the following tranformations:

$$W(1,2) \to W(\mathbf{r}, \mathbf{r}', t - t') \to W(\mathbf{r}, \mathbf{r}')\delta(t - t'), \tag{3.17}$$

and

$$L(1,2,3,4) \to L(\mathbf{r}, \mathbf{r}', \mathbf{r}'', \mathbf{r}''', t - t') \to L(\mathbf{r}, \mathbf{r}', \mathbf{r}'', \mathbf{r}''', \omega). \tag{3.18}$$

Next step is to take advantage of the fact that only a limited number of electron-hole pairs contribute to the excitations. One can then change the basis to the transition space (which is the product of single-particle orbitals) where any four-pint quantity $S(\mathbf{r}, \mathbf{r}', \mathbf{r}'', \mathbf{r}''', \omega)$ can be written as

$$S(\mathbf{r}, \mathbf{r}', \mathbf{r}'', \mathbf{r}''', \omega) = \sum_{n_1 n_2 n_3 n_4} \Psi^*_{n_1}(\mathbf{r})\Psi_{n_2}(\mathbf{r}')\Psi_{n_3}(\mathbf{r}'')\Psi^*_{n_4}(\mathbf{r}''')S_{(n_1 n_2)(n_3 n_4)}(\omega), \tag{3.19}$$

where

$$S_{(n_1n_2)(n_3n_4)}(\omega) = \int S(\mathbf{r},\mathbf{r}',\mathbf{r}'',\mathbf{r}''',\omega)\Psi_{n_1}(\mathbf{r})\Psi^*_{n_2}(\mathbf{r}')\Psi^*_{n_3}(\mathbf{r}'')\Psi_{n_4}(\mathbf{r}''')drdr'dr''dr'''. \tag{3.20}$$

The n_i is the index for the band, **k**-point and spin. The expansion set of single-particle orbitals has to form a complete basis set in the Hilbert space. The non-interacting polarizability can be expressed now as

$$L_0(\mathbf{r},\mathbf{r}',\mathbf{r}'',\mathbf{r}''',\omega) = \sum_{n,n'} \frac{f_n - f_{n'}}{\epsilon_n - \epsilon_{n'} - \omega}\Psi^*_n(\mathbf{r})\Psi_{n'}(\mathbf{r}')\Psi_n(\mathbf{r}'')\Psi^*_{n'}(\mathbf{r}''') \tag{3.21}$$

and it is diagonal in the electron-hole basis,

$$L_{0(n_1n_2)(n_3n_4)}(\omega) = -\frac{f_{n_1} - f_{n_2}}{\epsilon_{n_1} - \epsilon_{n_2} + \omega}\delta_{n_1,n_3}\delta_{n_2,n_4} \tag{3.22}$$

With this transformation, the BSE equation can now be rewritten as

$$L_{(n_1n_2)(n_3n_4)}(\omega) = L_{0(n_1n_2)}(\omega)\left[\delta_{n_1,n_3}\delta_{n_2,n_4} + \sum_{n_5n_6} K_{(n_1n_2)(n_5n_6)}(\omega)L_{(n_5n_6)(n_3n_4)}(\omega)\right]. \tag{3.23}$$

To solve the above equation we have to invert it for each frequency. The problem it that the matrix L can be very large and the inversion of equation 3.23 can become impossible. Nevertheless, we can reformulate this problem to an effective eigenvalue problem. By rewriting equation 3.23 as

$$\sum_{n_5n_6}\left[\delta_{n_1,n_5}\delta_{n_2,n_6} - L_{0(n_1n_2)}(\omega)K_{(n_1n_2)(n_5n_6)}(\omega)\right]L_{(n_5n_6)(n_3n_4)}(\omega) = L_{0(n_1n_2)}(\omega), \tag{3.24}$$

and using equation 3.22, one can obtain

$$\sum_{n_5n_6}\left[(\epsilon_{n_2} - \epsilon_{n_1} - \omega)\,\delta_{n_1,n_5}\delta_{n_2,n_6} - (f_{n_2} - f_{n_1})\,K_{(n_1n_2)(n_5n_6)}(\omega)\right] \times L_{(n_5n_6)(n_3n_4)}(\omega) = f_{n_2} - f_{n_1}. \tag{3.25}$$

We considered above that W is static which means that K is also static. This allows us to define an effective frequency independent Hamiltonian with the expression

$$H^{ex}_{(n_1n_2)(n_5n_6)} = (\epsilon_{n_2} - \epsilon_{n_1})\,\delta_{n_1,n_5}\delta_{n_2,n_6} - (f_{n_2} - f_{n_1})\,K_{(n_1n_2)(n_5n_6)}. \tag{3.26}$$

where we define it as the excitonic Hamiltonian. The BSE can now be reduced to

$$L_{(n_1n_2)(n_3n_4)}(\omega) = [H^{ex} - I\omega]^{-1}_{(n_1n_2)(n_3n_4)} (f_{n_2} - f_{n_1}), \tag{3.27}$$

where I is the identity matrix with same size as the excitonic Hamiltonian. In the spectral representation we have

$$[H^{ex} - I\omega]^{-1}_{(n_1n_2)(n_3n_4)} = \sum_{\lambda\lambda'} \frac{A^{\lambda}_{n_1n_2} A^{\lambda'}_{n_3n_4}}{E^{\lambda} - \omega} N^{-1}_{\lambda\lambda'} \tag{3.28}$$

where the eigenvalues E^{λ} and eigenvectors A^{λ} given by

$$H^{ex} A^{\lambda} = E^{\lambda} A^{\lambda}, \tag{3.29}$$

are the excitonic energies and eigenstates respectively. The $N_{\lambda\lambda'}$ is the overlap matrix defined by

$$N_{\lambda\lambda'} \equiv \sum_{n_1n_2} [A^{\lambda}_{n_1n_2}]^* A^{\lambda'}_{n_1n_2}. \tag{3.30}$$

The Hamiltonian of equation 3.29 is in general not Hermitian. There is an approximation, Tamm-Dancoff approximation, where only the electron-hole pairs at positive energies are considered and the Hamiltonian becomes hermitian. With this approximation the excitonic hamiltonian has the following expression with the **k**-point dependence explicit

$$H = (\epsilon_{nk} - \epsilon_{n'k}) \delta_{mn} \delta_{n'm} \delta_{\mathbf{k}\mathbf{k}'} + [2V_{nn'\mathbf{k},mm'\mathbf{k}'} - W_{nn'\mathbf{k},mm'\mathbf{k}'}], \tag{3.31}$$

where the $\epsilon_{n(m)\mathbf{k}}$ can be the Khon-Sham eigenvalues or quasiparticles energies. Finally the imaginary part of the dielectric function can be obtained by

$$\mathrm{Im}\epsilon_M = \lim_{q\to 0} \frac{8\pi^2}{q^2 V} \sum_{\lambda} \sum_{nn'\mathbf{k}} |\langle n'\mathbf{k} - \mathbf{q}| e^{i\mathbf{q}\mathbf{r}} |n\mathbf{k}\rangle A^{\lambda}_{n'n\mathbf{k}}|^2 \delta((E_{n\mathbf{k}-\mathbf{q}} - E_{n'\mathbf{k}}) - \omega) \tag{3.32}$$

3.3 Important facts about the G_0W_0 and BSE calculations.

In this section we give some important topics about the G_0W_0 and BSE calculations that are done using the BerkeleyGW [30] package. More details are presented in appendix B.

3.3.1 G_0W_0 calculations

The G_0W_0 calculations that will be shown in chapters 4 and 5 use the Generalised-Plasmon-Pole (GPP) model proposed by Hybertson e Louie [28].

In that model, we first have to compute the static polarizability matrix of equation B.1.

We have to construct the matrix elements $M_{nn'}$ where n is the number of occupied bands and n' the number of empty bands. For computing these elements we have to choose a cut-off which we call the dielectric cut-off. The number of empty bands is the number of bands used for the summation of the static polarizability matrix. The last empty band used in this summation has to be consistent with the dielectric cut-off. So we can choose a number of bands for the summation and then choose the dielectric cut-off to be consistent with the energy of the last empty band.

When we have all parameters needed to construct the static polarizability matrix, we can compute the static dielectric matrix and calculate equation B.9. The next step is to calculate Σ which is divided in two parts, equation B.14 and equation B.15. These equations also depend on the plane-wave matrix elements $M_{nn'}$, and equation B.15 has a band summation that has infinite terms.

So we have to choose a cut-off for the plane-wave matrix elements and a number of bands for equation B.15. Because the cut-off for the plane-wave matrix elements cannot be greater than the dielectric cut-off, we use that cut-off in equations B.14 and B.15 (which depend on the plane-wave matrix elements).

The number of bands for equation B.15, which is the number of bands in the Coulomb hole calculation, is a parameter that has to be converged.

To summarize, we have to study convergence for two parameters, the number of bands used for the construction of the plane-wave matrix elements of equation B.2 and the number of bands in the Coulomb hole calculation of equation B.15.

3.3.2 BSE calculations

First we have to do compute the kernel in a coarse grid of **k**-points using equations B.21 and B.22.

Just like in the dielectric computation, we have to choose a cut-off for and the number of valence and conduction bands for the construction of the matrix M of equations B.21 and B.22. The cut-off is chosen to be the same of the dielectric cut-off used in the G_0W_0 calculation.

The number of valence and conduction bands are convergence parameters that have to be studied.

Finally, we have to choose a coarse grid for the computation of the kernel. We choose the grid for which the G_0W_0 calculation was converged, which is $11 \times 11 \times 1$. After computing the kernel we have to interpolate it in a fine grid to include more **k**-points in the BSE. To do this interpolation we choose the number of valence and conduction bands we want to use for the interpolation.

So the important quantities we have to study are the number of valence and conduction bands to construct the kernel with the coarse grid and the number of **k**-points of the fine grid, and the number of valence and conduction bands in which we want do to the interpolation.

Chapter 4

2D hexagonal boron nitride

4.1 Introduction

The bidimensional (2D) hexagonal boron nitride (h-BN) has gain a lot of attention because of its similarity with graphene. As can be shown in figure 4.1, the structure of 2D h-BN is analogous to graphene, where boron and nitrogen atoms are bound by strong covalent bonds. Like graphene, 2D h-BN has good mechanical properties and high thermal conductivity [31], but it is an insulator with a wide gap greater than 4 eV [32]. Having a wide band gap makes this material good for band gap engineering and chemical functionalization. It was shown that the h-BN can become semiconductor by tuning its gap, which makes it a promising candidate to semiconductor applications [33]. Besides, its high energy gap is good for the realization of ultra-violet lasers [34] and ultrasonic devices [35].

The 2D h-BN is a very recent material, and few works were done to provide a good description of electronic and optical properties of this material. The band gap energy obtained using first principles calculations varies from author to author as we will see. Besides, there is a lack of study about excitonic properties. It is important then to study this material with a reliable description. In this chapter we study the electronic and optical properties of the 2D h-BN using the *GW* approximation [11, 12] and BSE [14, 15].

4.2 DFT calculations

Ab initio Density Functional Theory (DFT) calculations were performed by using the Quantum ESPRESSO package [36]. Plane-wave representation is used. Scalar-relativistic pseudopotentials for both boron and nitrogen atoms were used. The exchange-correlation functional is approximated by

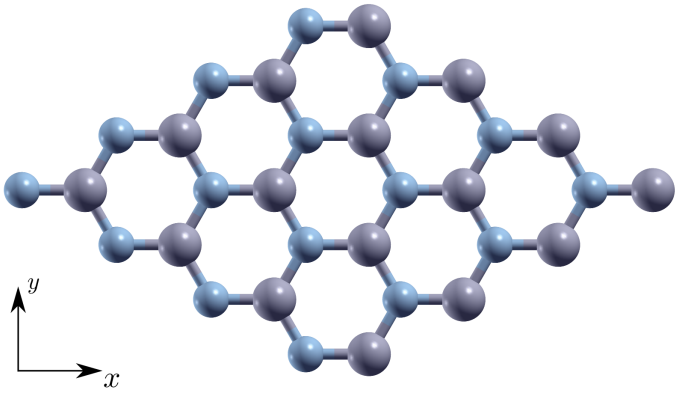

Figure 4.1: Structure of 2D h-BN. The blue colour corresponds to B atoms which are the small ones, while the grey colour corresponds to N atoms.

PBE [37] generalised gradient approximation (GGA). A plane-wave energy cut-off of 80 Ry (1088 eV) was used. The **k**-points mesh was sampled by a Monkhorst-Pack [38] method with convergence at 6× 6× 1. Both the plane-wave energy cut-off and the **k**-points mesh convergence are shown in the figures A.1 and A.2 of appendix A. We have used a super-cell with the vectors represented in table 4.1, which can be seen in figure 4.2. The optimized lattice

Real space	Reciprocal space
$\vec{a}_1 = \frac{\sqrt{3}a}{2}\vec{e}_x + \frac{a}{2}\vec{e}_y$	$\vec{b}_1 = \frac{2\pi}{a\sqrt{3}}\vec{k}_x + \frac{2\pi}{a}\vec{k}_y$
$\vec{a}_2 = \frac{\sqrt{3}a}{2}\vec{e}_x - \frac{a}{2}\vec{e}_y$	$\vec{b}_2 = \frac{2\pi}{a\sqrt{3}}\vec{k}_x - \frac{2\pi}{a}\vec{k}_y$

Table 4.1: Lattice vectors in real space and reciprocal space. The parameter a is the lattice constant.

parameter is $a = 4.78$ bohr and a vacuum size between the layers of $c \geq 15$ bohr is enough to avoid interactions between the periodic images. This study is shown in figure A.3 and A.4 of appendix A. Figure 4.3 shows the electronic band-structure along a chosen **k**-points path. It is easy to see that we obtain a direct band gap at the K point of 4.43 eV and an indirect band gap of 4.56 eV from Γ to K point.

In table 4.2 we summarized the DFT h-BN studies from our work and previous works. In table 4.2 we can see that the lattice constant in in good agreement with the other works. This is expected because DFT predicts with

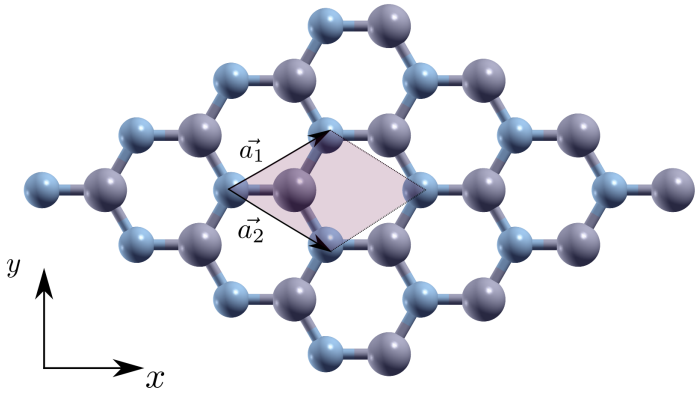

Figure 4.2: The red shadow is the area of the cell used to construct the 2D h-BN structure. The vectors $\vec{a}_1$ and $\vec{a}_2$ are the ones shown in table 4.1.

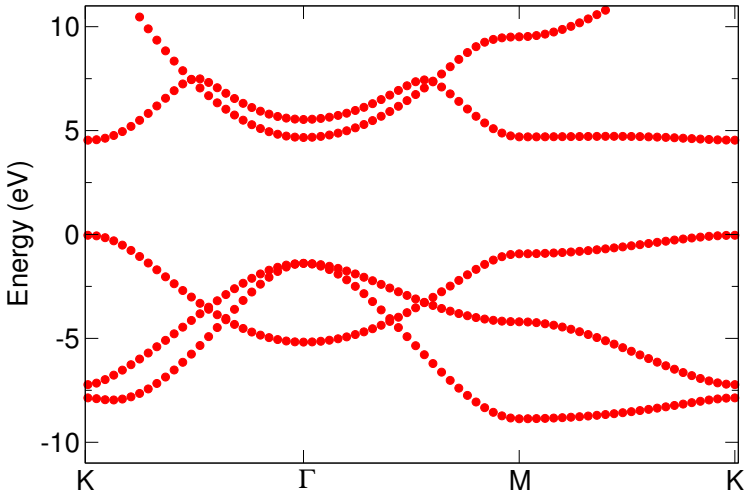

Figure 4.3: Electronic band-structure of 2D h-BN along the path K-Γ-M-K. The exchange-correlation functional is approximated by PBE-GGA.

good precision the lattice constants as mentioned in the chapter 1.

When comparing data from our electronic band-structure with other works, we can some incongruences. First, our band gap is direct at K point and most of the other works present an indirect band gap from Γ to K point. We have tested some other pseudopotentials with different approximations for exchange-correlation functional to see if the problems persists, and we conclude that the indirect and direct nature of the gap is very sensitive to the type of pseudopotential. In the band-structure shown in figure 4.3 the difference between the energy of the lowest conduction band at Γ and K

Reference	XC functional	a [bohr]	D. Gap [eV]	I. Gap [eV]
This Work	GGA	4.78	4.43 (K-K)	4.56 (K-Γ)
[33]	LDA	4.72		4.50
[31]	GGA			4.56 (K-Γ)
[31]	HSE			5.56 (K-Γ)
[39]	GGA	4.74		4.64 (K-Γ)
[40]	GGA	4.74	4.61 (K-K)	

Table 4.2: DFT results from different works including our work. We include the exchange-correlation functional (XC), the lattice constant a, the direct band gap (D. Gap) and the indirect band gap (I. Gap). We could not obtain the lattice constant from the work [31] and the work [33] has obtained an indirect band gap that is not a transition from the (K-Γ).

point is 0.12 eV. This difference is relatively small when compared to the band gap and can vary easily with the choice of the type of pseudopotential. Nevertheless, the calculated band gaps in table 4.2 are not so deviated, ranging from (4.43 to 4.64 eV). The second incongruence comes from the work that used the hybrid functional HSE [41]. We can see that there is a difference of the order of 1.0 eV when compared to the rest of the works. It is well known that at DFT-LDA or DFT-GGA level the band gap energies are underestimated as mentioned in the chapter 1. DFT-HSE level can be used to correct that underestimation [41]. This is a signal that is necessary to do other calculations beyond DFT to have a correct description of the electronic properties.

Experimental data shows band gaps for bidimensional h-BN ranging from 4.6 to 7.0 eV [32]. There are also works that assume that the gap of 2D h-BN is the same as in the bulk h-BN [31]. But despite of that, the direct and indirect band gaps are still not known accurately. The bulk h-BN band gap values varies from 3.6 to 7.1 eV [42]. Besides, it is not clear if this experiments are measuring the fundamental band gap or the optical gap which includes excitonic effects. To accurately calculate the band gap of 2D h-BN is needed. That is the reason why *GW* approximation calculations are fundamental to have a correct description of the electronic band-structures.

We also calculated the absorption spectrum which is proportional to the imaginary part of the macroscopic dielectric function using the post processing code of Quantum ESPRESSO epsilon.x which computes it using the RPA. The Im ϵ_m is shown in figure 4.4, for light polarized along the surface direction. The spectrum is the same for the light polarized along the x or y axis. This graphic will be discussed with more detail in the section 4.4.

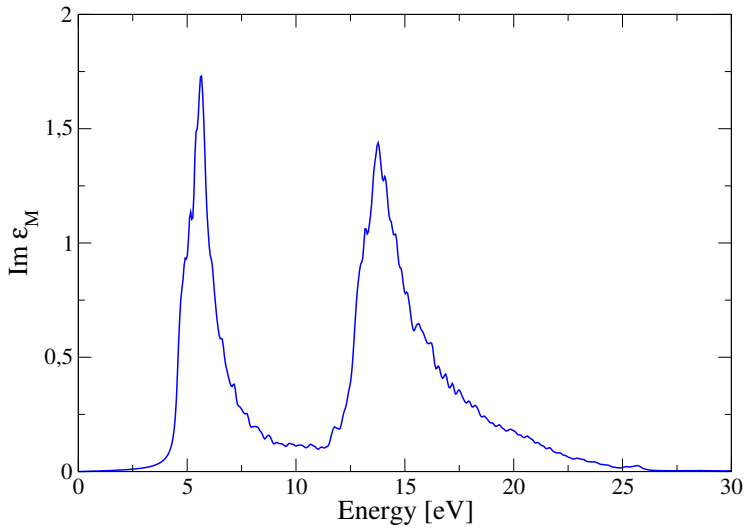

Figure 4.4: Imaginary part of the macroscopic dielectric function at DFT-GGA+RPA level of bidimensional h-BN for light polarized along the direction parallel to the surface. Local field effects are not included. A gaussian smearing of 0.2 eV was used.

4.3 G_0W_0 calculations on 2D h-BN

We saw in the previous section that we have to do calculations beyond DFT to have a more reliable description of the electronic band-structure of the 2D h-BN. In this section we use the BerkeleyGW [30] package code to do G_0W_0 calculations by using the previous DFT calculations as starting point. We use the Generalized-Plasmon-Pole (GPP) proposed by Hybertson e Louie [28]. In the chapter 3 we talked about the important factors about the G_0W_0 calculations which are done here.

At DFT level the convergence was achieved for a plane wave cut-off of 80 Ry (1088 eV) and a **k**-points mesh of $6 \times 6 \times 1$. We also saw that a vacuum size between the layers greater or equal than 15 bohr is sufficient to avoid interactions with the periodic images. Our first G_0W_0 calculation uses a grid of $6 \times 6 \times 1$ and a vacuum size of 50 bohr. Figures 4.5 and 4.6 show the convergence of the quasi-particle direct (K-K) and indirect gap (K-Γ) using the G_0W_0 calculations with the GPP.

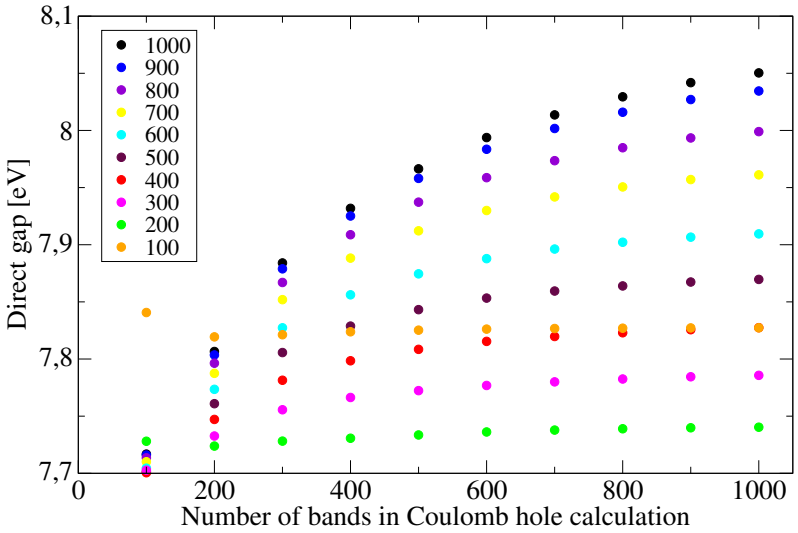

Figure 4.5: Quasi-particle direct gap vs number of bands in the Coulomb hole calculation for a G_0W_0 calculation that used a grid of $6 \times 6 \times 1$. The legend on box represents the number of bands used to construct the plane-wave matrix elements for the dielectric function. We used a criterion for convergence within approximately 0.02 eV.

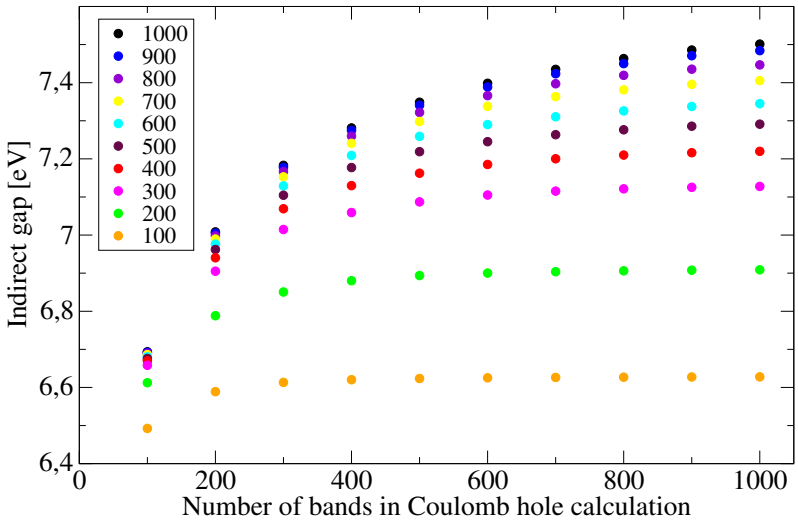

Figure 4.6: Quasi-particle indirect gap vs number of empty bands in the Coulomb hole calculation for a G_0W_0 calculation that used a grid of $6 \times 6 \times 1$. The legend on the left represents the number of bands used to construct the plane-wave matrix elements for the dielectric function. We used a criterion for convergence within approximately 0.02 eV.

In the graphic of the figure 4.5 and 4.6 the gap value is converged for 1000 bands in the Coulomb hole calculation (see equation B.15) and 1000 bands for the construction of the plane-wave matrix elements (see equation B.2) which correspondsto a dielectric cut-off of 15.95 Ry (217 eV). The direct gap is 8.05 eV and the indirect gap is 7.50 eV. This means that the band gap is indirect and not direct as predicted by our DFT calculations.

Besides, the band gap value is now 7.50 eV, which is a huge difference compared to the 4.43 eV from DFT. One fundamental point that should be noticed is the independent convergence that we can see in the two graphics. If we choose to fix the construction of the plane-wave matrix given by equation B.2, which are the elements needed to compute the static dielectric matrix given by equation B.8, with 100 bands that corresponds to a dielectric cut-off energy of 2.9 Ry, we can see that the number of bands needed to do the summation of the Coulomb hole calculation of equation B.14 is just 400 considering our criterion of convergence which is 0.02 eV.

Now if we increase the dielectric cut-off by including 1000 bands in the construction of the plane-wave matrix elements, which corresponds to dielectric cut-off energy of 15.95 Ry, we see that we need 1000 bands in the Coulomb hole calculation to achieve convergence.

It is clear then that we cannot fix one parameter and test the convergence of the other parameter independently. This happens because a low cut-

off energy for the dielectric matrix will prevent the contribution from high-energy conduction bands to the Coulomb-hole self-energy [43]. That is the reason why we have a false convergence behaviour for lower cut-off energies for the dielectric matrix. Figure 4.7 shows the quasi-particle electronic band-structure with the converged parameters of the graphics of figure 4.5 and 4.6 compared to the one obtained by DFT.

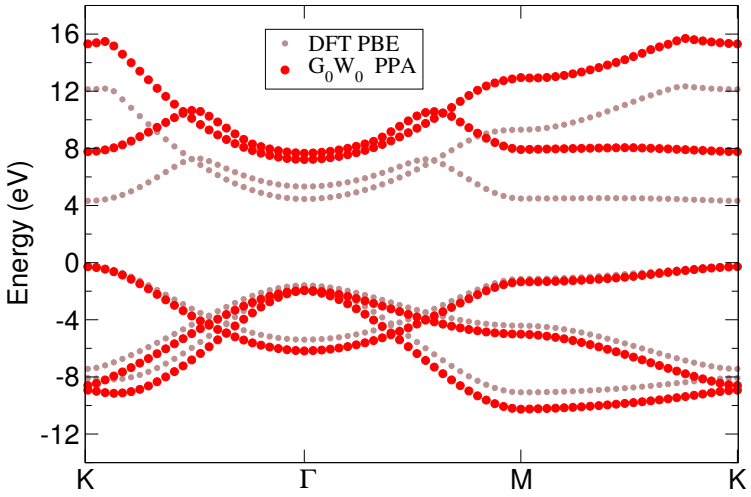

Figure 4.7: Quasi-particle band-structure (red) and DFT band-structure (brown).

Here we could conclude our *GW* work and say that the corrected band gap energy is 7.50 eV and it results from an indirect transition. But *GW* calculations also depends on the **k**-points as it is clear from appendix B. Figures 4.8 and 4.9 show the study of the convergence of the quasi-particle direct and indirect band gap with the same parameters of the previously study but now with a grid of $12 \times 12 \times 1$.

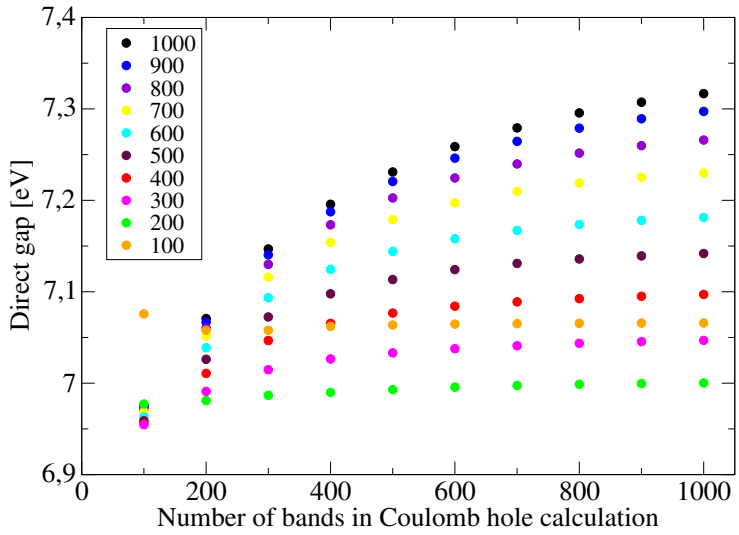

Figure 4.8: Quasi-particle direct gap vs number of bands in the Coulomb hole calculation for a G_0W_0 calculation that used a grid of $12 \times 12 \times 1$. The The legend on box represents the number of bands used to construct the plane-wave matrix elements for the dielectric function. We used a criterion for convergence within approximately 0.02 eV.

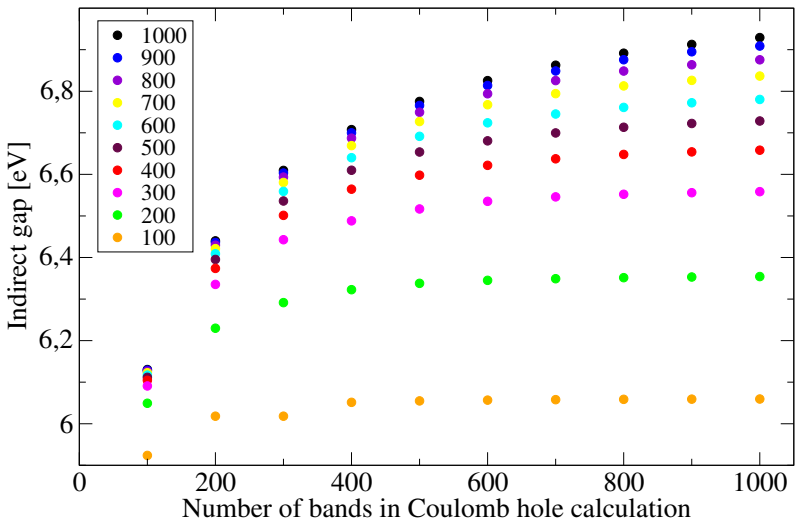

Figure 4.9: Quasi-particle indirect gap vs number of bands in the Coulomb hole calculation for a G_0W_0 calculation that used a grid of $12 \times 12 \times 1$. The The legend on box represents the number of bands used to construct the plane-wave matrix elements for the dielectric function. We used a criterion for convergence within approximately 0.02 eV.

From figure 4.8 and 4.9 we can see that the convergence is achieved for for 1000 bands in the Coulomb hole calculation and 1000 bands for the construction of the plane-wave matrix elements. The direct gap is 7.32 eV and the indirect gap is 6.93 eV. When compared to the graphics with a grid of $6 \times 6 \times 1$ we see that with a grid of $12 \times 12 \times 1$ the converged band gap is now lower as can be seen in figure 4.10. This shows that despite convergence

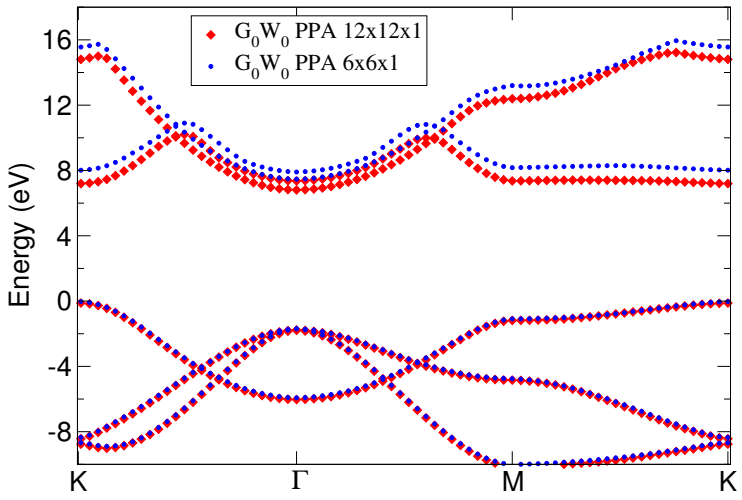

Figure 4.10: Quasi-particle band-structure of 2D h-BN. The blue graphic used a grid of $6 \times 6 \times 1$ to compute the G_0W_0 calculations whereas the blue graphic used a grid of $12 \times 12 \times 1$.

at DFT happens with a grid of $6 \times 6 \times 1$ it does not mean that the same is going to happen at G_0W_0 level. The reason for this can be explained by the fact that when we have a finer grid, we have more **k**-points contributing for the screening. It is known that the screening is higher for **k**-points near the Γ point which are captured by denser grids. The dielectric function for 2D materials varies a lot with **k**-points in the region near the Γ point and for higher points is is almost constant [44]. That is why it is important to have finer grids in order to capture the contribution of this small points near the Γ point.

It is also important to study the convergence of the quasi-particle energies with the size of the vacuum size between the layers. When increasing the the vacuum size, the number of **G**-vectors increases because it scales with the unit cell volume. This means that we have to do the previous studies all over again for the different vacuum sizes. The table 4.3 shows our G_0W_0 obtained gap for all different vacuum sizes and different grids.

We only made detailed studies for a vacuum size of 50 bohr with a grid of $6 \times 6 \times 1$ and a grid of $12 \times 12 \times 1$ which were shown in figures 4.5-4.9. For

k-points sampling	Vacuum space [bohr]			
	30	40	50	70
$6 \times 6 \times 1$	6.97	7.25	7.50	8.12
$8 \times 8 \times 1$	6.89	7.05	7.16	7.53
$12 \times 12 \times 1$	6.85	6.90	6.93	-
$14 \times 14 \times 1$	6.87	6.91	6.92	-

Table 4.3: G_0W_0 calculated indirect gap for 2D h-BN for four vacuum sizes.

the other studies with different vacuum sizes the procedure was to choose a high value for the number of bands in the construction of the plane-wave matrix elements and for each value we used two high values for the bands at Coulomb hole calculation and tested if the difference of the obtained gap is within 0.02 eV.

For example: we choose the value 1000 and 900 for the number of bands in the construction of the plane-wave matrix elements and we choose two high values for the Coulomb hole calculation, like 1000 and 900, and tested the convergence in these 4 calculations.

We can observe from table 4.3 that for different vacuum sizes we have different convergences. For a vacuum size of 70 bohr we could not find the converged value because calculations started to be very computational expensive for grids greater than $8 \times 8 \times 1$. We note that for different vacuum sizes we had different converged parameters. For a vacuum size of 30 bohr the indirect gap was converged with a dielectric cut-off of 21.10 Ry and for vacuum size of 40 bohr the indirect gap was converged with a dielectric cut-off of 17.60 Ry. This happens because the energy of a certain empty state is not the same for different vacuum sizes.

For a vacuum of 30 bohr we have a convergence at $8 \times 8 \times 1$. Increasing the grid will not alter significantly the value of the band gap as can be seen in table. For a vacuum space of 40 and 50 bohr we have a convergence at $12 \times 12 \times 1$. Looking at the data with 70 bohr we could anticipate that the convergence would be achieved for grids greater than $12 \times 12 \times 1$. This shows that when we increase the vacuum size a finer grid is necessary to obtain the true contribution of the screening. We think that this is due to a change of the behaviour of the dielectric function with the increase of the vacuum size but further investigation is need in order to have a clear understanding of this.

Nevertheless, it is clear that even when the convergence is found, the band gap value increases with the vacuum size. This can be explained by the non-local screening effects of the GW approximation which makes the gap

Reference	Type of calculation	L [bohr]	Band gap [eV]
This Work	G_0W_0	50	6.92 K-Γ
[31]	G_0W_0	Extrapolation $L \to \infty$	7.40 K-Γ
[40]	GW_0	28.34	6.86 K-Γ
[46]	G_0W_0	$14.0 < \mathrm{L} < 26.0$	6.00 K-Γ

Table 4.4: Summarized results for different works that use GW calculations for 2D h-BN. In our work we present the results with a vacuum distance of 50 bohr. In the first row of table L stands for the vacuum size between the layers while in reference [31] an extrapolation to infinity was done and for a reference [46] a vacuum size greater than 14 but smaller than 26.0 bohr was used. The GW_0 calculation is an update of the G_0W_0 calculation where only G is updated by converging the quasi-particle energies.

converges with $1/L$, where L is the vacuum size. This non-local screening effects are more weak with the increasing of the vacuum size which makes the electrons more correlated and thereby increasing the value of the band gap. The detailed physics beyond this convergence with $1/L$ can be consulted in reference [45].

To get the true band gap, one can use the fact that band gaps converge as $1/L$ and do an extrapolation in the limit of infinite L. Unfortunately, more calculations with different vacuum sizes, are needed in order to do such extrapolations. We just have results for three vacuum sizes, which is not enough. Nonetheless we can see that the band gap will not be so far from 6.9 eV since the difference between the vacuum distance of 40 and 50 bohr is just 0.01 eV.

In table 4.4, we have summarized the results of some works on the quasi-particle band gap of 2D h-BN. We can see that work [40] has computed a band gap of 6.86 eV which is in good agreement with our work. The others present computed band gaps that are far from our calculated value. Analysing reference [31] we could not find information about the G_0W_0 calculations parameters, but we can see that they used a grid for sampling the Brillouin zone that is not greater than $6 \times 6 \times 3$. We show in our work that such grid is not enough to get a converged value for the band gap. From our table 4.3 we can see that a $6 \times 6 \times 1$ grid would result in a too high value for the band gap.

In reference [46] we can find many issues that could lead to an underestimation of the band gap. First the BN bond length is set to the experimental distance of 2.74 bohr. This value cannot be the optimized one and that changes the band-structure of this material. Also, the vacuum distance is

smaller than 26 bohr and only 40 bands per atom were used. From our work it is clear that a distance greater than 40 bohr and at least 500 bands per atom are needed for full convergence. They also use a convergence criterion of 0.1 eV while we used a much stricter one of 0.02 eV.

Nevertheless, there are some common results between our work and the other works. The band gap is indirect (K - Γ) and it is larger than 6 eV, which is completely different from the results of DFT. We also confirm that it is important to use the *GW* approximation to predict the electronic band-structures.

4.4 BSE calculations on 2D h-BN

After the DFT and G_0W_0 calculations, we proceed to the optical calculations with the Bethe-Salpeter equation (BSE).
We start choosing a fine grid of $24\times24\times1$, which corresponds to 576 **k**-points. We choose to include 2 valence and 4 conduction bands on the calculation of the kernel and 2 valence and 2 conduction bands for the interpolation. The cut-off used (21.1 Ry) is the same that was used in the dielectric cut-off for the G_0W_0 calculation with a vacuum size of 30 bohr (we are using the previous G_0W_0 calculation results done with that vacuum space). Figure 4.11 shows the calculated absorption spectrum.

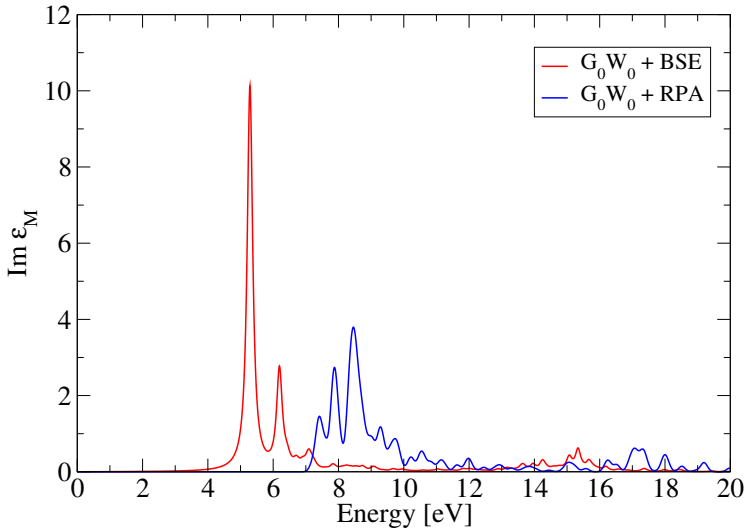

Figure 4.11: Absorption spectrum of 2D h-BN. The G_0W_0+RPA calculation does not include electron-hole interactions, while in G_0W_0+BSE excitonic effects are included. A gaussian broadening of 0.1 eV is used.

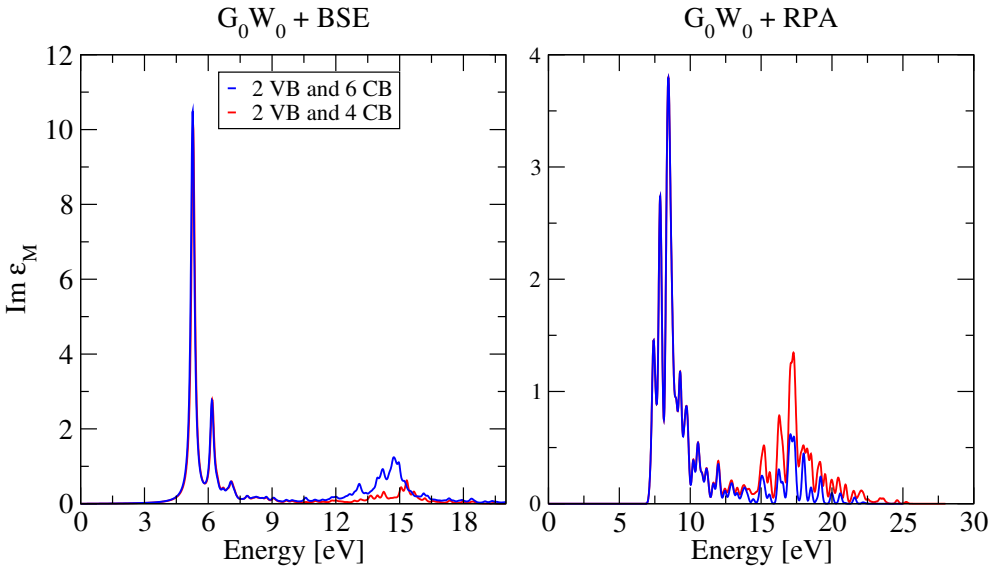

Figure 4.12: Left: G_0W_0+BSE absorption spectrum. Right: G_0W_0+RPA absorption spectrum. The red curves are the spectrum shown in figure 4.11. The blue curves have the same parameters of the red curves spectrum with the same number of valence bands (VB) but with more conduction bands (CB) for the kernel and interpolation.

It is necessary to study the convergence of the G_0W_0+RPA and G_0W_0+BSE spectrum. First we tested how changing the number of bands for the construction of the kernel and for the interpolation affects the spectrum. Increasing the number of valence bands in the kernel and in the interpolation does not influence the shape of the absorption spectrum but increasing the number of conduction bands has influence for energy values greater than 12 eV as can be seen in figure 4.12.

We are interested in the low energy zone where we measure the optical gap and binding energy. That is where we want the spectrum to be converged. The results with 2 valence and 4 conduction bands for the calculation of the kernel and 2 valence and 2 conduction bands for the interpolation are sufficient to achieve the convergence for that zone. We shall then use those values for the rest of the calculations.

The next absorption spectrum was calculated with an interpolation with a fine grid of $48 \times 48 \times 1$ which has 2304 **k**-points. The graphics are shown in figures 4.13 where we also included the graphic for 576 **k**-points for comparison.

When comparing the two graphics we can see that there are no significant differences between the shape of the spectrum. The only difference is that

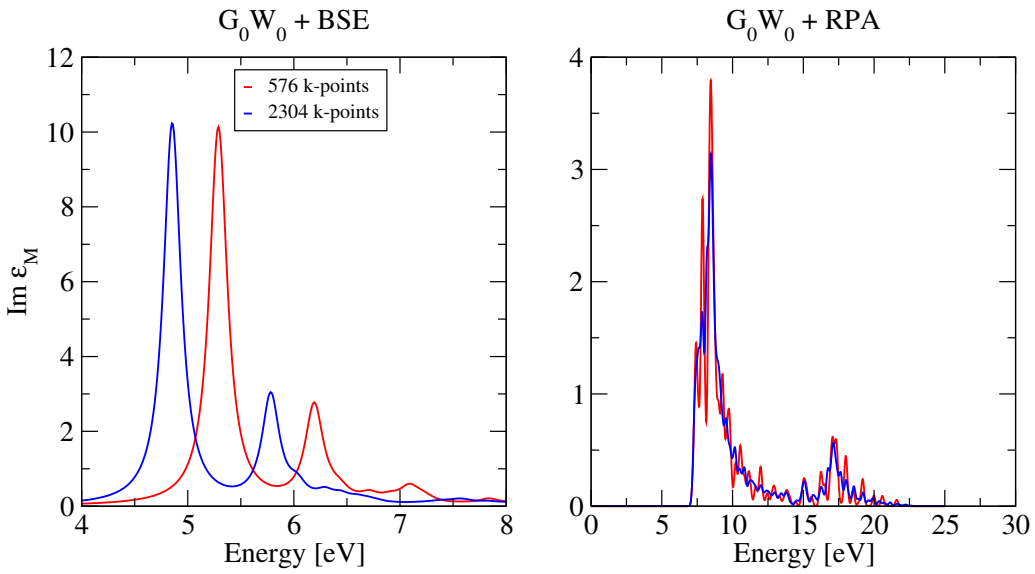

Figure 4.13: Left: absorption spectrum of 2D h-BN with the G_0W_0+BSE with an interpolation for a fine grid of 576 **k**-points (red) and 2304 **k**-points (green). Right: absorption spectrum of 2D h-BN with the G_0W_0+RPA with an interpolation for a fine grid of 576 **k**-points (red) and 2304 **k**-points (blue).

the "wiggle" is lower in the finer grid. That is not surprising because the elimination of the "wiggle" happens when we increase the density of **k**-points.

The other difference that we can observe is the red-shift of the spectrum for the G_0W_0+BSE with more **k**-points. The first peak and second peak are positioned at an energy of 5.3 eV and 6.2 eV for the grid 576 **k**-points, while for the grid 2304 **k**-points we have 4.9 eV and 5.8 eV. Because this red-shift is very significant it is important to study the convergence of these two peaks with the number of **k**-points used in the interpolation. So we do the previous calculations but changing the finer grid in which the kernel is interpolated and check where the convergence of the position of the two peaks is achieved. This study is shown in figure 4.14. We choose a convergence within a criterion of approximately 0.1 eV.

The first and second peak are converged for a fine grid with 25600 **k**-points and the correspondent graphic is shown in figure 4.15. When we look at the converged spectrum of figure 4.15 and compare with the left spectra in figure 4.13, we see that there are not many differences. The only difference is the red-shift in the G_0W_0+BSE spectrum and the elimination of the "wiggle" which is very visible in the G_0W_0+RPA spectrum which is much more smooth now.

With the convergence achieved we can conclude that the optical gap is

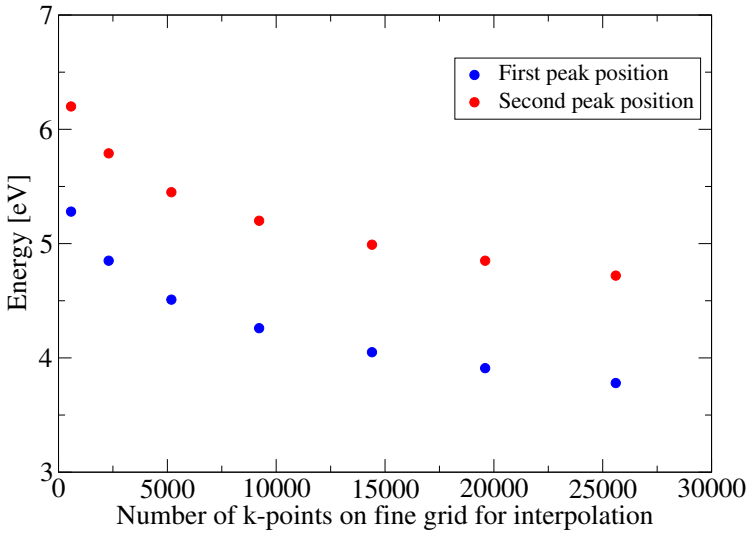

Figure 4.14: Convergence of the first and second peak position of the G_0W_0+BSE absorption spectrum. We used a criterion for the convergence approximately 0.1 eV. The first peak and second peak are converged for a fine grid with 25600 **k**-points with an energy of 3.8 eV and 4.7 eV respectively.

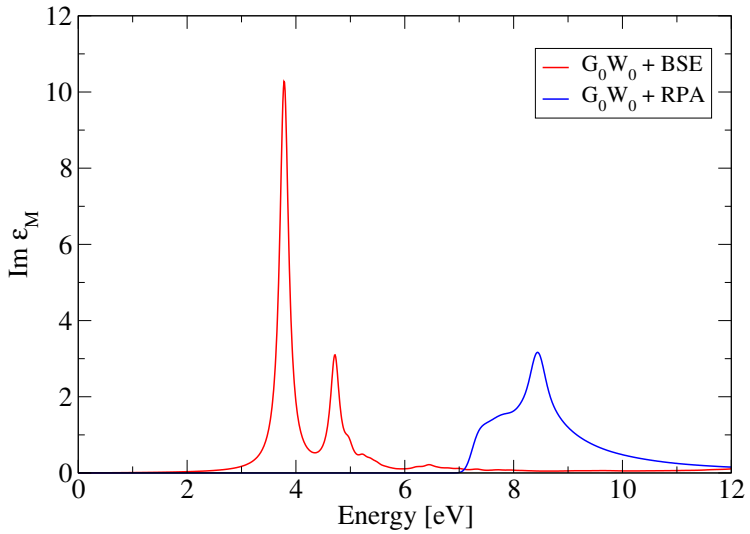

Figure 4.15: Absorption spectrum with the same parameters of figure 4.11 but with a finer grid with 25600 **k**-points.

3.8 eV. Knowing that the band gap calculated with the G_0W_0 (for a vacuum size of 30 bohr) was 6.9 eV, we obtain a binding energy of 3.1 eV for the first exciton. But it is important, as mentioned in the previous section, that we must recalculate everything for different vacuum sizes. We use the previous

G_0W_0 results with the vacuum sizes of 40 bohr and 50 bohr. The absorption spectra that were obtained with these vacuum sizes have the same shape of the one obtained with a vacuum size of 30 bohr, but the position of the peaks are different. Figure 4.16 shows the convergence of the position of the peaks with the number of **k**-points of the fine grid for the interpolation. Figure 4.17 shows the converged absorption spectra for a vacuum size of 40 and 50 bohr.

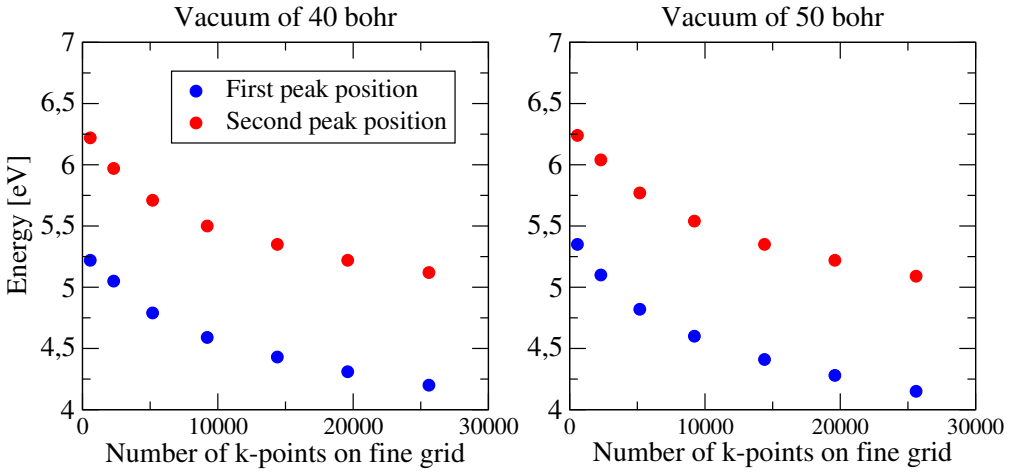

Figure 4.16: Convergence of the first and second peak positions of the G_0W_0+BSE absorption spectrum for a vacuum size of 40 bohr and 50 bohr. The first peak and second peak are converged for a fine grid with 25600 **k**-points with an energy of 4.2 eV and 5.1 eV respectively for a vacuum size of 40 and 50 bohr.

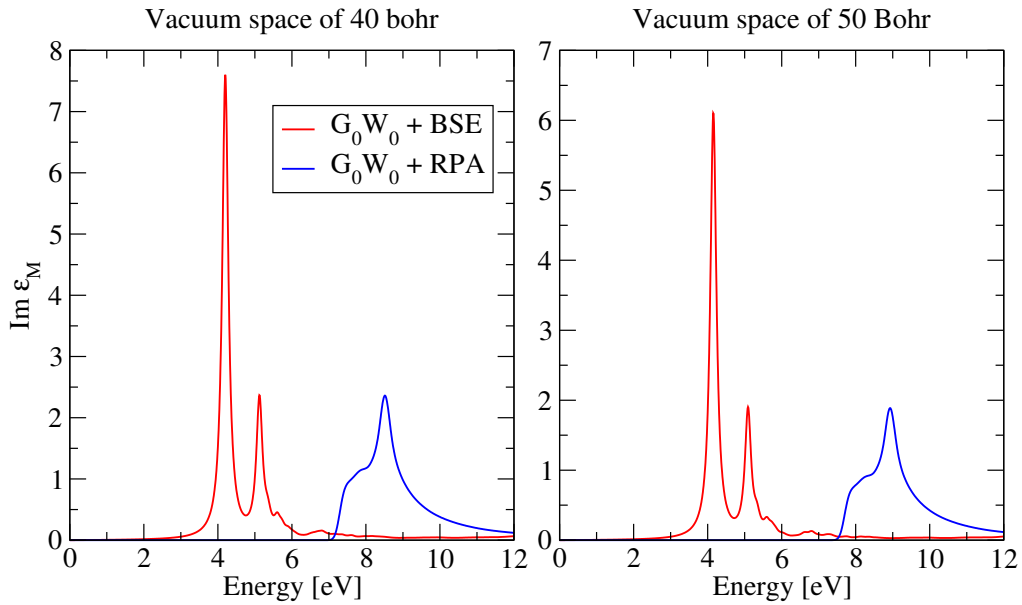

Figure 4.17: Absorption spectrum with the same parameters of 4.15 but for a vacuum size of 40 bohr (left) and 50 bohr (right).

For a vacuum size of 40 and 50 bohr, we obtain an optical gap of 4.2 eV and knowing that the G_0W_0 band gap was 6.9 eV, the binding energy is 2.7 eV. These two values are very different from the one obtained with a vacuum size of 30 bohr. Again, this shows the importance of doing a convergence study of the vacuum size between the periodic images.

More calculations with different vacuum sizes are needed in order to achieve more accuracy in the optical gap and binding energy of the first exciton. Nevertheless, with our calculations we can see that the binding energy is tending to values in the range of 2.8 to 3.0 eV, since the difference of the excitonic binding energy for vacuum distances of 40 and 50 bohr is less than 0.1 eV . This excitonic binding energy is relatively high since other works give around 0.7 eV [47] for the bulk h-BN excitonic binding energy. This happens because the screening is less for systems with low dimensionality and the overlap between the electron and hole is higher, which enhance the Coulomb interaction between them.

Only a few works considering a theory with excitonic effects have been done. Yet, those effects are very important as we can see in figures 4.4 and 4.17. Using only the DFT+RPA or the G_0W_0+RPA to calculate the absorption spectrum is not enough.

If the G_0W_0+RPA spectrum were totally converged for high energies, we could see that G_0W_0+RPA is the DFT spectrum but blue-shifted.

This is because DFT+RPA spectrum is just a RPA full frequency calculation without the quasi-particle energies corrected. When the excitonic interactions are considered in the G_0W_0+BSE calculation, two strong peaks appear for energies lower than the band gap energy. The first excitonic peak, which is the optical gap, is the dominant peak of the absorption spectrum.

Reference	Type of calculation	1º peak [eV]	2º peak [eV]	EBE [eV]
This Work	G_0W_0+BSE	4.2	5.1	2.7
[48]	GLLBSC+BSE	6.1	7.1	1.9
[49]	GW+BSE	5.6	6.4	1.4
[47]	GW_0+BSE	-	-	2.1

Table 4.5: Summarized results for different works that use the BSE for 2D h-BN. In our work we use the results with a vacuum distance of 50 bohr. The work [48] do not use GW calculations but the DFT functional GLLBSC [50]. In the work [49] we could not know that the GW is the self-consistent step after G_0W_0. In the work [47] the GW_0 is the result of updating the G_0W_0 quasi-particles until self-consistency is achieved.

In table 4.5 we summarize some of the results of the works that used the BSE calculation to calculate the absorption spectrum of 2D h-BN. We note that for all works in table 4.5 the absorption spectra presented the same shape, where we have two peaks with more intensity for energies lower than the band gap energy. The differences are the position of the excitonic peaks and the band gap energy. This of course is going to change the excitonic binding energy. This differences are not unexpected because we saw that the same happens for the band gap energy in the previous G_0W_0 calculations.

It is not easy to tell the origin of this differences because the works [47,49] do not have information about the GW and BSE calculations. In the work [48] the BSE is calculated with Brillouin zone sampled on a non Γ-centered 32×32 grid. This grid is very small when compared to the converged grid of our work. They also used a vacuum size of 38 bohr with a truncation technique to avoid the periodic interactions. Even with truncation techniques it is necessary to study the convergence with respect to vacuum size because there is always an influence in the wave-functions and energies for highly unbounded states [44].

As we mentioned in the chapter 1, few experimental works have been done for 2D h-BN. In reference [51] the optical gap was measured for h-BN films (two to five layers) and its value is 5.56 eV but the excitonic binding energies are not measured. In reference [52] an optical gap of 5.955 eV is measured and an excitonic binding energy of about 130 meV is obtained. It mentions that the excitons in h-BN are of the Wannier type, in contrast to the theoretical framework.

Chapter 5

Phosphorene

5.1 Introduction

Single layer black phosphorus, or phosphorene, is a very recent material [53] that has been studied in many areas due to its promising properties. It is a semiconductor material and its band gap is approximately 2.0 eV [54] which is much higher that the bulk band gap which is 0.3 eV [55]. Studies have reported a high mobility for this material [56] which makes this material very good for the construction of field-effect transistors. The reported on/off ratios are up to 10^5 [57, 58]. Also it can be used for gas sensor [59] and solar-cell applications [60]. Another particular property is the strong in-plane anisotropy of transport and optical properties. The reason for the anisotropy is its structure that is shown in figure 5.1 where we can see that phosphorene is structured by puckered lattice due to sp3 hybridization. This structure allows band gap engineering by applying strain in-plane or out of plane [61].

Because this material is bidimensional, the excitonic effects can not be neglected and must be taken into account if we want to study its optical properties like absorption spectra. We study the electronic properties by using the *GW* approximation [11, 12] and the optical properties by using Bethe-Salpeter equation [14,15] (BSE). This is very important because as we will see DFT does not provide a good description of the electronic band-structures of phosphorene and a many-body formalism that takes into account electron-electron interactions is necessary. Besides, we cannot neglect the excitonic effects and the BSE is also very important and should be considered.

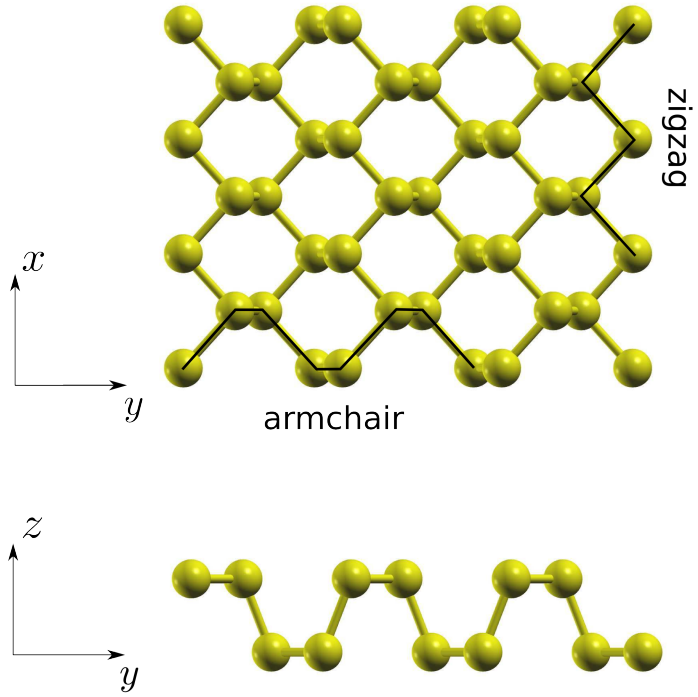

Figure 5.1: Structure of phosphorene. The yellow balls corresponds to P atom. Top: top view in xy plane. Bottom: side view in zy plane. In the xy plane we can see that phosphorene structure is arranged in different ways with a zigzag structure along the x axis and an armchair structure along the y axis.

5.2 DFT calculations

First principle calculations were done by using the QUANTUM ESPRESSO package [36] which is based on the DFT formalism. A plane-wave basis is used. The pseudopotential used for phosphorus atom is non-relativistic. The exchange-correlation functional is approximated by PBE [37] generalised gradient approximation (GGA). A plane-wave energy cut-off of 70 Ry (952 eV) was used. The **k**-points mesh was sampled by a Monkhorst-Pack [38] method with convergence at 9× 9× 1. Both the plane-wave energy cut-off and the **k**-points mesh convergence are shown in figure A.5 and A.6 in the appendix A.

We have used a periodic cell with the vectors shown in table 4.1 which are shown in figure 5.2.

Real space	Reciprocal space
$\vec{a_1} = a\vec{e}_x$	$\vec{b}_1 = \frac{2\pi}{a}\vec{k}_x$
$\vec{a_2} = b\vec{e}_y$	$\vec{b}_2 = \frac{2\pi}{b}\vec{k}_y$

Table 5.1: Lattice vectors in real space and reciprocal space. The parameter a and b are the lattice constants.

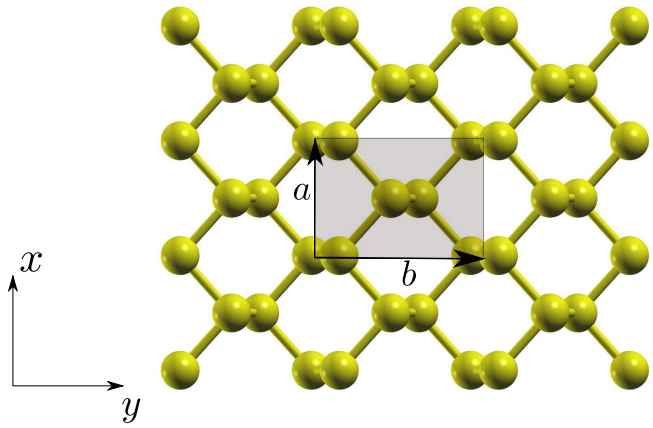

Figure 5.2: The shadow is the area of the unit cell used to construct phosphorene. The vectors $\vec{a}$ and $\vec{b}$ are given in table 5.1.

We relaxed the system to obtain the optimized structure and obtained the lattice parameters $a = 6.24$ bohr and $b = 8.67$ bohr. A vacuum size between

the layers of $c \geq 20$ bohr is enough to avoid interactions between the periodic images. This study is shown in figure A.7 of appendix A. In figure 5.3 the obtained band-structure along a chosen **k**-point path is shown.

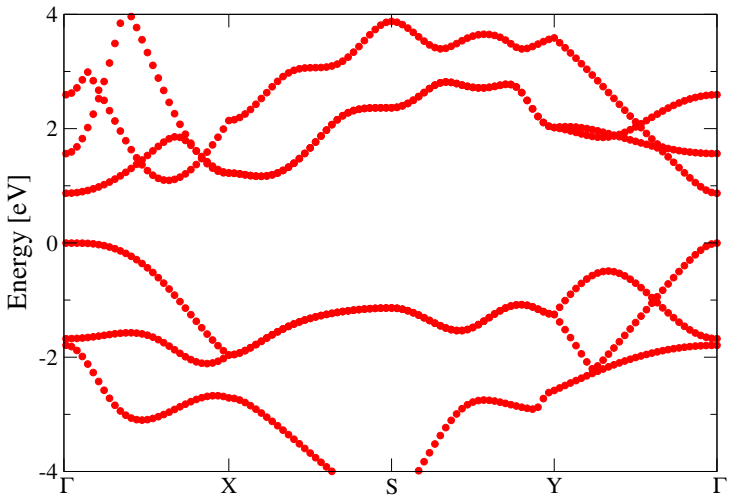

Figure 5.3: Electronic band-structure of 2D h-BN along the path Γ-X-S-Y-Γ. The exchange-correlation functional is approximated by PBE-GGA. The band gap is direct at Γ point with an energy of 0.87 eV.

We can see that we have a direct band gap at the Γ point and it has an energy of 0.87 eV.

In table 5.2 we have summarized some works that we found in the literature about DFT of phosphorene.

Reference	XC functional	a [bohr]	b [bohr]	Band gap [eV]
This Work	GGA	6.24	8.76	0.87
[62]	GGA	6.24	8.72	0.91
[56]	GGA	6.27	8.72	0.91
[63]	GGA			0.80
[62]	HSE	6.24	8.72	1.56
[56]	HSE	6.27	8.66	1.51

Table 5.2: DFT results from different works including ours. We include the exchange-correlation functional (XC), the lattice constants a and b, and the band gap which is at Γ. We could not obtain the lattice constant of work [63].

By looking at table 5.2, we see that our band gap and lattice parameters are in good agreement with the works that used the GGA functional. However, we can see that for the works that used the functional HSE, the band gap is much larger. The HSE [41] functional is often used to achieve a larger band gap than the ones obtained by LDA or GGA (which underestimate it in semiconductors).

DFT is not enough to describe the electronic properties and other better approximation is necessary. Unfortunately we could not find experimental data for the lattice parameters but we could find two works that estimate experimentally the band gap of phosphorene with a value of 2.05 eV [54] and 2.2 ± 0.1 [64]. These values are far from being in agreement with the results from our work and the other DFT works. So it is important to do calculations that take into account many-body effects like the *GW* approximation.

The absorption spectrum which is proportional to the imaginary part of the macroscopic dielectric function was calculated using the post processing code of QUANTUM ESPRESSO epsilon.x. The graphic is shown in figure 5.4 where we calculated the dielectric function for light polarized along the zigzag (x axis) and armchair (y axis) direction. This spectrum will be discussed with more detail in section 6.4.

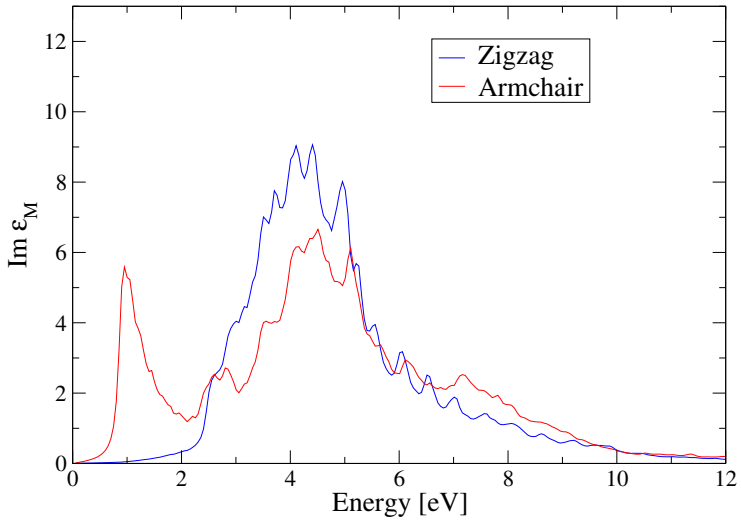

Figure 5.4: Imaginary part of the macroscopic dielectric function at DFT-GGA+RPA level of phosphorene. We just computed the dielectric function for light polarized along the x axis (blue colour) and y axis (red colour). Local field effects are not included.

5.3 G_0W_0 calculations on phosphorene

It is clear from the previous section that DFT is not reliable to predict the electronic band-structure of phosphorene. We use the GW approximation to study with more accuracy the electronic properties of this material. The BerkeleyGW package [30] is used where G_0W_0 is computed with DFT calculations as the starting point. The Generalised-Plasmon-Pole (GPP) model proposed by Hybertson e Louie [28] is used. In chapter 3 we talked about important factors about the G_0W_0 calculations which are useful for this section. It is important to remember that at DFT level the convergence was achieved for a plane wave cut-off of 70 Ry (952 eV) with a mesh of **k**-points of $9 \times 9 \times 1$ and a vacuum size between the layers greater or equal than 20 bohr is sufficient to avoid interactions with the periodic images.

Our first G_0W_0 calculations uses a grid of $9 \times 9 \times 1$ and a vacuum size of 40 bohr. Figure 5.5 shows the convergence of the quasi-particle band gap using the G_0W_0 calculations with the PPA.

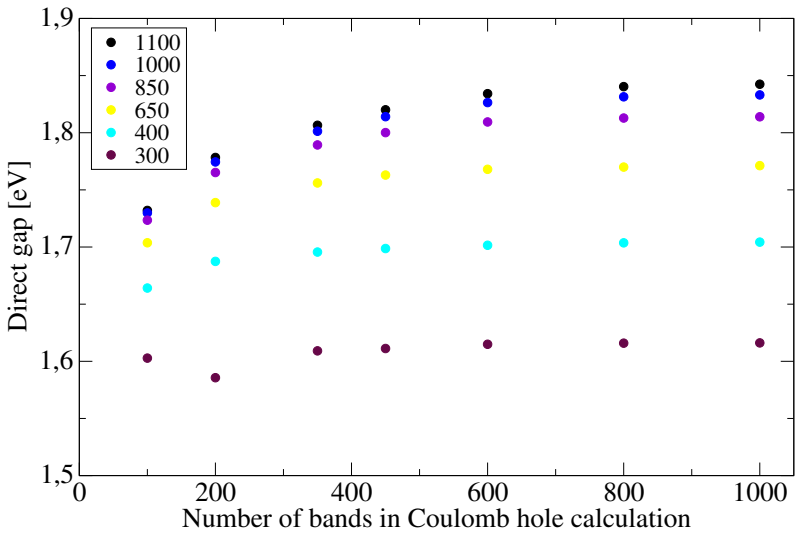

Figure 5.5: Quasi-particle direct gap vs number of bands in the Coulomb hole calculation for or a G_0W_0 calculation that used a grid of $9 \times 9 \times 1$. The legend on the box represents the number of bands used to construct the plane-wave matrix elements for the dielectric function. We used a criterion for convergence within approximately 0.02 eV.

The band gap is converged for 1000 bands for the construction of the plane-wave matrix elements which corresponds to a dielectric cut-off of 9.73 Ry (see equation B.2) and for 1100 bands in the Coulomb hole calculation (see equation B.15). The quasi-particle band gap is 1.84 eV which is much higher than the DFT value (0.87 eV). It is important to note the behaviour of the convergence by looking at graphic 5.5. It is clear that for the data with 300 bands to construct the plane-wave matrix elements for the dielectric function, the band gap converges for 500 bands in the Coulomb hole calculation with

a value approximately 1.6 eV. But when we increase the number of bands to construct the plane-wave matrix elements for the dielectric function, we see that for achieving the convergence is necessary more than 500 bands in the Coulomb hole calculation. So the convergence parameters are dependent and we can not fix one and converge the other and then fix the converged one and study the convergence of the one that was fixed. That leads very often to a false converged value. The reason why this happens is because a low cut-off energy for the dielectric matrix (or for a lower number of bands to construct the plane-wave matrix elements for the dielectric function) prevents the contribution from high-energy conduction bands to the Coulomb-hole self-energy which are important to the screening effect [43]. Figure 5.6 shows the quasi-particle electronic band-structure that corresponds to the graphic of figure 5.5 compared to the obtained by DFT. We saw from DFT calculations

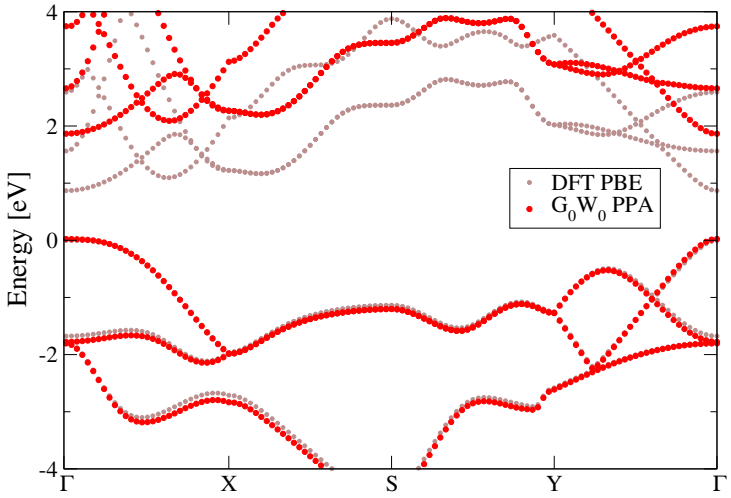

Figure 5.6: Quasi-particle band-structure (red) and DFT band-structure (brown).

that the converged grid is achieved for a mesh of $9 \times 9 \times 1$. Unfortunately this does not mean that for *GW* approximation the convergence happens at the same grid. So we have to do the same study but now with a grid of $11 \times 11 \times 1$ to see if and how the quasi-particle energies change. The figure 5.7 shows the study of the convergence of the quasi-particle band gap direct and indirect band gaps with the same parameters of the previously study but now with a grid of $11 \times 11 \times 1$.

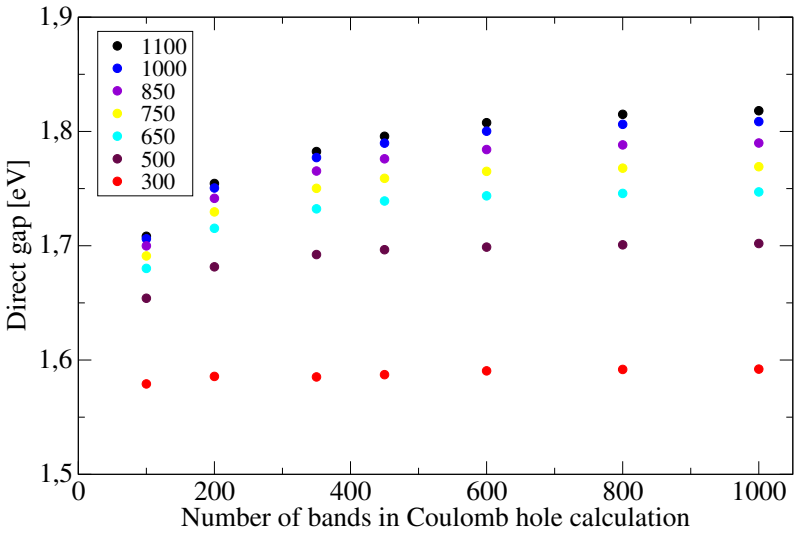

Figure 5.7: Quasi-particle direct gap vs number of bands in the Coulomb hole calculation for a G_0W_0 calculation that used a grid of $11 \times 11 \times 1$. The legend on box represents the number of bands used to construct the plane-wave matrix elements for the dielectric function. We used a criterion for convergence within approximately 0.02 eV.

When compared to the graphics with a grid of $9 \times 9 \times 1$ we see that for the grid of $11 \times 11 \times 1$ the converged band gap is lower with a difference of 0.02 eV. This means that it is not necessary to do more calculations for different grids but to make sure we have done one more calculation for the grid $13 \times 13 \times 1$ where the result is shown in table 5.3.

The study of the convergence of the quasi-particle energies with the vacuum size between the layers is also important. The number of **G**-vectors, which are present in all GW equations, increase with the increase of the volume of the supercell. It is necessary then to repeat the previously studies for different vacuum sizes. The table 5.3 shows our G_0W_0 with GPP obtained gap for all different vacuum sizes.

k-points sampling	Vacuum space [bohr]			
	c=20	c=30	c=40	c=70
$9 \times 9 \times 1$	1.74	1.77	1.84	2.05
$11 \times 11 \times 1$	1.75	1.78	1.82	1.98
$13 \times 13 \times 1$	1.77	1.78	1.81	1.88

Table 5.3: G_0W_0 calculated indirect gap for 2D h-BN for four vacuum sizes.

Detailed studies were done for a vacuum size of 40 bohr with a grid of $9 \times 9 \times 1$ and $11 \times 11 \times 1$ which were shown in figures 5.5-5.7. For the other studies with different vacuum sizes we choose two high values for the number of bands in the construction of the plane-wave matrix elements and for each value we used two high values for the bands at Coulomb hole calculation and tested the convergence in those four calculations. We could not find the converged value for a vacuum size of 70 bohr because calculations started to be computationally expensive for grids greater than $13 \times 13 \times 1$.

We can see from table 5.3 that for different vacuum sizes, we have different converged values for the quasi-particle band gap. This can be explained by the non-local screening effects of the GW approximation which makes the gap converges with $1/L$, where L is the inter-layer distance or vacuum size. A possible explanation of what is happening here is that when we increase the vacuum size the screening is becoming more weaker, which increases the electron-electron correlation. The weaker the screening the larger the band gap becomes. The detailed physics beyond this convergence with $1/L$ can be consulted at [45]. These effects do not happen in DFT because the potentials are local. We could get the band gap for an infinite L, if we do an extrapolation in the limit of infinite L. For that, more calculations are data needed but we can easily see that the band gap is converging to a value that is in the range of 1.8 to 1.9 eV.

In table 5.4 we summarize the results from other works to compare with our work.

Reference	Type of calculation	L [bohr]	Band gap [eV]
This Work	G_0W_0	40.00	1.81
[61]	G_0W_0	28.34	2.31
[65]	GW_0	$\approx$ 28.34	1.85
[63]	G_0W_0	-	2.00
[54]	GW_0	34.00	1.94
[66]	G_0W_0	$\approx$ 37.79	1.60

Table 5.4: Summarized results for different works that use GW calculations for phosphorene. In our work we present the results with a vacuum distance of 40 bohr. In the first row of table L stands for the vacuum size between the layers. The calculation GW_0 is a calculation is an update of the G_0W_0 calculation where only G is updated by a converging the quasi-particle energies.

In table 5.4 we see that our results are in line with most of the other works, with a band gap ranging from 1.8 to 2.0 eV. The only work that is more deviated from our work is [61] where the band gap calculated is 2.31 eV. In that work, 326 bands and a vacuum size of 28.34 bohr were used for the G_0W_0 calculations. That number of bands is very small when compared with the number of bands used in our work. A vacuum space greater than 30 bohr is also important to achieve convergence. The works [63, 65, 66] have used only a few empty bands, ranging from 80 to 360. The work [54] uses parameters close to the ones used in our work. They use a grid $9 \times 12 \times 1$ and an energy cutoff for the response function was 150 eV. The only difference is that they do a GW_0 calculation and that can explain the difference with our results.

The experimental values for the fundamental band gap (not optical) that we have found are 2.05 eV [54] and 2.2 ± 0.1 [64]. In contrast to DFT values, the G_0W_0 values are much closer to these experimental ones, but there are still some deviations.

We have just found two experimental works. More experimental data on the band gap of phosphorene would be very convenient. We know that there are factors like doping, defects and substrate interactions that can influence the band gap of the material.

5.4 BSE calculations on phosphorene

In this section we perform BSE calculations where we use the previous results of the G_0W_0 calculation. The important factors about the BSE calculations that are done in this section are discussed in the chapter 3 section 3.3.

First we choose a fine grid of $24 \times 24 \times 1$ that corresponds to 576 **k**-points. We included 2 conduction and 2 valence bands for the construction of the kernel matrix and for the interpolation. The obtained absorption spectrum is shown in figure 5.8.

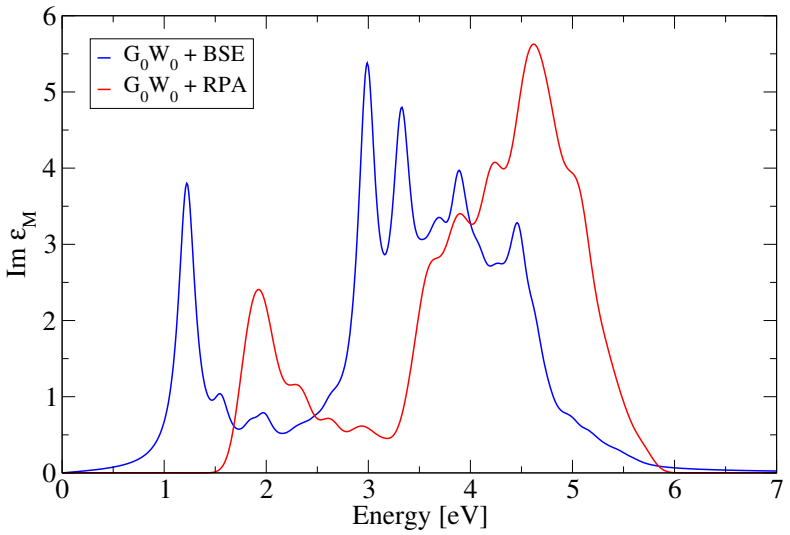

Figure 5.8: Absorption spectrum of phosphorene. The G_0W_0+RPA calculation does not include electron-hole interactions, while in G_0W_0+BSE excitonic effects are included. A gaussian broadening of 0.1 eV is used.

Now we increase the number of valence and conduction bands for 4 in the construction of the kernel matrix and for the interpolation and we compare to the previously result as can be seen in figure 5.9.

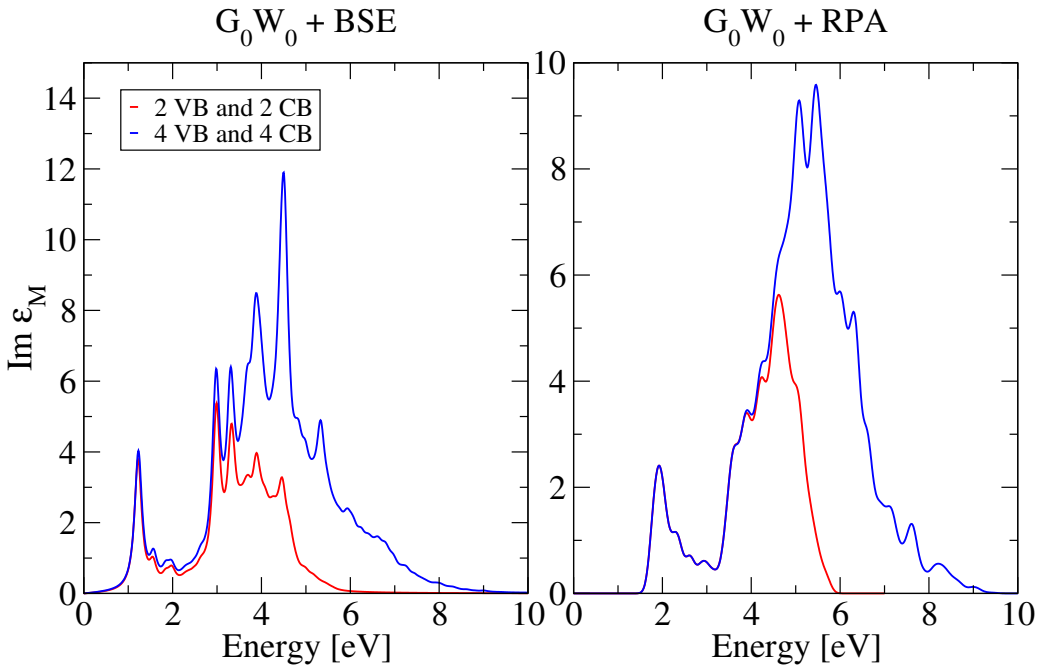

Figure 5.9: The red curves are the same from figure 5.8. The blue curves are the same spectrum but with the inclusion of 4 valence and conduction bands for the construction of the kernel matrix and for the interpolation.

The difference is very significant as we can see from the two graphics of figure 5.9 which means that we have to increase the number of bands again to verify if the absorption spectrum changes.

In figures 5.10 we increase the number of conduction bands and valence bands to 6 and compare with the previous calculation.

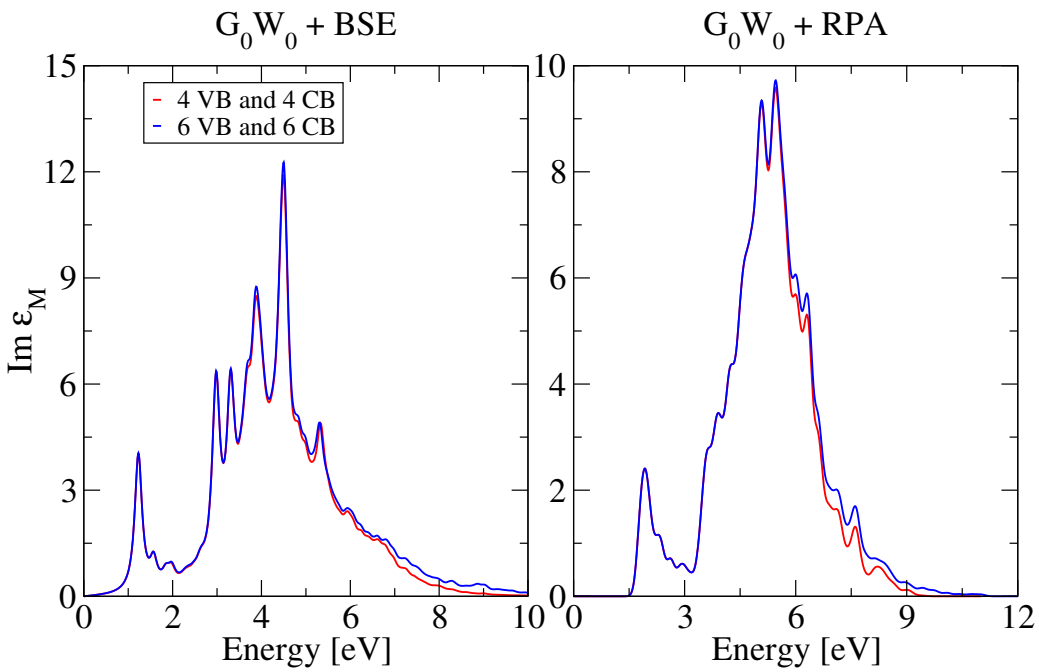

Figure 5.10: The red curves are from the same spectrum of figure 5.9 with blue curves. The blue curves represent the same spectrum but with inclusion of 4 valence and conduction bands for the construction of the kernel matrix and for the interpolation.

We can conclude that it is necessary to include more conduction and valence bands if we want a full converged absorption spectrum. For that we would need to compute the quasi-particle energies for energies up to 10 eV and construct the kernel by including bands that corresponds to that energy. But we are interested only in the absorption spectrum for the range of energies between 0 to 3 eV, where we can measure the optical gap. For that range of energy the absorption spectrum is practically converged for 4 valence and conduction bands, so we choose that number for the next calculations always considering that for high energies the absorption spectrum is not fully converged.

In the next calculation we use a fine grid of $48 \times 48 \times 1$ which has 2304 **k**-points. The comparison with the graphic with 576 **k**-points is shown in figure 5.11. We can see that there is less "wiggle" for the graphic with a

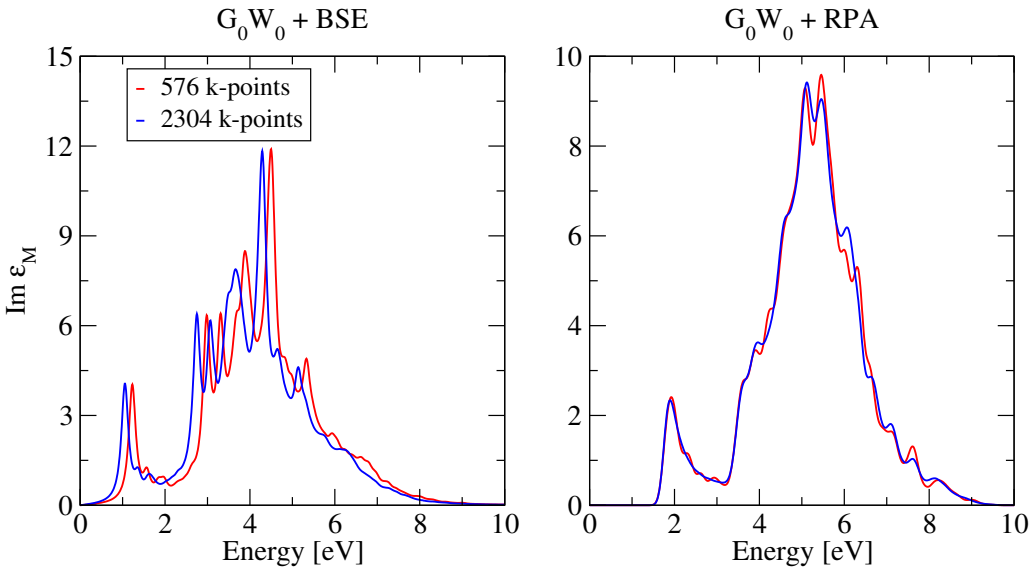

Figure 5.11: Absorption spectra of phosphorene for different fine grids used on the interpolation. For red curves we have a fine grid of 576 **k**-points and for blue curves we have a fine grid of 2304 **k**-points. We used 4 valence and 4 conduction bands for the construction of the kernel matrix and for the interpolation. A gaussian broadening of 0.1 eV is used. For energies greater than 3 eV the spectrum is not converged as discussed above in the text.

denser a grid. This is because we have a better interpolation when including more **k**-points. In the graphic without electron-hole interaction the peaks are almost in the same position whereas in the BSE graphic there is a red-shift, because the peaks are positioned in lower energies for the denser grid. The first peak is "red-shifted" about 0.17 eV which is a significant difference. It

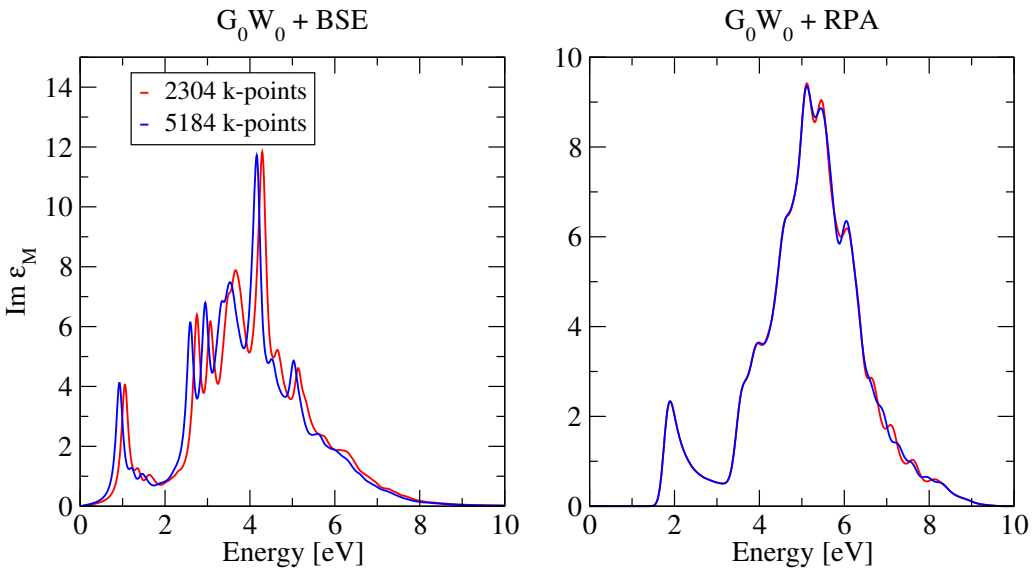

Figure 5.12: Absorption spectra of phosphorene for different fine grids used on the interpolation. For red curves we have a fine grid of 2304 **k**-points and for blue curves we have a fine grid of 5184 **k**-points. We used 4 valence and 4 conduction bands for the construction of the kernel matrix and for the interpolation. A gaussian broadening of 0.1 eV is used. For energies greater than 3 eV the spectrum is not converged as discussed above in the text.

is necessary to increase the number of **k**-points of the fine grid to converge the peak's position.

In the next calculation we use a fine grid of $72 \times 72 \times 1$ which contains 5184 **k**-points. In figure 5.12 we can see the comparison with the results for $48 \times 48 \times 1$. Once again we can observe a reduction of the wiggle for the spectrum obtained with more **k**-points. The first peak is red-shifted about 0.13 eV. Our convergence criterion is 0.1 eV so we do one more calculation with a finer grid to see if that criterion is achieved. In the next calculation we use a fine grid of $96 \times 96 \times 1$ which contains 9216 **k**-points. In figure 5.13 we can see the comparison with the results for $72 \times 72 \times 1$.

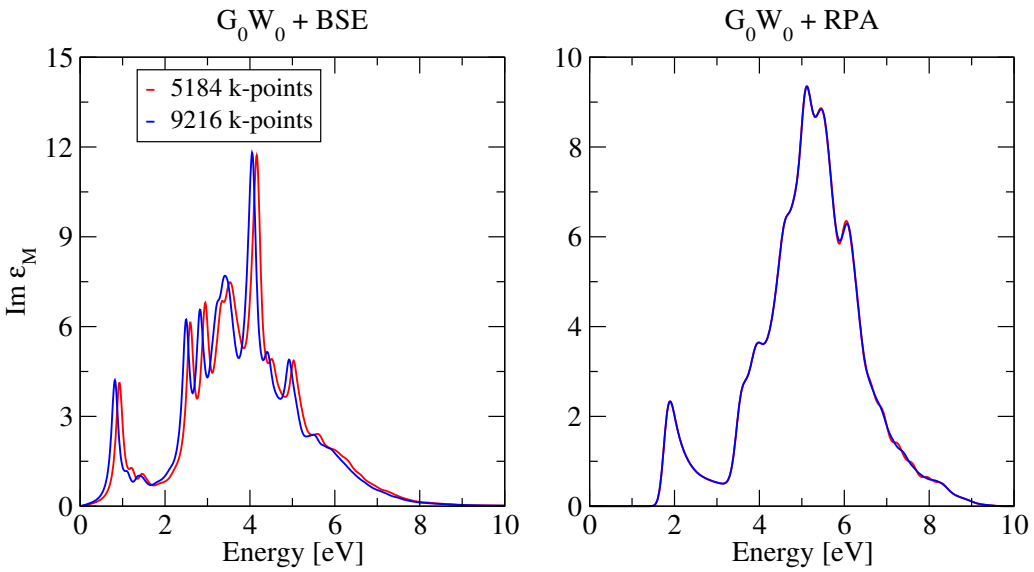

Figure 5.13: Absorption spectra of phosphorene for different fine grids used on the interpolation. For red curves we have a fine grid of 5184 **k**-points and for blue curves we have a fine grid of 9216 **k**-points. We used 4 valence and 4 conduction bands for the construction of the kernel matrix and for the interpolation. A gaussian broadening of 0.1 eV is used. For energies greater than 3 eV the spectrum is not converged as discusses above.

The first peak is red-shifted about 0.1 eV. This is our convergence criterion which means that the BSE spectrum is converged for a fine grid of $96 \times 96 \times 1$. The first peak is positioned at an energy of 0.8 eV. From the results for the G_0W_0 calculation we saw that he band gap value was 1.8 eV. This means that the binding energy of the first exciton is 1.0 eV. We have also done the same calculations but now with the previous G_0W_0 calculation but with a vacuum size of 40 bohr. The results were almost the same as the results with 30 bohr. The convergence was achieved for a grid of 9216 **k**-points. The only difference was the position of the first exciton which is 0.9 eV. The absorption spectrum is shown in figure 5.14.

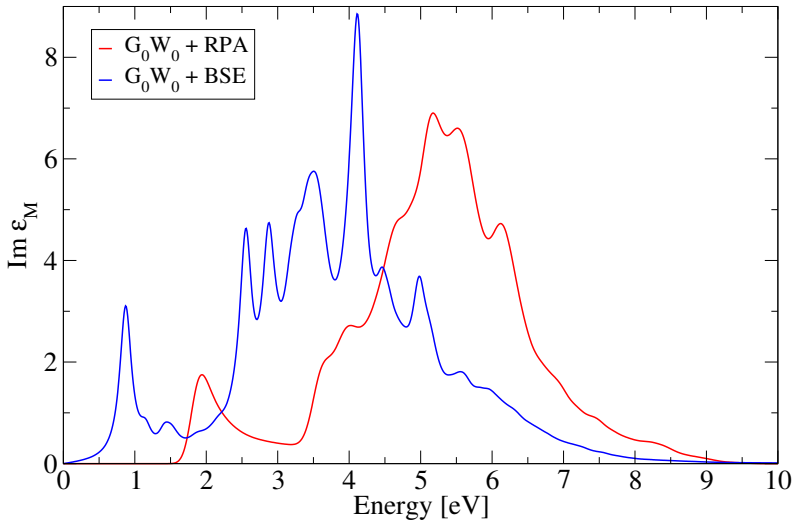

Figure 5.14: Absorption spectrum of phosphorene. The G_0W_0+RPA calculation does not include electron-hole interactions, while in G_0W_0+BSE excitonic effects are included. This calculation is computed in a coarse grid of $11 \times 11 \times 1$ **k**-points and then interpolated in a finer grid of $96 \times 96 \times 1$ **k**-points. We used 4 valence and 4 conduction bands for the construction of the kernel matrix and for the interpolation. A gaussian broadening of 0.1 eV is used.

Looking at figures with calculations at the DFT level (figure 5.4) and G_0W_0+RPA we can see that both do not present peaks for energies lower than the band gap. In the DFT calculation we have a band gap of 0.9 and the first peak which is due to the light polarization parallel to the armchair direction is positioned at the energy 1.0 eV. The G_0W_0+RPA absorption spectrum is just a blue shift of the DFT absorption spectrum. This blue-shift is due to the quasi-particle corrections that are done in the G_0W_0 calculation. It is important to note that the G_0W_0+RPA spectrum includes both light polarization along the armchair direction and zigzag direction. What we can see from the DFT spectrum it that phosphorene is transparent to polarized light along the zigzag direction for a good range of energies. That only shows the optical anisotropy of this material. When the excitonics effects are included using the BSE calculations, we can observe that the absorption spectrum is red-shifted and we can clearly see that peaks are more discrete. The first peak of the G_0W_0+BSE absorption spectrum of figure 5.14 is positioned at an energy of 0.9 eV which coincides with the position of the first peak in the DFT absorption spectrum. But this time we know that the band gap obtained by the G_0W_0 calculations is 1.8 eV giving us an excitonic binding energy of 0.9 eV. This result shows the importance of doing calculations

with energies corrected by the G_0W_0 and including the electron-hole interactions if we really want to study the optical properties of such materials. This high excitonic binding energy is expected in this material because of its low dimensionality and the low screening. The low dimensionality increases the confinement between the electron and hole which enhances its Coulomb interaction.

Few works have been done with the GW and BSE formalism for phosphoerene. In table 5.5 we summarize the results of our work and two works that we have found that use G_0W_0+BSE. When we look at table 5.5 we can

Reference	Type of calculation	1º peak [eV]	EBE [eV]
This Work	G_0W_0+BSE	0.9	0.9
[61]	G_0W_0+BSE	1.6	0.7
[63]	G_0W_0+BSE	1.2	0.8

Table 5.5: Summarized results for different works that use the BSE for phosphorene. In our work we use the results with a vacuum distance of 40 bohr.

observe that there are some differences in the results. First, every work is in qualitative agreement in relation to the physics of the absorption spectra. The first excitonic peak appears for light polarized along the armchair direction and the rest of the absorption is dominated for light polarized along the zigzag direction. The only thing that is different is the energy of the optical gap and the fundamental band gap.

These differences can be explained when we look to the parameters used in other works. In work [61] a grid of $9 \times 13 \times 1$ **k**-points is used for the computing the BSE while in work [63] a grid of $56 \times 40 \times 1$ is used. We show in our results that a much larger grid of $96 \times 96 \times 1$ **k**-points is needed in order to achieve convergence. We have also discussed in section 5.2 that the number of bands those works used for the G_0W_0 calculations were small. This will have influence in the screened potential and thereby in the BSE results.

There is also a lacking of experimental works about this material. This is because its exfoliation to single-layer is very complicated. We found an experimental work [64] that used photoluminescence techniques in order to obtain the optical gap and the fundamental band gap. The measured optical gap is 1.3 ± 0.02 eV and the fundamental band gap 2.2 ± 0.1 eV; the binding energy measured is 0.9 ± 0.12 eV. This value is in agreement with the binding energy of our work.

Other experimental work [57] also used photoluminescence techniques in phosphorene. A peak at an energy of 1.45 eV is observed and it is likely to

be of excitonic nature. That experimental value is not in total agreement with the theoretical works. But there are factors like the substrate effects, defects and doping that can have significant influence in the measurements of the optical gap and band gap energies.

Nevertheless we can see that phosphorene is indeed a material with large excitonic effects with an excitonic binding energy that can achieve values near 1.0 eV. This means that the difference between the optical gap and the fundamental gap is large.

Chapter 6

Conclusion and outlook

The goal of this dissertation was to study the electronic and optical properties of bidimensional materials, namelly single layer h-BN and phosphorene. It is well known that independent particle theories like DFT frequently do not predict correctly the electronic and optical properties of materials. For example the band gap value of the semiconductors is often underestimated when the functional LDA or GGA is used. To correct this, a theory that includes many-body effects is needed. In this work we use the *GW* approximation which includes electron-electron interactions by considering the quasi-particles.

The quasi-particles come from the electron-electron interaction and they interact with each other by a weaker potential than the Coulomb potential. We call that interaction the dynamical screening Coulomb potential. The *GW* formalism is not sufficient to predict accurately the optical properties. For that we need to include the electron-hole interactions, that is, excitonic effects. These effects have great importance for materials with low dimensionality and reduced screening which is the case of bidimensional materials. We use the BSE formalism, which uses the results from *GW* and then solves an eigenvalue problem with the electron-hole interactions.

To study the single layer h-BN and phosphorene electronic properties we did G_0W_0 calculations with the GPP model. These calculations used DFT as starting point. Our main goal was to calculate the band gap of these two materials.

For h-BN we obtained a fundamental band gap of 6.92 eV from K-Γ which corrects the band gap of 4.43 eV from K-K obtained by DFT. Due to the complexity of the *GW* approximation formalism, the results are influenced by many parameters and a convergence study is always needed, as can be seen in figure 4.9 and table 4.3. These parameters are, for instance, the dielectric cut-off, the number of bands in the Σ calculation, the vacuum size

between the periodic cells and the number of **k**-points.

For phosphorene the fundamental band gap calculated was 1.82 eV from $\Gamma - \Gamma$ correcting the 0.87 eV obtained by DFT. Just like h-BN, the value of the gap is influenced by the number of **k**-points and the vacuum size. The vacuum size dependence can be explained by the non-local nature of the *GW* approximation formalism where the screening is going to be influenced by the vacuum size. The **k**-points dependence can be explained by significant variation of the dielectric function for bidimensional materials in regions for **k**-points near the Γ point. To capture those points, finer grids are necessary, and so *GW* needs more **k**-points than DFT.

The same happens when we studied the optical properties of this materials. The optical gap is influenced by the vacuum size and the number of **k**-points used to solve the BSE equation. For h-BN an optical gap of 4.2 eV was obtained and the binding energy was 2.8 eV. For phosphorene the optical gap was 0.9 and the binding energy was 1.0 eV. These results were compared to other works as can be seen in tables 4.4, 4.5, 5.4 and 5.5. We saw that those works do not provide the necessary information about the *GW* and BSE calculations to have a clear comparison with our results. And from the information that is provided we can conclude that most of those other works did not treat the convergence studies as well as we did.

From our results it is clear that *GW* and BSE calculations are very computationally demanding because the convergence is achieved for large number of bands, dense grids and long vacuum sizes. Other works do not seem to have used such large resources, but it is doubtful that they converged their results properly.

Materials with low dimensionality are more susceptible to electron-electron and electron-hole interactions, and so theories like DFT are far for being sufficient to predict these excited properties. We showed that many-body theories like *GW* approximation and BSE can give a deeper understanding of the properties of such materials.

Appendices

Appendix A

DFT convergence studies

A.1 2D h-BN

In this appendix we show the DFT convergence studies for 2D h-BN. In figure A.1 we show the convergence of the plane-wave cut-off energy. We can see

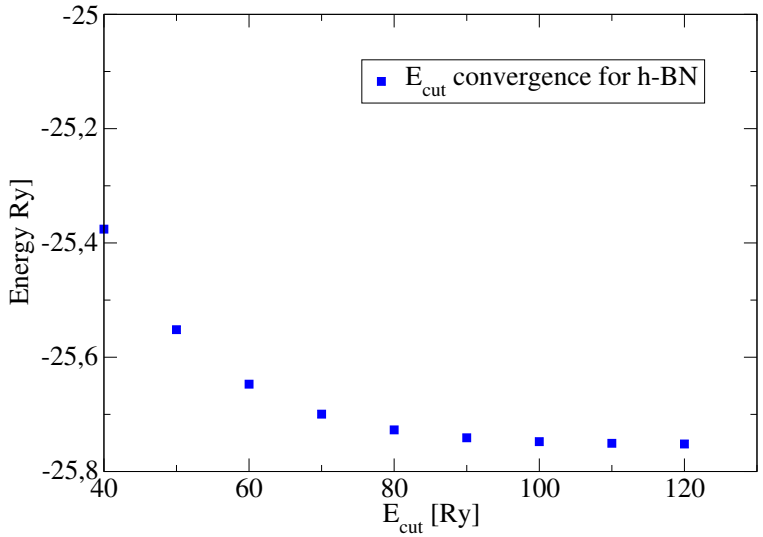

Figure A.1: Convergence study of the plane-wave cut-off energy for 2D h-BN.

that for a plane-wave cut-off (E_{cut}) greater than 80 Ry there is no significant difference in the energy value. So we choose 80 Ry as the converged value. Figure A.2 shows the convergence for the mesh of **k**-points. For a mesh greater than $6 \times 6 \times 1$ there is no significant difference in the energy value. We choose then that mesh as the converged grid. In figure A.3 we show how we found the optimized lattice parameter for 2D h-BN. When we fit a

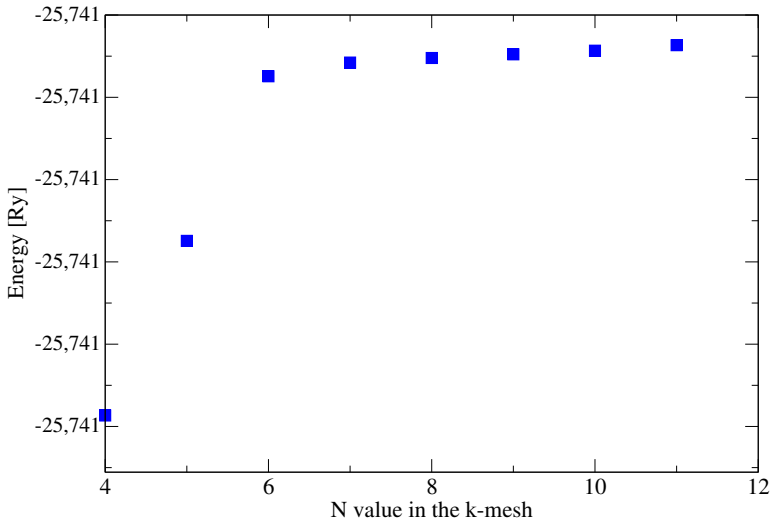

Figure A.2: Convergence study of the mesh of **k**-points for 2D h-BN.

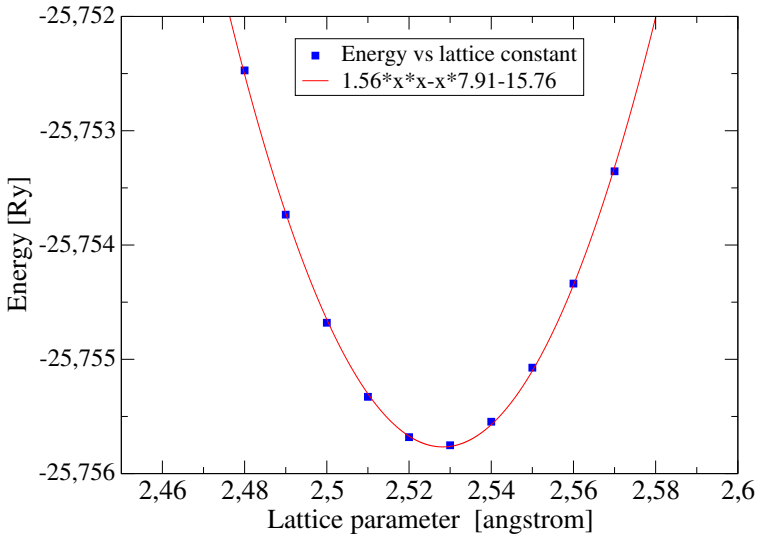

Figure A.3: Convergence study of the lattice parameter for 2D h-BN.

parabolic curve do the data, we can obtain a optimized lattice parameter of 2.54 Å. The final convergence study is the vacuum size between the periodic images, which is shown in figure A.4. We see that for a vacuum size greater than 15 bohr there is no significant difference in the energies vales. So at DFT level a vacuum size of 15 bohr is sufficient to avoid periodic interactions.

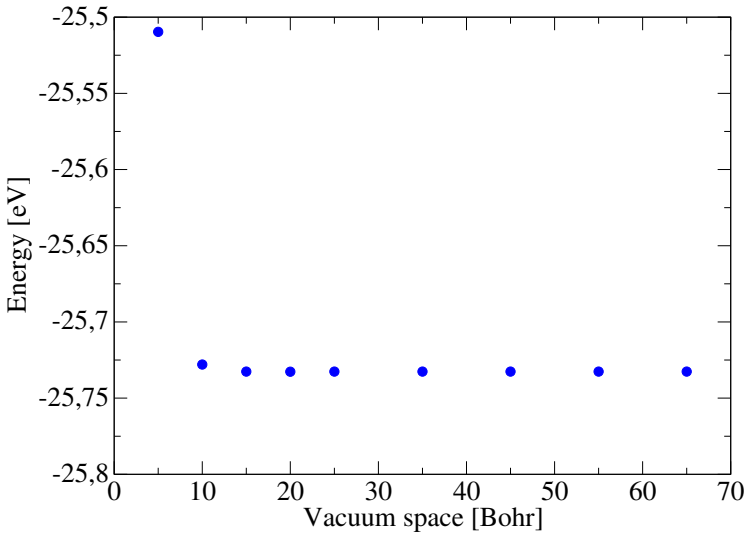

Figure A.4: Convergence study of the vacuum size between the periodic cells for 2D h-BN.

A.2 Phosphorene

Here we show the DFT convergence studies for phosphoerene. Figure A.5 shows the convergence study of the plane-wave cut-off E_{cut}. The difference

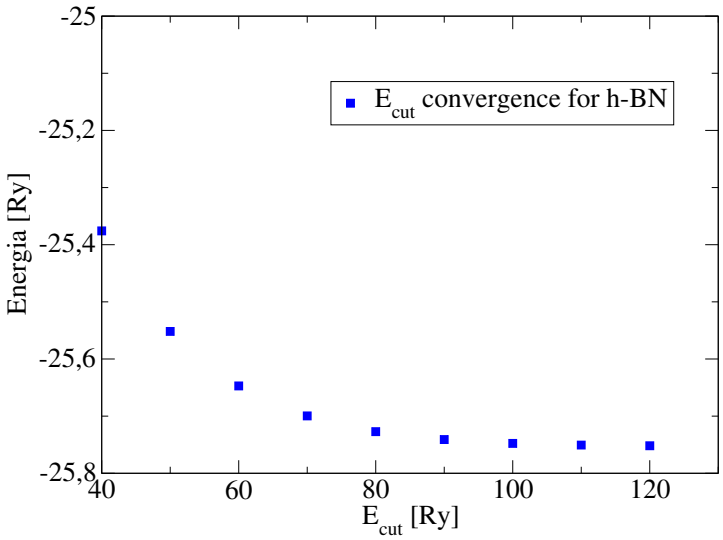

Figure A.5: Convergence study of the plane-wave cut-off energy for phosphorene.

between the energy for the E_{cut} of 70 Ry and the higher E_{cut}'s is insignificant.

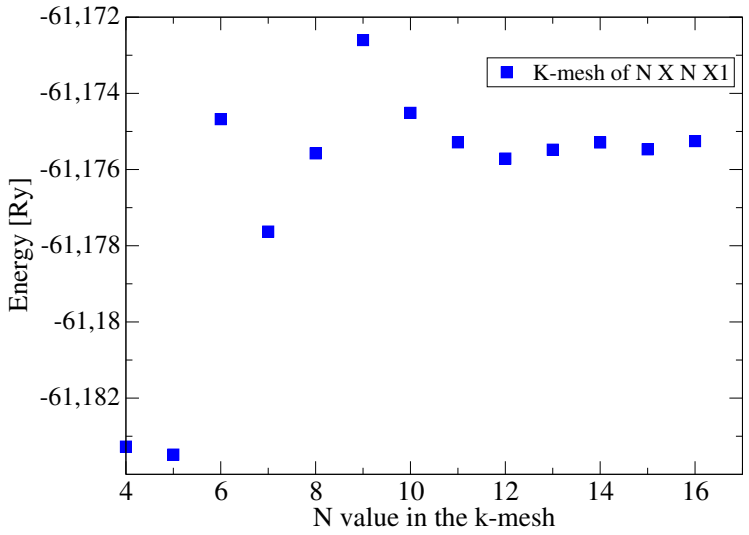

Figure A.6: Convergence study of the mesh of **k**-points for phosphoerene.

So we choose 70 Ry as the converged value. Figure A.6 shows the convergence for the mesh of **k**-points. We can see that the energy difference between the grid $8 \times 8 \times 1$ and the finer grids is very small. We choose this grid as the converged one, but we used the grid $9 \times 9 \times 1$ because of symmetry questions. In figure A.7 we show the study of the vacuum size between the periodic images. For a vacuum size greater than 20 bohr the convergence is achieved.

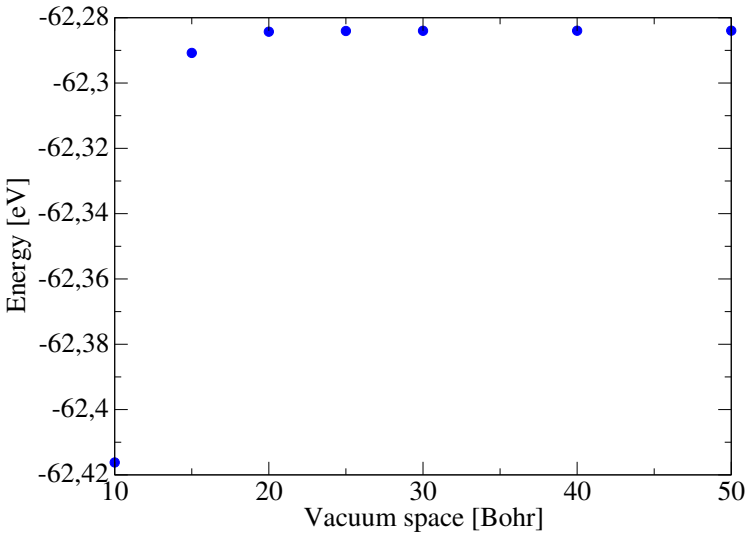

Figure A.7: Convergence study of the vacuum size between the periodic cells for phosphorene.

Appendix B

BerkeleyGW equations

In this appendix we show how the BerkeleyGW package [30] has the *GW* and BSE equations implemented numerically. The plane-wave representation is used and more detail in the BerkeleyGW manual and paper.

B.1 Calculation of Σ

BerkeleyGW (BGW) package performs *GW*-BSE calculations in three steps. In the first step the ground state properties are calculated through a single-particle formalism. This calculations can be performed by independent-particle theories, like DFT. In the second step the quasi-particle energies and wave-functions are calculated using the *GW* approximation. In the third step the excited states of the two-particle electron-hole are calculated through the Bethe-Salpeter equation. When the first step is finished, the first quantity that needs to be calculated is the polarizability or polarization function. It is implemented in the BGW package with the following expression

$$P^{r/a}_{\mathbf{GG'}}(\mathbf{q},\omega) = \sum_{n}^{occ}\sum_{n'}^{emp}\sum_{k} M^{*}_{nn'}(\mathbf{k},\mathbf{q},\mathbf{G})M_{nn'}(\mathbf{k},\mathbf{q},\mathbf{G'}) \times \frac{1}{2}\left|\frac{1}{E_{n,\mathbf{k+q}} - E_{n',\mathbf{k}} - \omega \mp i\delta} + \frac{1}{E_{n,\mathbf{k+q}} - E_{n',\mathbf{k}} - \omega \pm i\delta}\right|, \quad \text{(B.1)}$$

where

$$M_{nn'}(\mathbf{k},\mathbf{q},\mathbf{G}) = \langle n,\mathbf{k}+\mathbf{q}|\, e^{i(\mathbf{q}+\mathbf{G})\cdot\mathbf{r}}\, |n'\mathbf{k}\rangle \quad \text{(B.2)}$$

are the plane-wave matrix elements. The quantity $\mathbf{q}$ is a vector in the first Brillouin zone, $\mathbf{G}$ is a reciprocal-lattice vector, $|n,\mathbf{k}\rangle$ and $E_{n,\mathbf{k}}$ are the MF eigenvectors and eigenvalues respectively. The ω is the evaluation parameter and the the δ is a broadening parameter. This last parameter is chosen to

be consistent with the energy space afforded by the **k**-point sampling of the calculation. The upper (lower) signs corresponds to the retarded (advanced) function. The plane-wave matrix elements are evaluated up to $|\mathbf{q}+\mathbf{G}|^2$, where $|\mathbf{q}+\mathbf{G}'|^2 < E_{cut}$ defines the dielectric cut-off E_{cut}. The number of empty states included in the summation must be such that the highest empty state must have the same energy of the E_{cut}. This means that the number of empty states in the summation and the E_{cut} do not have to be converged separately. With the polarizablity matrix computed, the dielectric matrix is calculated by using the following expression

$$\epsilon_{\mathbf{GG}'}(\mathbf{q},\omega) = \delta_{\mathbf{GG}'} - v(\mathbf{q}+\mathbf{G})P_{\mathbf{GG}'}(\mathbf{q},\omega), \tag{B.3}$$

where $v(\mathbf{q}+\mathbf{G}) = \frac{4\pi}{|\mathbf{q}+\mathbf{G}|^2}$ is the Coulomb interaction. For bidimensional materials it is recommended to include truncations to avoid interactions with the periodic images. This truncations helps to speed the convergence with the super-cell size. For more information about truncations see BerkeleyGW paper [30]. The screened Coulomb interaction is calculated using the following expression

$$W_{\mathbf{GG}'}(\mathbf{q},\omega) = \epsilon^{-1}_{\mathbf{GG}'}(\mathbf{q},\omega)v(\mathbf{q}+\mathbf{G}). \tag{B.4}$$

The computation of the $W_{\mathbf{GG}'}(\mathbf{q},\omega)$ is then performed in three steps. First step, the plane-wave matrix elements are determined by equation B.2 where we have to define the E_{cut}. The second step is the summation of the plane-wave matrix elements in equation B.1. Then it is necessary to construct the dielectric matrix by using equation B.3 and invert it to compute the screened Coulomb interaction with equation B.4. In equation B.1 we have to study the convergence of the dielectric cut-off E_{cut} in conformity with the empty bands. We also have to study convergence with the increasing of **k**-point sampling adjusting the broadening parameter. Because we are doing calculations in a frequency grid of real frequencies, it is necessary to check the convergence with the frequency grid that is chosen. With the epsilon matrix calculated, we can calculate the self energy operator Σ. It is divided in two terms, $\Sigma = \Sigma_{SX} + \Sigma_{CH}$, where Σ_{SX} is the screened-exchange term and the Σ_{CH} is the Coulomb-hole term and they have the following expression

$$\begin{aligned}\langle n\mathbf{k}|\,\Sigma_{SX}(\omega)\,|n'\mathbf{k}\rangle = -\sum_{n''}^{occ}\sum_{\mathbf{qGG}'} M^*_{nn'}(\mathbf{k},-\mathbf{q},-\mathbf{G})M_{n''n'}(\mathbf{k},-\mathbf{q},-\mathbf{G}') \\ \times \epsilon^{-1}_{\mathbf{GG}'}(\mathbf{q},\omega - E_{n''\mathbf{k}-\mathbf{q}})v(\mathbf{q}+\mathbf{G}'),\end{aligned} \tag{B.5}$$

$$\langle n\mathbf{k}|\,\Sigma_{CH}(\omega)\,|n'\mathbf{k}\rangle = -\frac{i}{2\pi}\sum_{n''}\sum_{\mathbf{qGG'}} M^*_{nn'}(\mathbf{k},-\mathbf{q},-\mathbf{G})M_{n''n'}(\mathbf{k},-\mathbf{q},-\mathbf{G'}) \times \int_0^\infty d\omega' \frac{\left[\epsilon^r_{\mathbf{GG'}}\right]^{-1}(\mathbf{q},\omega') - \left[\epsilon^a_{\mathbf{GG'}}\right]^{-1}(\mathbf{q},\omega')}{\omega - E_{n''k-q} - \omega' + i\delta} v(\mathbf{q}+\mathbf{G'}), \quad \text{(B.6)}$$

where e^r and e^a are the retarded and advanced dielectric matrices. BerkeleyGW packages performs the computation of the matrix elements of the bare exchange Σ_X and of $\Sigma_{SX} - \Sigma_X$ where the Σ_X is just the equation B.5 but with $\epsilon^{-1}_{\mathbf{GG'}}$ being replaced by $\delta_{\mathbf{GG'}}$. For computing these matrices it is necessary to construct the plane-wave matrix $M_{n''n'}$ just like the case of the polarizability matrix. For the terms Σ_{SX} and Σ_{CH} we have to chose the screened-Coulomb cut-off (scc). This cut-off have the same function of the dielectric cut-off, which is to define an energy truncation for the evaluation of the elements of $M_{n''n'}$. The scc has to be less or equal to the dielectric cut-off. For the Σ_X term we have the bare-coulomb cut-off (bcc) and it can take any value up to the energy cut-off used in the DFT calculation. Besides, the convergence with respect to the number of bands included in the summation of B.6 has to be studied. The integral of equation B.6 has to be done numerically on the same frequency grid where the dielectric matrix was constructed. Now that the construction of Σ is computed, equation 3.10 can now be solved.

B.1.1 Generalised-Plasmon-Pole

The equations represented above are frequency dependent and they have to be computed in a chosen frequency axis. There is a model, called Generalised-Plasmon-Pole (GPP) proposed by Hybertson e Louie [28], where we compute the static dielectric matrix and then extend it to finite frequencies. This is done by considering the static polarizability matrix

$$\chi_{\mathbf{GG'}}(\mathbf{q},0) = \sum_{\mathbf{k}}^{occ}\sum_{n}^{emp}\sum_{n'} M^*_{nn'}(\mathbf{k},\mathbf{q},\mathbf{G})M_{nn'}(\mathbf{k},\mathbf{q},\mathbf{G'})\frac{1}{E_{n,\mathbf{k+q}} - E_{n',\mathbf{k}}}. \quad \text{(B.7)}$$

The static dielectric matrix is calculated by using the following expression

$$\epsilon_{\mathbf{GG'}}(\mathbf{q},0) = \delta_{\mathbf{GG'}} - v(\mathbf{q}+\mathbf{G})\chi_{\mathbf{GG'}}(\mathbf{q},0) \quad \text{(B.8)}$$

and the static screened Coulomb interaction is

$$W_{\mathbf{GG'}}(\mathbf{q},0) = \epsilon^{-1}_{\mathbf{GG'}}(\mathbf{q},0)v(\mathbf{q}+\mathbf{G}). \quad \text{(B.9)}$$

To compute the static dielectric matrix, there is only one convergence parameter, which is the dielectric cut-off or the number of empty bands (which have to be in conformity with each other).

The imaginary part of W is in generally characterized by a strong peak that corresponds to the plasmon excitations at the plasmon frequency. The PPA assume that all weight of the Im W is at the plasmon excitation. Then we can write the imaginary part of dielectric functions as

$$\text{Im } \epsilon^{-1}_{\mathbf{GG'}}(\mathbf{q},\omega) = A_{\mathbf{GG'}}(\mathbf{q})\delta(\omega - \tilde{\omega}_{\mathbf{GG'}}(\mathbf{q})), \tag{B.10}$$

where $A_{\mathbf{GG'}}$ and $\tilde{\omega}_{\mathbf{GG'}}$ are parameters that we need to determine. The real part is given by:

$$\text{Re } \epsilon^{-1}_{\mathbf{GG'}}(\mathbf{q},\omega) = \delta_{\mathbf{GG'}} + \frac{\Omega^2_{\mathbf{GG'}}(\mathbf{q})}{\omega^2 - \tilde{\omega}^2_{\mathbf{GG'}}(\mathbf{q})} \tag{B.11}$$

where $\Omega_{\mathbf{GG'}}$ is the effective plasma frequency. The unknown parameters $A_{\mathbf{GG'}}(\mathbf{q})$ and $\omega_{\mathbf{GG'}}(\mathbf{q})$ can be determined by using the static limit of ϵ^{-1},

$$\text{Re } \epsilon^{-1}_{\mathbf{GG}},(\mathbf{q},0) = \delta_{\mathbf{GG}}, + \frac{2}{\pi}P\int_0^\infty d\omega \frac{1}{\omega}\text{Im } \epsilon^{-1}_{\mathbf{GG}},(\mathbf{q},\omega), \tag{B.12}$$

and by the f-sum rule,

$$\int_0^\infty \text{Im } \epsilon^{-1}_{\mathbf{GG}},(\mathbf{q},\omega) = -\frac{\pi}{2}\omega_p^2 \frac{(\mathbf{q}+\mathbf{G}).(\mathbf{q}+\mathbf{G'})}{|\mathbf{q}+\mathbf{G}|^2}\frac{\rho(\mathbf{G}-\mathbf{G'})}{\rho(0)} = -\frac{\pi}{2}\Omega^2_{\mathbf{GG'}}, \tag{B.13}$$

where ρ is the electron charge density in reciprocal space and ω_p^2 is the classical plasma frequency defined by $\omega_p^2 = 4\pi\rho(0)e^2/m$. This allows us to write equation B.5 and B.6 as

$$\begin{aligned}\langle n\mathbf{k}|\,\Sigma_{SX}(\omega)\,|n'\mathbf{k}\rangle = &-\sum_{n''}^{occ}\sum_{\mathbf{qGG'}} M^*_{nn'}(\mathbf{k},-\mathbf{q},-\mathbf{G})M_{n''n'}(\mathbf{k},-\mathbf{q},-\mathbf{G'}) \\ &\times\left[\delta_{\mathbf{GG'}} + \frac{\Omega^2_{\mathbf{GG'}}(\mathbf{q})(1 - i\ \tan\phi_{\mathbf{GG'}}(\mathbf{q}))}{(\omega - E_{n''\mathbf{k}-\mathbf{q}})^2 - \tilde{\omega}^2_{\mathbf{GG'}}(\mathbf{q})}\right] v(\mathbf{q}+\mathbf{G'}),\end{aligned} \tag{B.14}$$

$$\begin{aligned}\langle n\mathbf{k}|\,\Sigma_{CH}(\omega)\,|n'\mathbf{k}\rangle = &-\frac{1}{2}\sum_{n''}\sum_{\mathbf{qGG'}} M^*_{nn'}(\mathbf{k},-\mathbf{q},-\mathbf{G})M_{n''n'}(\mathbf{k},-\mathbf{q},-\mathbf{G'}) \\ &\times\int_0^\infty d\omega' \frac{\Omega^2_{\mathbf{GG'}}(\mathbf{q})(1 - i\ \tan\phi_{\mathbf{GG'}}(\mathbf{q}))}{\tilde{\omega}_{\mathbf{GG'}}(\mathbf{q})(\omega - E_{n''\mathbf{k}-\mathbf{q}} - \tilde{\omega}_{\mathbf{GG'}}(\mathbf{q}))} v(\mathbf{q}+\mathbf{G'}).\end{aligned} \tag{B.15}$$

The $\Omega_{\mathbf{GG'}}$ and $\tilde{\omega}_{\mathbf{GG'}}$ are related by

$$\tilde{\omega}_{\mathbf{GG'}}(\mathbf{q})) = \frac{|\lambda_{\mathbf{GG'}}(\mathbf{q})|}{\cos\phi_{\mathbf{GG'}}(\mathbf{q})}, \tag{B.16}$$

$$|\lambda_{\mathbf{GG'}}(\mathbf{q})|\, e^{i\phi_{\mathbf{GG'}}}(\mathbf{q}) = \frac{\Omega^2_{\mathbf{GG'}}(\mathbf{q})}{\delta_{\mathbf{GG'}} - \epsilon^{-1}_{\mathbf{GG'}}(\mathbf{q},0)}, \tag{B.17}$$

where $\lambda_{\mathbf{GG'}}(\mathbf{q})$ and $\phi_{\mathbf{GG'}}(\mathbf{q})$ are the amplitude and the phase of the renormalized $\Omega^2_{\mathbf{GG'}}(\mathbf{q})$ respectively.

B.2 Bethe Salpeter equation

In the BerkeleyGW package the BSE is given by

$$(E_{c\mathbf{k}} - E_{v\mathbf{k}})\, A^S_{vc\mathbf{k}} + \sum_{v'c'\mathbf{k}'} \langle vc\mathbf{k}|\, K^{eh}\, |v'c'\mathbf{k}'\rangle = \Omega^S A_{vc\mathbf{k}} \tag{B.18}$$

where $E_{c\mathbf{k}}$ and $E_{v\mathbf{k}}$ are the conduction and valence quasi-particle energies, K^{eh} the electron-hole Kernel, $A^S_{vc\mathbf{k}}$ and Ω^S the excitonic wavefunction and excitonic energy respectively for a excitonic state S. The Tamm-Dancoff approximation is considered, where only valence to conduction transitions are included. The first step before solving the BSE is to compute the electron-hole kernel. It can be separated in two terms, $K^{eh} = K^d + K^x$, where K^d is the screened direct interaction term and K^x is the bare exchange interaction term. They are defined in the following way

$$\langle vc\mathbf{k}|\, K^d\, |v'c'\mathbf{k}'\rangle = \int dr dr' \psi^*_{c\mathbf{k}}(\mathbf{r})\psi_{c'\mathbf{k}'}(\mathbf{r}) W(\mathbf{r},\mathbf{r}')\psi^*_{v'\mathbf{k}'}(\mathbf{r}')\psi_{c\mathbf{k}}(\mathbf{r}'), \tag{B.19}$$

$$\langle vck|\, K^x\, |v'c'\mathbf{k}'\rangle = \int dr dr' \psi^*_{c\mathbf{k}}(\mathbf{r})\psi_{v\mathbf{k}}(\mathbf{r}) v(\mathbf{r},\mathbf{r}')\psi^*_{v'\mathbf{k}'}(\mathbf{r}')\psi_{c'\mathbf{k}'}(\mathbf{r}'), \tag{B.20}$$

where the static approximation for W is considered. This matrix is often calculated using the same grid of $\mathbf{k}$-points used in the previous GW calculation where the dielectric matrix $\epsilon^{-1}(\mathbf{q})$ for $\mathbf{q} = \mathbf{k} - \mathbf{k}'$ was constructed. The matrices B.19 and B.20 are constructed in the $\mathbf{G}$-space in the following way

$$\langle vc\mathbf{k}|\, K^d\, |v'c'\mathbf{k}'\rangle = \sum_{\mathbf{GG'}} M^*_{c'c}(\mathbf{k},\mathbf{q},\mathbf{G}) W_{\mathbf{GG'}}(\mathbf{q},0) M_{v'v}(\mathbf{k},\mathbf{q},\mathbf{G}') \tag{B.21}$$

$$\langle vc\mathbf{k}|\, K^x\, |v'c'\mathbf{k}'\rangle = \sum_{\mathbf{G}\neq 0} M^*_{vc}(\mathbf{k},\mathbf{q},\mathbf{G}) v_{\mathbf{k}+\mathbf{G}}(\mathbf{q},0) M_{v'c'}(\mathbf{k},\mathbf{q},\mathbf{G}') \tag{B.22}$$

where M is defined in equation B.2 which means that we have to chose a cut-off for the kernel matrix construction. The excitonic properties are very sensitive to the grid of **k**-points that is used because the contributions of $\mathbf{q} \to 0$ are very important. This means we have to compute the kernel in very fine grids. The problem is that such thing is prohibitively expensive and another method has to be used. The BerkeleyGW package computes the kernel with a coarse grid of **k**-points by using the `kernel` executable and then interpolate it in a very fine grid of **k**-points before the diagonalization using the `absorption` executable. In the `absorption` executable the coarse and fine grid wavefunctions are needed as input so we have to do DFT calculations in a finer grid. This interpolation is done in such way that now the BSE depends on the number of valence bands and conduction bands from the coarse, as can be seen in equation B.21 and B.20, and it also depends on the number of valence bands and conduction bands from the fine grid.

After the diagonalization we can get the set of excitonic eigenvalues Ω^S and eigenfuctions $A^S_{vc\mathbf{k}}$ which can be used to calculate the absorption spectrum.

Appendix C

BerkeleyGW calculation tutorial

In this tutorial we show how to perform a simple G_0W_0 calculation using the Generalised-Plamon-Pole proposed by Hybertson and Louie [28] and solve the Bethe-Salpeter equation (BSE) by using the QUANTUM ESPRESSO [36] (QE) and BERKELEYGW [30] (BGW) packages. We choose the semiconductor h-BN has the reference material and we will show the procedure to calculate its quasi-particle energies and the absorption spectrum.

C.1 G_0W_0 calculation

First it is necessary to perform DFT calculations that will be the starting point for the G_0W_0. We use QE to perform DFT calculations. A plane-wave cut-off of 80 Ry and a grid of **k**-points of $12 \times 12 \times 1$ with a shift of $1 \times 1 \times 0$ are used. When the DFT calculations are done, we have to convert the information to new files that will be read by the BGW. The recommended approach for the QE calculations is the following (see figure from the link "http://www.nersc.gov/assets/Uploads/Davidpracticalcalc.pptx.pdf" page 10):

1. `scf` calculation with `pw.x` (uniform grid with a shift of 0.5 and number of bands (`nbnb`) equal to the number of occupied bands).

2. `bands` calculation with `pw.x` (uniform grid with a shift of 0.5 and a large number of bands possible). After the `pw.x` calculation we have to convert the data using the `pw2bgw.x` to create the file `WFN`.

3. `bands` calculation with `pw.x` (uniform grid with a shift of 0.5, a **q**-shift and number of bands (`nbnb`) equal to the number of occupied

bands). After the `pw.x` calculation we have to convert the data using the `pw2bgw.x` to create the file `WFNq`.

4. `bands` calculations with `pw.x` (uniform grid with no shift and a large number of bands possible). After the `pw.x` calculation we have to convert the data using the `pw2bgw.x` to create the file `WFN_inner`.

5. `bands` calculations with `pw.x` (in our case we will use the program `inteqp.cplx.x` to do an interpolation for plot the quasi-particle electronic band-structure where we have to choose the **k**-point path and include few unoccupied bands). After the `pw.x` calculation we have to convert the data using the `pw2bgw.x` to create the file `WFN_fi`.

In the step 1, a `scf` calculation is done. It is not necessary to include more bands than the occupied ones. A good plane-wave cut-off and a grid of **k**-points has to be used (it is necessary to study the convergence). A automatic grid of **k**-points with a shift of 0.5 has to be used, for example: $12 \times 12 \times 1$ with a shift of $1 \times 1 \times 0$. The following calculations must have the same plane-wave cut-off used in the `scf` calculation.

In the setp 2 it is necessary to do a `bands` calculation with a large value of unoccupied bands with a generated uniform grid of **k**-points with 0.5 shift. To generate this grid the `kgrid.x` program that is included in the BGW package can be used. The input structure for the `kgrid.x` can be seen in the BGW manual page 23. In our case (h-BN, plane-wave cut-off 80 Ry, $12 \times 12 \times 1$ with shift $1 \times 1 \times 0$) the input for the `kgrid.x` for the step 2, which we call `kgrid.wfn.inp`, has the following content:

```
#kgrid.wfn.inp for  WFN

12 12 1   #k-points
0.5 0.5 0.0 #shift in k-points
0.0 0.0 0.0 #shift in q-points

#lattice vectors in Cartesian coordinates:
4.14   2.391    0.00
4.14  -2.391    0.00
0.00   0.000   50.00


2 #Number of atoms
1  0.0000000   0.0000000   0.0000000     #Cartesian coordinates
2  2.7603155   0.0000000   0.0000000
27 27 288               #FFT dimensions
.false.  #use time-reversal symmetry. Set to false for BerkeleyGW
```

The FFT dimensions can be taken from the output file of the `scf` calculation done in the step 1. For generate the **k**-points with `kgrid.x` we have to execute the following command:

```
kgrid.x kgrid.wfn.in kgrid.wfn.out kgrid.wfn.log
```

The `kgrid.wfn.out` gives us the **k**-points list for the input file for the `pw.x` calculation in step 2. In our case we have:

```
&CONTROL
                      title = 'BN' ,
                calculation = 'bands' ,
                 wf_collect = .true. ,
                   ...

 /
 &SYSTEM
                     ...
                    ecutwfc = 80.0,
                       nbnd = 1000,
                    ...

 /
 &ELECTRONS
 ...
 diagonalization ='cg'
 ...
 /
CELL\_PARAMETERS hexagonal
  ..
 ATOMIC\_SPECIES
  ...
ATOMIC\_POSITIONS (crystal)
...
K_POINTS crystal
   78
  0.041666667  0.041666667  0.000000000   1.0
  0.041666667  0.125000000  0.000000000   2.0
  0.041666667  0.208333333  0.000000000   2.0
  0.041666667  0.291666667  0.000000000   2.0
  0.041666667  0.375000000  0.000000000   2.0
  0.041666667  0.458333333  0.000000000   2.0
  0.041666667  0.541666667  0.000000000   2.0
  0.041666667  0.625000000  0.000000000   2.0
  0.041666667  0.708333333  0.000000000   2.0
  0.041666667  0.791666667  0.000000000   2.0
  0.041666667  0.875000000  0.000000000   2.0
  0.041666667  0.958333333  0.000000000   2.0
  0.125000000  0.125000000  0.000000000   1.0
  0.125000000  0.208333333  0.000000000   2.0
  0.125000000  0.291666667  0.000000000   2.0
  0.125000000  0.375000000  0.000000000   2.0
  0.125000000  0.458333333  0.000000000   2.0
  0.125000000  0.541666667  0.000000000   2.0
  0.125000000  0.625000000  0.000000000   2.0
  0.125000000  0.708333333  0.000000000   2.0
  0.125000000  0.791666667  0.000000000   2.0
  0.125000000  0.875000000  0.000000000   2.0
  0.125000000  0.958333333  0.000000000   2.0
  0.208333333  0.208333333  0.000000000   1.0
  0.208333333  0.291666667  0.000000000   2.0
  0.208333333  0.375000000  0.000000000   2.0
  0.208333333  0.458333333  0.000000000   2.0
  0.208333333  0.541666667  0.000000000   2.0
```

```
  0.208333333  0.625000000  0.000000000   2.0
  0.208333333  0.708333333  0.000000000   2.0
  0.208333333  0.791666667  0.000000000   2.0
  0.208333333  0.875000000  0.000000000   2.0
  0.208333333  0.958333333  0.000000000   2.0
  0.291666667  0.291666667  0.000000000   1.0
  0.291666667  0.375000000  0.000000000   2.0
  0.291666667  0.458333333  0.000000000   2.0
  0.291666667  0.541666667  0.000000000   2.0
  0.291666667  0.625000000  0.000000000   2.0
  0.291666667  0.708333333  0.000000000   2.0
  0.291666667  0.791666667  0.000000000   2.0
  0.291666667  0.875000000  0.000000000   2.0
  0.291666667  0.958333333  0.000000000   2.0
  0.375000000  0.375000000  0.000000000   1.0
  0.375000000  0.458333333  0.000000000   2.0
  0.375000000  0.541666667  0.000000000   2.0
  0.375000000  0.625000000  0.000000000   2.0
  0.375000000  0.708333333  0.000000000   2.0
  0.375000000  0.791666667  0.000000000   2.0
  0.375000000  0.875000000  0.000000000   2.0
  0.375000000  0.958333333  0.000000000   2.0
  0.458333333  0.458333333  0.000000000   1.0
  0.458333333  0.541666667  0.000000000   2.0
  0.458333333  0.625000000  0.000000000   2.0
  0.458333333  0.708333333  0.000000000   2.0
  0.458333333  0.791666667  0.000000000   2.0
  0.458333333  0.875000000  0.000000000   2.0
  0.458333333  0.958333333  0.000000000   2.0
  0.541666667  0.541666667  0.000000000   1.0
  0.541666667  0.625000000  0.000000000   2.0
  0.541666667  0.708333333  0.000000000   2.0
  0.541666667  0.791666667  0.000000000   2.0
  0.541666667  0.875000000  0.000000000   2.0
  0.541666667  0.958333333  0.000000000   2.0
  0.625000000  0.625000000  0.000000000   1.0
  0.625000000  0.708333333  0.000000000   2.0
  0.625000000  0.791666667  0.000000000   2.0
  0.625000000  0.875000000  0.000000000   2.0
  0.625000000  0.958333333  0.000000000   2.0
  0.708333333  0.708333333  0.000000000   1.0
  0.708333333  0.791666667  0.000000000   2.0
  0.708333333  0.875000000  0.000000000   2.0
  0.708333333  0.958333333  0.000000000   2.0
  0.791666667  0.791666667  0.000000000   1.0
  0.791666667  0.875000000  0.000000000   2.0
  0.791666667  0.958333333  0.000000000   2.0
  0.875000000  0.875000000  0.000000000   1.0
  0.875000000  0.958333333  0.000000000   2.0
  0.958333333  0.958333333  0.000000000   1.0
```

We can see that it is a `bands` calculation, with a plane-wave cut-off `ecutwfc` of 80 eV and we choose the value 1000 as the number of bands (`nbnds`). The 78 **k**-points are generated by the `kgrid.x`. We choose the flag `diagonalization ='cg'` because it is more robust than `diagonalization ='david'` calculation (see BGW manual page 22). Note: The input file for he `pw.x` calculation in step 2 is equal to the `scf` file in step 1 with the difference being in the type of calculation, the number of bands, and the **k**-points.

After the pw.x calculation in step 2 is done, it is necessary to convert the information/data of QE files to new files that will be read by the BGW. For that we have to use the pw2bgw.x which is included in the QE package. The input structure of this file can be seen in the BGW manual page 25). We have the following example which we call BN.wfn.pp.in:

```
&input_pw2bgw

#BN.wfn.pp.in file

   prefix = 'BN'
   outdir = './'
   real_or_complex = 2
   wfng_flag = .true.
   wfng_file = 'WFN'
   wfng_kgrid = .true.
   wfng_nk1 = 12
   wfng_nk2 = 12
   wfng_nk3 = 1
   wfng_dk1 = 0.5
   wfng_dk2 = 0.5
   wfng_dk3 = 0.0
   /
```

The more important flag in this file is the real_or_complex. If the system has inversion symmetry and time-reversal symmetry than we can use real_or_complex = 1 which will turn the calculations more faster. Otherwise we have to use real_or_complex = 2. Our example has not inversion symmetry. The other flags are just information for converting the data of the pw.x calculation to the file WFN (see BGW manual page 25). Now we have to execute the command:

pw2bgw.x <BN.wfn.pp.in> pp.wfn.out.

If everything is done correctly, a file named WFN is going to be created. To create the files WFNq and WFN_inner the procedure is the same of step 2. In step 3 we can generate the **k**-points with kgrid.x just like in step 2. The difference is that we want a small shift in the **q**-points. The input file, which we call kgrid.wfnq.in, has the following content:

```
#kgrid.wfnq.inp for  WFNq

12 12 1
0.5 0.5 0.0
0.001 0.0 0.0
... # The rest is equal to kgrid.wfn.in
```

After executing the command

kgrid.x kgrid.wfnq.in kgrid.wfnq.out kgrid.wfnq.log,

it will be generated a file `kgrid.wfnq.out` with more **k**-points than `kgrid.wfn.out` because of the additional shift. Now that the list of **k**-points is generated we have to create the `pw.x` file for step 3. This file will be the same as the file of step 2 but now the list of **k**-points is the one given by `kgrid.wfnq.out` and it not necessary to include empty bands. After the `pw.x` calculation, we have to use `pw2bgw.x` again to create the `WFNq` file. The `pw2bgw.x` input file, which we call `BN.wfnq.pp.in`, has the following structure:

```
#BN.wfnq.pp.in file

&input_pw2bgw
   prefix = 'BN'
   real_or_complex = 2
   wfng_flag = .true.
   wfng_file = 'WFNq'
   wfng_kgrid = .true.
   wfng_nk1 = 12
   wfng_nk2 = 12
   wfng_nk3 = 1
   wfng_dk1 = 0.5012
   wfng_dk2 = 0.5
   wfng_dk3 = 0.0
/
```

After executing the command

`pw2bgwx.x <BN.wfnq.pp.in> wfnq.pp.out`,

a file named `WFNq` is going to be created.

In the step 4 we can also generate the **k**-points with the `kgrid.x` but this time we do not want any shift and we want many empty bands. The input for the `kgrid.x`, which we call kgrid.wfn_inner.in, is the following:

```
#kgrid.wfn_inner.inp for  WFN_inner


12 12 1
0.0 0.0 0.0
0.0 0.0 0.0
... # the rest is the same of kgrid.wfn.in
```

The `pw.x` file will be the same as BN.wfn.in but with the list of **k**-points given by `kgrid.wfn_inner.out`. The input file for `pw2bgw.x` is going to have more content than `BN.wfn.pp.in` and `BN.wfnq.pp.in`. This file, which we call `BN.wfn_inner.pp.in`, will have the following content:

```
#BN.wfn_inner.pp.in file


&input_pw2bgw
   prefix = 'BN'
   real_or_complex = 2
   wfng_flag = .true.
   wfng_file = 'WFN_inner'
   wfng_kgrid = .true.
   wfng_nk1 = 12
   wfng_nk2 = 12
   wfng_nk3 = 1
   wfng_dk1 = 0.0
   wfng_dk2 = 0.0
   wfng_dk3 = 0.0
   rhog_flag = .true.
   rhog_file = 'RHO'
   vxcg_flag = .false.
   vxcg_file = 'vxc.real'
   vxc_flag = .true.
   vxc_file = 'vxc.dat'
   vxc_diag_nmin = 1
   vxc_diag_nmax = 1000
   vxc_offdiag_nmin = 1
   vxc_offdiag_nmax = 1000
/
```

This file has more content than the previous files because this one is going to create the file for electronic charge density (`RHO`) and it will create a file with the elements of exchange-correlation potential (`vxc.dat`). See page 27-29 of BGW manual for more information about the flags. After executing the command

`pw2bgw.x <MoS2.wfn_innner.pp.in> wfn_inner.pp.out`,

the files `WFN_inner`, `RHO` and `vxc.dat` are going to be created.

In the step 5 we will do a `bands` calculation with `pw.x` but this time we choose the **k**-points path. This path is going to be used to do an interpolation more later. It is not necessary to generate the **k**-points with the `kgrid.x` and include many unoccupied bands (only few). An example of the chosen path (K-Γ-M-K) for the file `BN.kpath.in` which is the input file for the `pw.x` calculation in step 5, is represented below:

```
K_POINTS crystal_b
4
0.3333333333 0.6666666667 0.0000000000     25.0
0.0000000000 0.0000000000 0.0000000000     25.0
0.0000000000 0.5000000000 0.0000000000     25.0
0.3333333333 0.6666666667 0.0000000000     1.0
```

It is necessary to create the `WFN_fi` file using the `pw2bgw.x`. The input file for `pw2bgw.x` for step 4, which we call `MoS2.kpath.pp.in`, has the following

structure:

```
#BN.wfn_fi.pp.in file

&input_pw2bgw
   prefix = 'MoS2'
   real_or_complex = 2
   wfng_flag = .true.
   wfng_file = 'WFN_fi'
/
```

After executing the command

`pw2bgw.x <MoS2.wfn_fi.pp.in> wfn_fi.pp.out` ,

the file `WFN_fi` will be created. At this stage we have done all calculations with DFT for the G_0W_0 calculation. The files that were created are `WFN` , `WFNq` , `WFN_inner`, `WFN_fi`, `RHO` and `vxc.dat`. These are the files that BGW needs in order to do a G_0W_0 calculation with the GPP.

So to synthesise what has been written till here, we write the whole procedure of the DFT calculations (which can be done in the same folder one by one or can be done in different folders with the necessity of using links):

- `pw.x <BN.scf.in> scf.out` (`scf` calculation with uniform grid and a shift of 0.5 with only occupied bands).
- `pw.x <BN.wfn.in> wfn.out` (`bands` calculation with uniform grid with a shift of 0.5 and many unoccupied bands).
- `pw2bgw.x <BN.wfn.pp.in> pp.wfn.out` (convert QE data with `pw2bgw.x` to create the `WFN` file).
- `pw.x <BN.wfnq.in> wfnq.out` (`bands` calculation with uniform grid, a shift of 0.5 and small shift only with occupied bands).
- `pw2bgw.x <BN.wfnq.pp.in> pp.wfnq.out` (convert QE data with `pw2bgw.x` to create the `WFNq` file).
- `pw.x <BN.wfn_inner.in> wfn_inner.out` (`bands` calculation with uniform grid and many unoccupied bands).
- `pw2bgw.x <BN.pp.wfn_inner.in> pp.wfn_inner.out` (convert QE data with `pw2bgw.x` to create the `WFN_inner`, `RHO` and `vxc.dat` files).
- `pw.x <BN.kpath.in> kpath.out` (`bands` calculation with with a **k**-point path chosen by us and few empty bands).

- `pw2bgw.x <BN.kapth.pp.in> pp.kpath.out` (convert QE data with `pw2bgw.x` to create the `WFN_fi`).

Now that we have all necessary files for the starting point of G_0W_0 calculation, it is time to compute the dielectric matrix of equation B.3. Because we use the GPP model we do not need to compute the frequency dependent dielectric matrix but the static one of equation B.8. The `epsilon.cplx.x` is the program to construct the dielectric matrix. If the system had inversion and time-reversal symmetry we could use the `epsilon.real.x` which can be faster than `epsilon.cplx.x`. This program needs the files `WFN`, `WFNq` and the `epsilon.inp` which is the input file (see page 59 of BerkeleyGW manual). In our example the `epsilon.inp` has the following content:

```
epsilon_cutoff 21.1

number_bands 998

band_occupation 4*1 994*0

frequency_dependence 0

begin qpoints
  0.001000000  0.000000000  0.000000000   1.0  1
  0.000000000  0.083333333  0.000000000   1.0  0
  0.000000000  0.166666667  0.000000000   1.0  0
  0.000000000  0.250000000  0.000000000   1.0  0
  0.000000000  0.333333333  0.000000000   1.0  0
  0.000000000  0.416666667  0.000000000   1.0  0
  0.000000000  0.500000000  0.000000000   1.0  0
  0.000000000  0.583333333  0.000000000   1.0  0
  0.000000000  0.666666667  0.000000000   1.0  0
  0.000000000  0.750000000  0.000000000   1.0  0
  0.000000000  0.833333333  0.000000000   1.0  0
  0.000000000  0.916666667  0.000000000   1.0  0
  0.083333333  0.166666667  0.000000000   1.0  0
  0.083333333  0.250000000  0.000000000   1.0  0
  0.083333333  0.333333333  0.000000000   1.0  0
  0.083333333  0.416666667  0.000000000   1.0  0
  0.083333333  0.500000000  0.000000000   1.0  0
  0.083333333  0.583333333  0.000000000   1.0  0
  0.083333333  0.666666667  0.000000000   1.0  0
  0.083333333  0.750000000  0.000000000   1.0  0
  0.083333333  0.833333333  0.000000000   1.0  0
  0.166666667  0.333333333  0.000000000   1.0  0
  0.166666667  0.416666667  0.000000000   1.0  0
  0.166666667  0.500000000  0.000000000   1.0  0
  0.166666667  0.583333333  0.000000000   1.0  0
  0.166666667  0.666666667  0.000000000   1.0  0
  0.166666667  0.750000000  0.000000000   1.0  0
  0.250000000  0.500000000  0.000000000   1.0  0
  0.250000000  0.583333333  0.000000000   1.0  0
  0.250000000  0.666666667  0.000000000   1.0  0
  0.333333333  0.666666667  0.000000000   1.0  0
end
```

First we have to choose the `epsilon_cutoff` which is the cut-off used for the construction of the matrix of equation B.2. This cut-off should have the same energy of the last band that is included in the polarization function of equation B.1. We choose 998 as the number of bands where the last band has an energy of 287 eV. Such information can be taken from the outputs of DFT calculations. We set then the `epsilon_cutoff` as 21.1 Ry. In `bands_occupation` we have to write the number of occupied bands and empty bands where 1 is for the occupied and 0 for the empty bands. For the flag `frequency_dependence` we can choose the value 0 which is to compute the static epsilon matrix and 2 for compute the frequency dependent dielectric matrix. We are doing a PPA calculation so we choose 0. Then we have to write a block with the **q**-points which are the **q**-points where the dielectric matrix is going to be computed. These **q**-points are the same as the `WFN_inner` (or `WFN` without any shift). The zero vector has to be replaced by a very small vector like 0.001 0.000 0.000. This is due to divergence issues.

Now that we have created our `epsilon.inp` we can execute the command

```
epsilon.cplx.x <epsilon.inp> epsilon.out.
```

If the calculation is done without any problems, the files `eps0mat`, `epsmat`, `epsilon.out`, `epsilon.log` and `chi_converge.dat` are created. The file `eps0mat` is the construction of the inverted dielectric matrix for the small **q**-point of the block list of `epsilon.inp`. The file `epsmat` is the construction of the inverted dielectric matrix for the rest of the **q**-points. In the `epsilon.out` we can see the output with the calculation procedure where we can see for example the computational time for each **q**-point. In the `epsilon.log` we can see the data of the dielectric matrix and in `chi_converge.dat` we can see the convergence of the polarization function with the number of bands.

With the static-dielectric matrix we can now use the GPP model to extend the matrix for finite frequencies and calculate the self-energy operator. That is done with the program `sigma.cplx.x`. To use this program the files `WFN_inner`, `RHO`, `vxc.dat`, `eps0mat`, `epsmat` are needed. The input file is `sigma.inp` where its content can be seen in the BGW manual page 69. In our example, the `sigma.inp` has the following content:

```
screened_coulomb_cutoff 21.1

bare_coulomb_cutoff 80.0

number_bands 998
band_occupation 4*1 994*0

frequency_dependence 1
```

```
band_index_min 1
band_index_max 10

screening_semiconductor

begin kpoints
  0.000000000  0.000000000  0.000000000  1.0
  0.000000000  0.083333333  0.000000000  1.0
  0.000000000  0.166666667  0.000000000  1.0
  0.000000000  0.250000000  0.000000000  1.0
  0.000000000  0.333333333  0.000000000  1.0
  0.000000000  0.416666667  0.000000000  1.0
  0.000000000  0.500000000  0.000000000  1.0
  0.000000000  0.583333333  0.000000000  1.0
  0.000000000  0.666666667  0.000000000  1.0
  0.000000000  0.750000000  0.000000000  1.0
  0.000000000  0.833333333  0.000000000  1.0
  0.000000000  0.916666667  0.000000000  1.0
  0.083333333  0.166666667  0.000000000  1.0
  0.083333333  0.250000000  0.000000000  1.0
  0.083333333  0.333333333  0.000000000  1.0
  0.083333333  0.416666667  0.000000000  1.0
  0.083333333  0.500000000  0.000000000  1.0
  0.083333333  0.583333333  0.000000000  1.0
  0.083333333  0.666666667  0.000000000  1.0
  0.083333333  0.750000000  0.000000000  1.0
  0.083333333  0.833333333  0.000000000  1.0
  0.166666667  0.333333333  0.000000000  1.0
  0.166666667  0.416666667  0.000000000  1.0
  0.166666667  0.500000000  0.000000000  1.0
  0.166666667  0.583333333  0.000000000  1.0
  0.166666667  0.666666667  0.000000000  1.0
  0.166666667  0.750000000  0.000000000  1.0
  0.250000000  0.500000000  0.000000000  1.0
  0.250000000  0.583333333  0.000000000  1.0
  0.250000000  0.666666667  0.000000000  1.0
  0.333333333  0.666666667  0.000000000  1.0
end
```

The first flag is `screened_coulomb_cutoff` which is used to calculate the terms Σ_{XC} and Σ_{CH} (see appendix B). These cut-off's can not be greater than the epsilon cut-off. We use then the epsilon cut-off for the `screened_coulomb_cutoff`. The `bare_coulomb_cutoff` is the cut-off that is used for calculate the term Σ_X. Because the calculation of this term is not expensive, we use the same of the plane-wave cut-off used in the DFT calculation which is 80 Ry. The `number_bands` is the number of bands used in equation B.15. Because we choose `frequency_dependence 1`, we are using the GPP. The `band_index_min` and `band_index_max` is the range in which we want to compute the quasi-particle correction, that is, calculate $\langle n\mathbf{k}| \Sigma(\omega) |n\mathbf{k}\rangle$. The `screening_semiconductor` is chosen because our system is an insulator. And finally we have to add a block of **k**-points, which are the same of the `WFN_inner`. The execution of this program is done executing the command

```
sigma.cplx.x <sigma.inp> sigma.out.
```

The files `sigma.out`, `sigma.log`, `sigma_hp.log` and `ch_converge.dat` will be created. The `sigma.out` gives us computational information where we can see for example the time that the calculations take. The file `sigma_hp.log` is the high-precision of `sigma.log` and we can see the values of the quasi-particles energies for the desired sates that we choose in `sigma.inp`. Finally the `ch_converge.dat` gives us the convergence of the term Σ_{CH} with respect to the number of bands.

So far we have calculated the quasi-particle energies for the states with **k**-points of WFN_inner. To compute the electronic band-structure in a chosen path an interpolation is necessary. First we execute the command

```
eqp.py eqp1 sigma_hp.log eqp_co.dat
```

to generate the file `eqp_co.dat` which is a file with the quasi-particle corrected energies. Now we have to use the program `inteqp.cplx.x` to do the interpolation. This program needs the files `WFN_fi` (which has the information about the pw.x calculation on our chosen **k**-points path), `WFN_co`, `eqp_co.dat` and `inteqp.inp`. The `WFN_co` file is the wave-function on a coarse grid and we can use the `WFN_inner` file for that grid. We have then to create the following link with the command: `ln -s WFN_inner WFN_co`. The `inteqp.inp` is the input for the `inteqp.cplx.x` (see BerkeleyGW manual page 86). Our `inteqp.inp` has the following content:

```
number_val_bands_coarse 4
number_val_bands_fine 4
number_cond_bands_coarse 6
number_cond_bands_fine 6

use_symmetries_coarse_grid
no_symmetries_fine_grid
no_symmetries_shifted_grid
```

Because we used 1 as `band_index_min` and 10 as `band_index_max` in the `sigma.inp`, we have 4 valence bands and 6 conduction bands that are corrected. We have to choose the number of conduction and valence bands for the coarse grid, which can not be greater than the corrected ones. Then we have choose the number of valence and conduction bands from the DFT calculation along the chosen path (that is the reason why `inteqp.cplx.x` need the `WFN_fi` file do the interpolation). Those bands are the number of conduction and valence bands from the fine grid. The rest of the flags are symmetry considerations. After executing the command

`inteqp.cplx.x <inteqp.inp> inteqp.out`,

the file `bandstructure.dat` is going to be created and it is the interpolated band-structure along the **k**-point path used for creating the `WFN_fi`.

To synthesise the procedure of the G_0W_0 calculations we write the following list:

- Create a folder for the `epsilon.cplx.x` calculation. Link the files `WFN` and `WFNq` to this folder. Create the `epsilon.inp` and execute the command: `epsilon.cplx.x <epsilon.inp> epsilon.out`. The files `eps0mat` and `epsmat` are created.
- Create a folder for the `sigma.cplx.x` calculation. Link the files `WFN_inner`, `eps0mat` and `epsmat` to this folder. Create the `sigma.inp` and execute the command: `sigma.cplx.x <sigma.inp> sigma.out`. The file `sigma_hp.log` is created.
- In the same folder of `sigma.cplx.x` calculation, execute the command `eqp.py eqp1 sigma_hp.log eqp_co.dat`. the file `eqp_co.dat` is created.
- Create a folder for the `inteqp.cplx.x` calculation. Link the files `WFN_inner` to this folder but with the name `WFN_co`. Link the file `WFN_fi`, and `eqp_co.dat` to this folder. Create the `inteqp.inp` and execute the command `inteqp.cplx.x <inteqp.inp> inteqp.out`. The file `bandstructure.dat` is created.

C.2 BSE calculation

With the G_0W_0 calculation finished, we can now compute the BSE. The files that are needed from the G_0W_0 calculation are the `eps0mat` and `epsmat`, which are the files that contain the inverse dielectric matrix information, the file `eqp_co.dat` which is the file with the information of the corrected quasi-particles and the `WFN_co` which are the wave-functions on a coarse grid. First we have to compute the kernel matrix of equations B.21 and B.22. For that only the files `eps0mat` and `epsmat` and `WFN_co` are needed. The program to compute the kernel matrix is the `kernel.cplx.x` (cplx and not real because of the same reason discussed above) and its input is the `kernel.inp` (see BerkeleyGW manual page 77). In our example, the `kernel.inp` has the following content:

```
number_val_bands 4
number_cond_bands 6

screened_coulomb_cutoff 21.1
bare_coulomb_cutoff 80.0

use_symmetries_coarse_grid

screening_semiconductor
```

First we have to say how many valence (`number_val_bands`) and conduction bands (`number_cond_bands`) we want to include in the construction of the matrices M of equations B.21 and B.22. Then we have to choose the `screened_coulomb_cutoff` and `bare_coulomb_cutoff` just like we did in `sigma.inp`. In our case we choose them to be the same as `sigma.inp`. We select the `screening_semiconductor` as the type of screening used in this calculation. Now we can execute the command

`kernel.cplx.x <kernel.inp> kernel.out`,

and two files named `bsedmat` and `bsexmat` which corresponds to the the screened direct interaction term and the bare exchange interaction term of the kernel respectively are created.

As written in appendix B, after computing the kernel in the coarse grid using the information of `WFN_co`, we have to interpolate it in a very fine grid of **k**-points before solving equation B.18. For that we need to perform three DFT calculations. The first one is the calculation of the step 1 in the G_0W_0 calculation. The second one has the same procedure of the calculation of the step 4 in the G_0W_0 calculation. But this time we have to use in the `pw.x` calculation a list of **k**-points generated by the `kgrid.x` with a finer grid without shift and include few empty bands. Our input file for generating the

k-points, which we call `kgrid.wfn_fi.inp`, has the following content:

```
48 48 1
0.0 0.0 0.0
0.0 0.0 0.0
... # the rest is the same of kgrid.wfn.in
```

We can see that it is just like the `kgrid.wfn.in` but with a finer grid and no shift. After calculating the `pw.x` calculation with the grid generated by the file `kgrid.wfn_fi.inp` and with few empty bands, we have to convert the information of QE using the `pw2bgw.x` program just like we did in the previous calculations. The input file for the `pw2bgw.x` in our example has the following content:

```
&input_pw2bgw
   prefix = 'bn'
   real_or_complex = 2
   wfng_flag = .true.
   wfng_file = 'WFN_fi'
   wfng_kgrid = .true.
   wfng_nk1 = 48
   wfng_nk2 = 48
   wfng_nk3 = 1
   wfng_dk1 = 0.0
   wfng_dk2 = 0.0
   wfng_dk3 = 0.0
/
```

After converting the information using the `pw2bgw.x` program, the file `WFN_fi` is going to be created. It is important to note that this file is not the same that was created in the previous G_0W_0 calculation. The final `pw.x` calculation is just like the previous calculation but with a **q**-shift and only occupied bands. The input for the `kgrid.cplx.x`, which we call `krgid.wfnq_fi.inp`, has the following content:

```
48 48 1
0.0 0.0 0.0
0.048 0.048 0.0
... # the rest is the same of kgrid.wfn.in
```

After the `pw.x` calculation is done we have to use the `pw2bgw.x`, where the input file, which we call `BN.wfnq_fi.pp.in`, has the following content:

```
&input_pw2bgw
   prefix = 'bn'
   real_or_complex = 2
   wfng_flag = .true.
   wfng_file = 'WFNq_fi'
   wfng_kgrid = .true.
   wfng_nk1 = 48
   wfng_nk2 = 48
   wfng_nk3 = 1
   wfng_dk1 = 0.048
   wfng_dk2 = 0.048
   wfng_dk3 = 0.0
/
```

The file `WFNq_fi` is going to be created and together with the files `WFN_fi`, `bsedmat`, `bsexmat`, `epsmat`, `eps0mat` and `eqp_co.dat` we can now proceed to the final step of the BSE calculation. The program that is used is the `absorption.cplx.x` and the input file is `absorption.inp` (see page 81 of BerkeleyGW manual). This program is going to interpolate the kernel in a finer grid and then solve equation B.18. In our example the `absorption.inp` has the following content:

```
number_val_bands_fine 4
number_val_bands_coarse 4

number_cond_bands_fine  6
number_cond_bands_coarse 6

coarse_grid_points 144

use_symmetries_fine_grid
no_symmetries_shifted_grid
use_symmetries_coarse_grid

eqp_co_corrections

diagonalization

#haydock
#number_iterations 500


screening_semiconductor

use_velocity

q_shift 0.001 0.001 0.000

energy_resolution 0.1
gaussian_broadening
```

Just like the `inteqp.inp`, we have to choose the number of bands used in the coarse grid and in the fine grid. In the flag `coarse_grid_points` we have to write the number of **k**-points on the coarse grid. This number can be taken from the `kernel.out`. The flag `eqp_co_corrections` is to include the quasi-particle corrections. We can compute the equation B.18 using the flag `diagonalization` to do a diagonalization or use the flag `haydock` together with the `flag number_iterations` to do an iterative solution by Haydock recursion (see page 20 of literature [30] and BerkeleyGW manual page 83 to see more detail about this options). Then we have to write the operator to calculate optical transition probabilities where we can choose the velocity operator (`use_velocity`) or the momentum operator (`use_momentum`). Information about this operators can be found in page 30 of literature [30]. We have to choose a `q_shift` that has the same shift between the `WFN_fi` and `WFNq_fi`. The flags `energy_resolution` and `gaussian_broadening` are the

numerical broadening width and type respectively (see page 84 of BerkeleyGW manual to see the other options). Now we can finally execute the command

`absorption.cplx.x <absorption.inp> absorption.out`,

to obtain the absorption spectrum. The two files that correspond to the absorption spectrum are the `absorption_noeh.dat` and `absorption_eh.dat`. The first one gives the the non-interacting (RPA) dielectric and joint density of states. The second file gives the dielectric function with the excitonic effects included and the density of excitonic states. There are more files that are created that gives us information like the eigenvalues and excitonic wavefunctions (see page 81 BerkeleyGW manual for more information).

To summarize, after performing G_0W_0 calculations, we have to use two programs to compute the BSE calculation. The first program is `kernel.cplx.x` and it needs the `WFN_co`, `esp0mat` and `epsmat` of the previous G_0W_0 calculations. So we have to create a folder and link the three previously files to that folder. Then create the `kernel.inp` and execute the `kernel.cplx.x` program. After executing this program, the files `bsedmat` and `bsexmat` are created and we can now proceed to the next step which is to use the program `absorption.cplx.x`. This program also needs the files `WFN_fi`, `WFNq_fi` which are created by using `pw.x` and `pw2bgw.x` calculations and the file `eqp_co_corrections` which were created in the G_0W_0 calculation. So we have to create a new folder, link the 5 files for that folder and create the `absoprtion.inp` to execute the `absorption.cplx.x`. After executed, we can obtain the absorption spectra that is written in the file `absorption_eh.dat`.

Bibliography

[1] R. J. Powell and W. E. Spicer. Optical properties of nio and coo. *Phys. Rev. B*, 2:2182–2193, Sep 1970.

[2] S. Hüfner, J. Osterwalder, T. Riesterer, and F. Hulliger. Photoemission and inverse photoemission spectroscopy of nio. *Solid State Communications*, 52(9):793 – 796, 1984.

[3] G. A. Sawatzky and J. W. Allen. Magnitude and origin of the band gap in nio. *Phys. Rev. Lett.*, 53:2339–2342, Dec 1984.

[4] Yasushi Ishii, Shuhei Ohnishi, and Satoru Sugano. Effects of electron correlation and geometrical structure on stability of metal clusters. *Phys. Rev. B*, 33:5271–5279, Apr 1986.

[5] Susumu Saito and Marvin L. Cohen. Jellium-model calculation for dimer decays of potassium clusters. *Phys. Rev. B*, 38:1123–1130, Jul 1988.

[6] Silvana Botti, Francesco Sottile, Nathalie Vast, Valerio Olevano, Lucia Reining, Hans-Christian Weissker, Angel Rubio, Giovanni Onida, Rodolfo Del Sole, and R. W. Godby. Long-range contribution to the exchange-correlation kernel of time-dependent density functional theory. *Phys. Rev. B*, 69:155112, Apr 2004.

[7] W. Kohn and L. J. Sham. Self-consistent equations including exchange and correlation effects. *Phys. Rev.*, 140:A1133–A1138, Nov 1965.

[8] A. D. Becke. Density-functional exchange-energy approximation with correct asymptotic behavior. *Phys. Rev. A*, 38:3098–3100, Sep 1988.

[9] L. J. Sham and W. Kohn. One-particle properties of an inhomogeneous interacting electron gas. *Phys. Rev.*, 145:561–567, May 1966.

[10] John P. Perdew, Robert G. Parr, Mel Levy, and Jose L. Balduz. Density-functional theory for fractional particle number: Derivative discontinuities of the energy. *Phys. Rev. Lett.*, 49:1691–1694, Dec 1982.

[11] Lars Hedin. New method for calculating the one-particle green's function with application to the electron-gas problem. *Phys. Rev.*, 139:A796–A823, Aug 1965.

[12] Lars Hedin and Lundqvist S. Effects of electron-electron and electron-phonon interactions on the one-electron states of solids. *Solid State Physics*, 23, 1969.

[13] W. G. Aulbur and J. W. Wilkins. Quasiparticle calculations in solids in solid state physics. *Solid State Physics*, 54, 2000.

[14] E. E. Salpeter and H. A. Bethe. A relativistic equation for bound-state problems. *Phys. Rev.*, 84:1232–1242, Dec 1951.

[15] Stefan Albrecht, Lucia Reining, Rodolfo Del Sole, and Giovanni Onida. *Ab Initio* calculation of excitonic effects in the optical spectra of semiconductors. *Phys. Rev. Lett.*, 80:4510–4513, May 1998.

[16] Giovanni Onida, Lucia Reining, and Angel Rubio. Electronic excitations: density-functional versus many-body green's-function approaches. *Rev. Mod. Phys.*, 74:601–659, Jun 2002.

[17] Alexander L.Fetter and John Dirk Walecka. *Quantum Theory of Many-Particle Systems*. Dover, 2003.

[18] Alexander Zagoskin. *Quantum Theory of Many-Body Systems*. Springer.

[19] C. Friedrich and A. Schindlmayr. Many-body perturbation theory: The gw approximation. *Computational Nanoscience: Do It Yourself!*, 31:335–355, 2000.

[20] Julian Schwinger. On the green's functions of quantized fields. i. *Proceedings of the National Academy of Sciences*, 37(7):452–455, 1951.

[21] Paul C. Martin and Julian Schwinger. Theory of many-particle systems. i. *Phys. Rev.*, 115:1342–1373, Sep 1959.

[22] G. Strinati. Application of the Green's functions method to the study of the optical properties of semiconductors. *Nuovo Cimento Rivista Serie*, 11:1–86, December 1988.

[23] X. Blase, C. Attaccalite, and V. Olevano. First-principles *GW* calculations for fullerenes, porphyrins, phtalocyanine, and other molecules of interest for organic photovoltaic applications. *Phys. Rev. B*, 83:115103, Mar 2011.

[24] Sivan Refaely-Abramson, Roi Baer, and Leeor Kronik. Fundamental and excitation gaps in molecules of relevance for organic photovoltaics from an optimally tuned range-separated hybrid functional. *Phys. Rev. B*, 84:075144, Aug 2011.

[25] W. Hanke and L. J. Sham. Many-particle effects in the optical excitations of a semiconductor. *Phys. Rev. Lett.*, 43:387–390, Jul 1979.

[26] W. Hanke and L. J. Sham. Many-particle effects in the optical spectrum of a semiconductor. *Phys. Rev. B*, 21:4656–4673, May 1980.

[27] G. Strinati. Effects of dynamical screening on resonances at inner-shell thresholds in semiconductors. *Phys. Rev. B*, 29:5718–5726, May 1984.

[28] Mark S. Hybertsen and Steven G. Louie. Electron correlation in semiconductors and insulators: Band gaps and quasiparticle energies. *Phys. Rev. B*, 34:5390–5413, Oct 1986.

[29] F. Bechstedt, K. Tenelsen, B. Adolph, and R. Del Sole. Compensation of dynamical quasiparticle and vertex corrections in optical spectra. *Phys. Rev. Lett.*, 78:1528–1531, Feb 1997.

[30] Jack Deslippe, Georgy Samsonidze, David A. Strubbe, Manish Jain, Marvin L. Cohen, and Steven G. Louie. Berkeleygw: A massively parallel computer package for the calculation of the quasiparticle and optical properties of materials and nanostructures. *Computer Physics Communications*, 183(6):1269 – 1289, 2012.

[31] Natalia Berseneva, Andris Gulans, Arkady V. Krasheninnikov, and Risto M. Nieminen. Electronic structure of boron nitride sheets doped with carbon from first-principles calculations. *Phys. Rev. B*, 87:035404, Jan 2013.

[32] A. Nagashima, N. Tejima, Y. Gamou, T. Kawai, and C. Oshima. Electronic dispersion relations of monolayer hexagonal boron nitride formed on the ni(111) surface. *Phys. Rev. B*, 51:4606–4613, Feb 1995.

[33] A. Bhattacharya, S. Bhattacharya, and G. P. Das. Band gap engineering by functionalization of bn sheet. *Phys. Rev. B*, 85:035415, Jan 2012.

[34] Y. Kubota T. Taniguchi, K. Watanabe and O. Tsuda. Production of a hexagonal boron nitride crystal body capable of emitting out ultraviolet radiation, (may 2010), patent no. us 2010/0120187 a1.

[35] Chunyi Zhi, Yoshio Bando, Chengchun Tang, Hiroaki Kuwahara, and Dimitri Golberg. Large-scale fabrication of boron nitride nanosheets and their utilization in polymeric composites with improved thermal and mechanical properties. *Advanced Materials*, 21(28):2889–2893, 2009.

[36] Paolo Giannozzi, Stefano Baroni, Nicola Bonini, Matteo Calandra, Roberto Car, Carlo Cavazzoni, Davide Ceresoli, Guido L Chiarotti, Matteo Cococcioni, Ismaila Dabo, Andrea Dal Corso, Stefano de Gironcoli, Stefano Fabris, Guido Fratesi, Ralph Gebauer, Uwe Gerstmann, Christos Gougoussis, Anton Kokalj, Michele Lazzeri, Layla Martin-Samos, Nicola Marzari, Francesco Mauri, Riccardo Mazzarello, Stefano Paolini, Alfredo Pasquarello, Lorenzo Paulatto, Carlo Sbraccia, Sandro Scandolo, Gabriele Sclauzero, Ari P Seitsonen, Alexander Smogunov, Paolo Umari, and Renata M Wentzcovitch. Quantum espresso: a modular and open-source software project for quantum simulations of materials. *Journal of Physics: Condensed Matter*, 21(39):395502 (19pp), 2009.

[37] John P. Perdew, Kieron Burke, and Matthias Ernzerhof. Generalized gradient approximation made simple. *Phys. Rev. Lett.*, 77:3865–3868, Oct 1996.

[38] Hendrik J. Monkhorst and James D. Pack. Special points for brillouin-zone integrations. *Phys. Rev. B*, 13:5188–5192, Jun 1976.

[39] M. Topsakal, E. Aktürk, and S. Ciraci. First-principles study of two- and one-dimensional honeycomb structures of boron nitride. *Phys. Rev. B*, 79:115442, Mar 2009.

[40] H. Şahin, S. Cahangirov, M. Topsakal, E. Bekaroglu, E. Akturk, R. T. Senger, and S. Ciraci. Monolayer honeycomb structures of group-iv elements and iii-v binary compounds: First-principles calculations. *Phys. Rev. B*, 80:155453, Oct 2009.

[41] Jochen Heyd, Gustavo E. Scuseria, and Matthias Ernzerhof. Hybrid functionals based on a screened coulomb potential. *The Journal of Chemical Physics*, 118(18):8207–8215, 2003.

[42] V.L. Solozhenko, A.G. Lazarenko, J.-P. Petitet, and A.V. Kanaev. Bandgap energy of graphite-like hexagonal boron nitride. *Journal of Physics and Chemistry of Solids*, 62(7):1331 – 1334, 2001.

[43] Bi-Ching Shih, Yu Xue, Peihong Zhang, Marvin L. Cohen, and Steven G. Louie. Quasiparticle band gap of zno: High accuracy from the conventional G^0W^0 approach. *Phys. Rev. Lett.*, 105:146401, Sep 2010.

[44] Filip A. Rasmussen, Per S. Schmidt, Kirsten T. Winther, and Kristian S. Thygesen. Efficient many-body calculations for two-dimensional materials using exact limits for the screened potential: Band gaps of $\mathbf{mos}_2$, h-bn, and phosphorene. *Phys. Rev. B*, 94:155406, Oct 2016.

[45] John C. Inkson. The electron-electron interaction near an interface. *Surface Science*, 28(1):69 – 76, 1971.

[46] X. Blase, Angel Rubio, Steven G. Louie, and Marvin L. Cohen. Quasiparticle band structure of bulk hexagonal boron nitride and related systems. *Phys. Rev. B*, 51:6868–6875, Mar 1995.

[47] Ludger Wirtz, Andrea Marini, and Angel Rubio. Excitons in boron nitride nanotubes: Dimensionality effects. *Phys. Rev. Lett.*, 96:126104, Mar 2006.

[48] Jun Yan, Karsten W. Jacobsen, and Kristian S. Thygesen. Optical properties of bulk semiconductors and graphene/boron nitride: The bethe-salpeter equation with derivative discontinuity-corrected density functional energies. *Phys. Rev. B*, 86:045208, Jul 2012.

[49] A. Rubio L. Wirtz, A. Marini. Optical absorption of hexagonal boron nitride and bn nanotubes. 786:391–395, 2005.

[50] M. Kuisma, J. Ojanen, J. Enkovaara, and T. T. Rantala. Kohn-sham potential with discontinuity for band gap materials. *Phys. Rev. B*, 82:115106, Sep 2010.

[51] Li Song, Lijie Ci, Hao Lu, Pavel B. Sorokin, Chuanhong Jin, Jie Ni, Alexander G. Kvashnin, Dmitry G. Kvashnin, Jun Lou, Boris I. Yakobson, and Pulickel M. Ajayan.

[52] Valvin P. Cassabois G. and Gil B.

[53] Jarillo-Herrero Pablo Churchill, Hugh O. H. Two-dimensional crystals: Phosphorus joins the family. *Nat Nano*, 9:330–331.

[54] Liangbo Liang, Jun Wang, Wenzhi Lin, Bobby G. Sumpter, Vincent Meunier, and Minghu Pan. Electronic bandgap and edge reconstruction in phosphorene materials. *Nano Letters*, 14(11):6400–6406, 2014. PMID: 25343376.

[55] Robert W. Keyes. The electrical properties of black phosphorus. *Phys. Rev.*, 92:580–584, Nov 1953.

[56] Kong Xianghua Hu-Zhi-Xin Yang Feng Ji Wei. Qiao, Jingsi. High-mobility transport anisotropy and linear dichroism in few-layer black phosphorus. *Nat Commun*, 5, July 2014.

[57] Han Liu, Adam T. Neal, Zhen Zhu, Zhe Luo, Xianfan Xu, David Tománek, and Peide D. Ye. Phosphorene: An unexplored 2d semiconductor with a high hole mobility. *ACS Nano*, 8(4):4033–4041, 2014. PMID: 24655084.

[58] Yuanyue Liu, Fangbo Xu, Ziang Zhang, Evgeni S. Penev, and Boris I. Yakobson. Two-dimensional mono-elemental semiconductor with electronically inactive defects: The case of phosphorus. *Nano Letters*, 14(12):6782–6786, 2014. PMID: 25162380.

[59] Liangzhi Kou, Thomas Frauenheim, and Changfeng Chen. Phosphorene as a superior gas sensor: Selective adsorption and distinct i–v response. *The Journal of Physical Chemistry Letters*, 5(15):2675–2681, 2014. PMID: 26277962.

[60] Yexin Deng, Zhe Luo, Nathan J. Conrad, Han Liu, Yongji Gong, Sina Najmaei, Pulickel M. Ajayan, Jun Lou, Xianfan Xu, and Peide D. Ye. Black phosphorus–monolayer mos2 van der waals heterojunction p–n diode. *ACS Nano*, 8(8):8292–8299, 2014. PMID: 25019534.

[61] Deniz Çak ır, Hasan Sahin, and François M. Peeters. Tuning of the electronic and optical properties of single-layer black phosphorus by strain. *Phys. Rev. B*, 90:205421, Nov 2014.

[62] V. Wang, Y. Kawazoe, and W. T. Geng. Native point defects in few-layer phosphorene. *Phys. Rev. B*, 91:045433, Jan 2015.

[63] Vy Tran, Ryan Soklaski, Yufeng Liang, and Li Yang. Layer-controlled band gap and anisotropic excitons in few-layer black phosphorus. *Phys. Rev. B*, 89:235319, Jun 2014.

[64] Jones Aaron M. Seyler Kyle L. Tran Vy Jia Yichen Zhao Huan Wang Han Yang Li Xu Xiaodong Xia Wang, Xiaomu and Fengnian. Highly anisotropic and robust excitons in monolayer black phosphorus. *Nat Nano*, 10:517–521, Aug 2015.

[65] A. N. Rudenko, Shengjun Yuan, and M. I. Katsnelson. Toward a realistic description of multilayer black phosphorus: From *gw* approximation to large-scale tight-binding simulations. *Phys. Rev. B*, 92:085419, Aug 2015.

[66] A. N. Rudenko and M. I. Katsnelson. Quasiparticle band structure and tight-binding model for single- and bilayer black phosphorus. *Phys. Rev. B*, 89:201408, May 2014.